

**Mixed-conducting perovskites as cathodes in protonic
ceramic fuel cells:
Defect chemistry and transport properties**

Von der Fakultät Chemie der Universität Stuttgart
zur Erlangung der Würde eines

Doktors der Naturwissenschaften
(Dr. rer. nat.)

genehmigte Abhandlung

Vorgelegt von
Reihaneh Zohourian Aboutorabi
aus Maschhad, Iran

Hauptberichter:	Prof. Dr. rer. nat. J. Maier
Mitberichterin:	Prof. Dr. rer. nat. A. Weidenkaff
Prüfungsvorsitzender:	Prof. Dr. rer. nat. J. van Slageren

Tag der Einreichung:	04.05.2018
Tag der mündlichen Prüfung:	19.07.2018

Max-Planck-Institut für Festkörperforschung

Stuttgart

2018

Erklärung über die Eigenständigkeit der Dissertation

Ich versichere, dass ich die vorliegende Arbeit mit dem Titel *Mixed-conducting perovskites as cathodes in protonic ceramic fuel cells: defect chemistry and transport properties* selbständig verfasst und keine anderen als die angegebenen Quellen und Hilfsmittel benutzt habe; aus fremden Quellen entnommene Passagen und Gedanken sind als solche kenntlich gemacht.

Declaration of Authorship

I hereby certify that the dissertation entitled *Mixed-conducting perovskites as cathodes in protonic ceramic fuel cells: defect chemistry and transport properties* is entirely my own work except where otherwise indicated. Passages and ideas from other sources have been clearly indicated.

Name/Name: Reihaneh Zohourian Aboutorabi

Unterschrift/Signed: 

Datum/Date: 03.05.2018

Contents

ABBREVIATIONS AND SYMBOLS.....	III
LIST OF ABBREVIATIONS.....	III
LIST OF SYMBOLS.....	IV
ZUSAMMENFASSUNG	VII
ABSTRACT.....	XI
1 INTRODUCTION AND MOTIVATION.....	2
2 THEORETICAL BACKGROUND.....	10
3 EXPERIMENTAL.....	16
3.1 SAMPLE PREPARATION	16
3.1.1 Powder preparation	16
3.1.2 Pellet preparation.....	19
3.1.3 Particle preparation for TG.....	22
3.1.4 Pulsed laser deposited samples: Microelectrodes.....	22
3.2 CHARACTERIZATION TECHNIQUES.....	25
3.2.1 X-ray diffraction (XRD)	25
3.2.2 Inductively coupled plasma optical emission spectroscopy (ICP-OES)	25
3.2.3 Thermogravimetry coupled with mass spectroscopy (TG-MS)	25
3.2.4 Karl-Fischer titration.....	30
3.2.5 Impedance measurement.....	31
3.2.6 Microelectrode measurement.....	32
3.3 ALTERNATIVE ELECTROLYTES FOR SURFACE OXYGEN EXCHANGE KINETICS STUDY OF CATHODES.....	33
4 RESULTS AND DISCUSSION.....	40
4.1 TWO-FOLD STOICHIOMETRY RELAXATION IN ELECTROLYTE PEROVSKITES.....	40
4.1.1 Details of the simulations.....	40
4.1.2 Results and discussion	42
4.2 PROTON UPTAKE IN MIXED-CONDUCTING PEROVSKITES.....	51
4.2.1 Proton-conducting cathode materials	51
4.2.2 Detailed example: $Ba_{0.85}La_{0.15}FeO_{3-\delta}$ (BL15F).....	51
4.2.3 Proton uptake in different materials.....	54
4.2.4 Trends of proton uptake with cation composition	66
4.2.5 Defect interactions and non-ideal behavior	74
4.2.6 Electronic conductivity measurements.....	81
4.2.7 Ionic conductivity measurements	83
4.2.8 Design strategies	84
4.3 SURFACE OXYGEN REDUCTION MECHANISM OF THE PCFC CATHODE MATERIALS	85
5 CONCLUSION AND SUMMARY.....	91
REFERENCES	95
ACKNOWLEDGEMENT	103
CURRICULUM VITAE.....	105

Abbreviations and symbols

List of abbreviations

AC	alternating current
BCFZr	$\text{Ba}(\text{Co}_{0.4}\text{Fe}_{0.4}\text{Zr}_{0.2})\text{O}_{3-\delta}$
BCFZrY	$\text{Ba}(\text{Co}_{0.4}\text{Fe}_{0.4}\text{Zr}_{0.1}\text{Y}_{0.1})\text{O}_{3-\delta}$
BCY20	$\text{Ba}(\text{Co}_{0.8}\text{Y}_{0.2})\text{O}_{3-\delta}$
BET	Brunauer-Emmett-Teller
BFY20	$\text{Ba}(\text{Fe}_{0.8}\text{Y}_{0.2})\text{O}_{3-\delta}$
BL _x FZn _y	$(\text{Ba}_{1-x}\text{La}_x)(\text{Fe}_{1-y}\text{Zn}_y)\text{O}_{3-\delta}$
BL _x F	$(\text{Ba}_{1-x}\text{La}_x)\text{FeO}_{3-\delta}$
BSCF	$(\text{Ba}_{0.5}\text{Sr}_{0.5})(\text{Co}_{0.8}\text{Fe}_{0.2})\text{O}_{3-\delta}$
BSCN	$(\text{Ba}_{0.5}\text{Sr}_{0.5})(\text{Co}_{0.8}\text{Nb}_{0.2})\text{O}_{3-\delta}$
BSF	$(\text{Ba}_{0.5}\text{Sr}_{0.5})\text{FeO}_{3-\delta}$
BSFZn	$(\text{Ba}_{0.5}\text{Sr}_{0.5})(\text{Fe}_{0.8}\text{Zn}_{0.2})\text{O}_{3-\delta}$
BZC _y Y _x	$\text{Ba}(\text{Zr}_{1-x-y}\text{Ce}_y\text{Y}_x)\text{O}_{3-\delta}$
CE	counter electrode
CHP	combined heat and power
CPE	constant phase element
DC	direct current
DFT	density functional theory
EIS	electrochemical impedance spectroscopy
FC	flow controller
FOC	first order correction
GB	grain boundary
ICP-OES	inductively coupled plasma-optical emission spectrometry
KFT	Karl-Fischer titration
LSC	$(\text{La}_{0.5}\text{Sr}_{0.5})\text{CoO}_{3-\delta}$
LSF	$(\text{La}_{0.5}\text{Sr}_{0.5})\text{FeO}_{3-\delta}$

LWO	$\text{La}_{27}\text{W}_5\text{O}_{54+\delta}$
Mo-LWO	$\text{La}_{27}(\text{W}_{3.5}\text{Mo}_{1.5})\text{O}_{54+\delta}$
MS	mass-spectroscopy
O^{2-} -SOFC	oxide-ion conducting solid oxide fuel cell
PCFC	protonic ceramic fuel cell
PECS	pulsed electric current sintering
PLD	pulsed laser deposition
SEM	scanning electron microscopy
SF	$\text{SrFeO}_{3-\delta}$
SFZn	$\text{Sr}(\text{Fe}_{0.8}\text{Zn}_{0.2})\text{O}_{3-\delta}$
SL15F	$(\text{Sr}_{0.85}\text{La}_{0.15})\text{FeO}_{3-\delta}$
SL25F	$(\text{Sr}_{0.75}\text{La}_{0.25})\text{FeO}_{3-\delta}$
SOFC	solid oxide fuel cell
SPS	spark plasma sintering
SSRS	solid-state reactive sintering
TG	thermogravimetry
TPB	triple phase boundary
WE	working electrode
XRD	X-ray diffraction
YSZ	Y-stabilized zirconia

List of symbols

ASR	area specific resistance
A'	acceptor dopant according to the Kröger-Vink notation
a	oxygenation interaction parameter
a	lattice constant
b	hydration interaction parameter
$A'h'$	hole trapped on the acceptor dopant
C	capacitance

c_j	concentration of the defect j
d	microelectrode diameter
D	diffusivity
D^{eff}	effective diffusivity
D^δ	chemical diffusivity
e	elementary charge
e'	electron according to the Kröger-Vink notation
E_a	activation energy
F	Faraday constant
$\text{Fe}_{\text{Fe}}^\bullet$	electronic hole defects trapped on Fe site
h^\bullet	electron hole defect according to the Kröger-Vink notation
I_{18}	ion current of the water molecule in mass spectroscopy
I_{28}	ion current of the nitrogen molecule in mass spectroscopy
J_j	flux of the defect j
k	Boltzmann constant
k^q	chemical effective rate constant
K_{hydrat}	hydration mass action constant
K_{hydrog}	hydrogenation mass action constant
K_{OX}	oxygenation mass action constant
l	thickness
n	depression factor
$\text{OH}_\text{O}^\bullet$	protonic defect according to the Kröger-Vink notation
$p\text{H}_2\text{O}$	water partial pressure
$p\text{O}_2$	oxygen partial pressure
Q	constant phase element
r	ratio of electronic resistance over surface reduction resistance
r_{ion}	ionic radius

R	8.31477 JK ⁻¹ mol ⁻¹ , universal gas constant
R	resistance
R_{eon}	electronic resistance
R_i	ionic resistance
R_s	surface reduction reaction resistance
R_s'	apparent surface reduction reaction resistance
t	Goldschmidt tolerance factor
t	time
t	transference number
T	absolute temperature
$V_{\text{O}}^{\bullet\bullet}$	oxygen vacancy according to the Kröger-Vink notation
z_{ion}	ion charge
Z'	real part of the impedance
Z''	imaginary part of the impedance
δ	oxygen vacancy concentration
$\Delta C_{\text{p,R}}$	reaction heat capacity at constant pressure
ΔG°	standard Gibbs free energy
ΔH°	standard enthalpy
ΔS°	standard entropy
σ	conductivity
λ_{AllRoch}	Allred-Rochow electronegativity
λ_{ion}	ion electronegativity
$\chi_{\text{h}\cdot}$	trapping factor for holes

Zusammenfassung

Die Eigenschaften von Oxiden mit Perowskit-Struktur können durch die Wahl der Kationen auf A- und B-Platz des Perowskits und durch Dotierung über einen großen Bereich eingestellt werden. Somit können Perowskite sowohl als ionenleitende Elektrolytmaterialien wie auch als gemischtleitende Elektroden in Festoxidebrennstoffzellen eingesetzt werden. Keramische Brennstoffzellen mit protonenleitenden Elektrolytmaterialien (PCFC) wie $\text{Ba}(\text{Zr,Ce,Y})\text{O}_{3-\delta}$ haben letzter Zeit viel Aufmerksamkeit erhalten, da sie bei niedrigeren Temperaturen im Vergleich zu konventionellen Festoxidebrennstoffzellen (SOFC) einsetzbar sind. Sie erlauben auch eine höhere Brennstoffnutzung, da der Brennstoff durch die Wasserbildung, die an der Kathodeseite stattfindet, nicht verdünnt wird. In der vorliegenden Dissertation werden die Defektchemie und die Kinetik solcher Perowskite untersucht, die für PCFC relevant sind.

Dotieren von BaZrO_3 mit redoxinaktiven Akzeptoren führt zu Materialien, die unter trockenen Bedingungen über Sauerstoffleerstellen ($\text{V}_\text{O}^{\bullet\bullet}$) leiten, und unter feuchten Bedingungen Protonenleiter sind (Bildung der Protonen $\text{OH}_\text{O}^\bullet$ durch dissoziative Wasseraufnahme, $\text{H}_2\text{O} + \text{V}_\text{O}^{\bullet\bullet} + \text{O}_\text{O}^\times \rightleftharpoons 2\text{OH}_\text{O}^\bullet$). Bei hohem Sauerstoffpartialdruck weist akzeptordotiertes BaZrO_3 jedoch zusätzlich eine elektronische p-Typ-Leitfähigkeit auf. Unter diffusionkontrollierten Bedingungen zeigen solche Systeme mit drei beweglichen Ladungsträgern ($\text{V}_\text{O}^{\bullet\bullet}$, $\text{OH}_\text{O}^\bullet$, h^\bullet) eine besondere Kinetik der Stöchiometrierelaxation mit zwei Zeitkonstanten („two-fold relaxation“). Im ersten Teil der vorliegenden Dissertation wird diese spezielle Kinetik mittels numerischer Simulationen und mit besonderem Schwerpunkt auf die Temperaturabhängigkeit untersucht. Es wird gezeigt, dass man das Trapping der Elektronen-Löcher im Modell berücksichtigen muss, um die Aktivierungsenergie der beobachtenden phänomenologischen Diffusionskoeffizienten zu reproduzieren.

Eine PCFC Kathode muss viele Eigenschaften wie intrinsische Stabilität der Phase, extrinsische chemische Stabilität, hohe katalytische Aktivität sowie elektronische und protonische Leitfähigkeit besitzen, um gut zu funktionieren. Diese können durch Dotierung auf A- und B-Platz eingestellt werden, jedoch können dabei gegenläufige Tendenzen auftreten. Eine ausreichende Protonenleitfähigkeit in der Kathode ist erforderlich, um die Sauerstoffreduktionsreaktion über die Dreifachphasengrenze (wo sich die Kathode, Elektrolyte und Gasphase treffen) auszudehnen und die gesamte Kathodenoberfläche zu aktivieren (sogenannter „bulk-path“). Im zweiten Teil der vorliegenden Dissertation wird die Protonkonzentration von $(\text{Ba,Sr,Lu})(\text{Fe,Co,Zn,Zr,Y})\text{O}_{3-\delta}$ -Perowskiten mittels Thermogravimetrie gemessen. Dazu werden die Proben typischerweise von höheren Temperaturen in N_2 rasch abgekühlt (Einfrieren der Sauerstoffaustauschreaktion), um eine hohe $\text{V}_\text{O}^{\bullet\bullet}$ - und eine niedrige Löcher-Konzentration zu erreichen. Somit werden die Protonen durch die

Hydratisierungsreaktion $\text{H}_2\text{O} + \text{V}_\text{O}^{\bullet\bullet} + \text{O}_\text{O}^\times \rightleftharpoons 2\text{OH}_\text{O}^\bullet$ aufgenommen, die eine reine Säure-Base-Reaktion darstellt. Bei hoher Löcher- und niedriger Sauerstoffleerstellen Konzentration dominiert die Redoxreaktion $\text{H}_2 + 2\text{h}^\bullet + 2\text{O}_\text{O}^\times \rightleftharpoons 2\text{OH}_\text{O}^\bullet$ (Wasserstoffaufnahme).

Für abgeschrecktes $(\text{Ba}_{0.95}\text{La}_{0.05})(\text{Fe}_{0.8}\text{Zn}_{0.2})\text{O}_{3-\delta}$ bei 250 °C und 100 ppm O_2 werden Protonenkonzentrationen von bis zu 10 mol% (0.1 Protonen pro Perowskit-Formeleinheit) gefunden. Dieser Wert verringert sich auf 5.5 mol% und 2.5 mol% für Proben mit equilibrierter Sauerstoffstöchiometrie in 0.84% O_2 und 8.3% O_2 , was für solch oxidierende Bedingungen noch immer ziemlich hoch ist. Allgemein ist der Grad der Hydratisierung für Kathodenmaterialien viel kleiner im Vergleich zu den Elektrolyten mit Perowskitstruktur, die unterhalb von 300 °C voll hydratisiert sind. Die Kathodenmaterialien weisen positivere Werte von $\Delta G_{\text{hydrat}}^\circ$ auf, die durch negativere Hydratationsentropien und weniger negative Hydratationsenthalpien verursacht sind.

Interessanterweise tritt für $(\text{Ba}_{0.95}\text{La}_{0.05})(\text{Fe}_{0.8}\text{Zn}_{0.2})\text{O}_{3-\delta}$, das Material mit der höchsten Protonenaufnahme, eine zweistufige Gewichtsänderung auf, wenn die Probe zuerst in einem mittleren $p\text{O}_2$ (z.B. 0.1 bar O_2) equilibriert und dann $p\text{H}_2\text{O}$ erhöht wird. Das kann qualitativ als ein Effekt der Oberflächenkinetik interpretiert werden: durch schnelle Wasseraufnahme nimmt die Sauerstoffleerstellenkonzentration unter den neuen Gleichgewichtswert ab, was eine nachfolgenden langsame Sauerstoffabgabe verursacht.

Die Ergebnisse der Variation der A- und B-Platz-Besetzung weisen darauf hin, dass eine partielle Substitution von Ba auf dem A-Platz anstelle von Sr aufgrund der höheren Basizität der Oxidionen von Vorteil ist. La auf dem A-Platz stabilisiert die kubische Perowskitphase, die Protonaufnahme, nimmt jedoch wegen der erhöhten Löcherkonzentration ab (nachteilige Proton-Loch-Wechselwirkung). Co (welches die katalytische Aktivität verbessert) verringert die Protonaufnahme, indem die B–O Bindungen kovalenter werden (stärkere Überlappung der Orbitale, mehr Defektwechselwirkungen). Interessanterweise ist die partielle Substitution von Zn auf dem B-Platz vorteilhaft für die Protonaufnahme. Eine Auftragung von $\Delta G_{\text{hydrat}}^0$ (als Maß der Protonenaufnahme) gegen Kationelektro negativität (die die Basizität der Oxidionen beeinflusst) zeigt, dass alle Kathodenmaterialien einer Korrelationslinie folgen, die sich jedoch von derjenigen der Elektrolytmaterialien unterscheidet. Das zeigt, dass zusätzliche Faktoren wie der Grad der Kovalenz der B–O-Bindungen, die Oxidationsstufe des B-Kations *etc.*, für die Protonaufnahme wichtig sind. Die abnehmende Protonenaufnahme mit zunehmender Kovalenz der B–O-Bindungen, die mit Delokalisierung und Beweglichkeit der Löcher zusammenhängt, zeigt, dass für PCFC-Kathodenmaterialien ein Kompromiss zwischen elektronischer Leitfähigkeit und Protonenaufnahme gefunden werden muss. Kathodenmaterialien wie $\text{Ba}(\text{Co}_{0.4}\text{Fe}_{0.4}\text{Zr}_{0.1}\text{Y}_{0.1})\text{O}_{3-\delta}$ mit vergleichsweise niedriger elektronischer Leitfähigkeit ($\sim 1 \text{ Scm}^{-1}$) und moderater Protonenaufnahme (2.2 mol%) wiesen in der Literatur gute Leistungen auf; dies zeigt, dass gute Kompromisse möglich sind.

Die detaillierten chemischen Defektuntersuchungen in der vorliegenden Arbeit zeigen, dass in den untersuchten Perowskiten Defektwechselwirkungen wichtig sind. Die Sauerstoffstöchiometrie wurde durch Thermogravimetrie in verschiedenen pO_2 (trockene Atmosphäre) bestimmt. Die van 't Hoff-Kurve der Oxidationsreaktion ist nicht linear und variiert mit dem Sauerstoffpartialdruck, was eindeutig eine Abweichung vom idealen Verhalten belegt. Bei niedrigeren Temperaturen, bei denen die Löcherkonzentration ansteigt (abnehmende Sauerstoffleerstellen-Konzentration), wird die van 't Hoff-Kurve flacher. Das bedeutet, dass die Oxidationsreaktion weniger exotherm wird. Dieses Verhalten kann durch Loch-Loch-Wechselwirkungen erklärt werden, die bereits bei niedrigen Lochkonzentrationen auftreten, da die Löcher (die in Fe-reichen Perowskiten kleinen Polaronen entsprechen) teilweise vom Übergangsmetall zu den benachbarten Oxidionen delokalisiert sind. Da diese Delokalisierung der Löcher die Basizität der Oxidionen beeinflusst, nimmt auch die Protonenkonzentration ab. Das zeigt sich deutlich in den Protonenaufnahmemessungen für Proben mit equilibrierter Sauerstoffstöchiometrie, die trotz einer immer noch hohen $V_O^{\bullet\bullet}$ -Konzentration eine geringere Protonenaufnahme aufweisen als die abgeschreckten Proben.

Quantitativ kann das nicht-ideale Verhalten durch eine Korrektur erster Ordnung für Loch-Loch- und Loch-Proton-Wechselwirkungen beschrieben werden. Die Enthalpie der Oxidations- und Hydratationsreaktion ändert sich linear mit der Konzentration der Löcher. Innerhalb der $(Ba,La)FeO_{3-\delta}$ -Materialfamilie ändern sich die Parameter für die Loch-Loch- und Loch-Proton-Wechselwirkungen parallel, sogar ihre absoluten Werte sind recht ähnlich. Das kann darauf zurückgeführt werden, dass Löcher mit anderen Löchern und Protonen durch die Beeinflussung der Oxidionen interagieren. Für $(Ba_{0.95},La_{0.05})(Fe_{0.8},Zn_{0.2})O_{3-\delta}$ ist der Wechselwirkungs-Parameter am kleinsten, was den günstigen Effekt von Zn auf die Unterdrückung von Defektwechselwirkungen unterstreicht.

Die Kinetik der Sauerstoffreduktionsreaktion an der Oberfläche ist ein weiterer wichtiger Aspekt eines Kathodenmaterials, der am besten durch Messungen an geometrisch gut definierten dichten Dünnschicht-Mikroelektroden untersucht werden kann. In Zellen mit hohem pO_2 an beiden Elektroden erschwert jedoch die nicht vernachlässigbare elektronische Überführungszahl des Elektrolyten die Messungen erheblich. In dieser Arbeit wurde die elektronische Überführungszahl von keramischen Proben der protonenleitenden Elektrolyten $La_{27}W_5O_{54+\delta}$ (Fluorit-verwandte Struktur) und $Ba(Zr,Ce,Y)O_{3-\delta}$ (Perowskit) bestimmt. Daraufhin wurden $La_{27}W_5O_{54+\delta}$ und $Ba(Zr_{0.89}Ce_{0.1}Y_{0.01})O_{3-\delta}$ als Elektrolytsubstrate für die Untersuchung der Oberflächenkinetik von $(Ba_{0.5}Sr_{0.5})(Co_{0.8}Fe_{0.2})O_{3-\delta}$ und $Ba(Co_{0.4}Fe_{0.4}Zr_{0.1}Y_{0.1})O_{3-\delta}$ -Kathodenmaterialien ausgewählt. Die Ergebnisse zeigen, dass die Sauerstoff- und insbesondere die Wasserpartialdruckabhängigkeit des Niederfrequenzhalbkreises empfindlich auf eine nichtvernachlässigbare elektronische Überführung reagieren.

Der Exponent der $p\text{O}_2$ -Abhängigkeit des Oberflächen-Reaktionswiderstands liegt geringfügig unter $1/2$. Ein Vergleich mit realistischen Reaktionsmechanismen weist jedoch trotzdem darauf hin, dass molekulare Sauerstoffspezies im ratenbestimmenden Schritt auftreten (wenn nur atomare Sauerstoffspezies beteiligt wären, ergäbe sich aufgrund der negativen $p\text{O}_2$ -Abhängigkeiten anderer beteiligter Defekte eine Gesamt- $p\text{O}_2$ -Abhängigkeit von ≤ 0.25). Dies ist analog zu Messungen an $(\text{Ba}_{0.5}\text{Sr}_{0.5})(\text{Co}_{0.8}\text{Fe}_{0.2})\text{O}_{3-\delta}$ -Mikroelektroden auf YSZ in der Literatur. Aus der $p\text{H}_2\text{O}$ -Abhängigkeit kann geschlossen werden, dass keine Protonen vor oder im ratenbestimmenden Schritt der Sauerstoffreduktion zu Wasser beteiligt sind. Die Abhängigkeit des Oberflächen-Reaktionswiderstands vom Mikroelektroden-durchmesser zeigt, dass sich die reaktive Zone deutlich über die Dreiphasengrenze hinaus erstreckt, auch wenn die für reinen "bulk path" (Protonentransfer durch das Kathodenmaterial, so dass die komplette Kathodenoberfläche aktiv wird) idealerweise erwartete Steigung nicht voll erreicht wird.

Abstract

The properties of oxides with perovskite structure can be tuned over a large range by the choice of the cations on the perovskite's A- and B-site and additional doping. Thus, for ceramic fuel cells perovskites can be used as selectively ion-conducting electrolyte materials as well as [in the function of] mixed-conducting electrodes. Protonic ceramic fuel cells (PCFC) based on proton-conducting $\text{Ba}(\text{Zr,Ce,Y})\text{O}_{3-\delta}$ electrolyte materials recently gained interest because they allow one to operate the device at lower temperatures compared to conventional solid oxide fuel cells (SOFC) and run at higher fuel utilization since the fuel is not diluted by water (which instead forms at the cathode). In the present thesis, the defect chemistry and kinetics of perovskite materials are investigated that are relevant for PCFCs.

Using BaZrO_3 as the base material and doping it with redox-inactive acceptors leads to materials which are oxygen vacancy ($V_{\text{O}}^{\bullet\bullet}$) conductors under dry and proton conductors under humid conditions (formation of protonic defects $\text{OH}_{\text{O}}^{\bullet}$ by dissociative water incorporation $\text{H}_2\text{O} + V_{\text{O}}^{\bullet\bullet} + \text{O}_{\text{O}}^{\times} \rightleftharpoons 2\text{OH}_{\text{O}}^{\bullet}$). However, in high oxygen partial pressure ($p\text{O}_2$) acceptor-doped BaZrO_3 develops also some p-type electronic conductivity. Such systems with three mobile carriers ($V_{\text{O}}^{\bullet\bullet}$, $\text{OH}_{\text{O}}^{\bullet}$, h^{\bullet}) are known to exhibit peculiar two-fold kinetics of diffusion-controlled stoichiometry relaxation. In the first part of the present thesis, this two-fold kinetics is investigated using finite-difference simulation with special emphasis on the temperature dependence. It is shown that in order to reproduce the activation energies of the observed phenomenological diffusion coefficients for $\text{Ba}(\text{Zr,Ce,Y})\text{O}_{3-\delta}$ perovskites, trapping of the holes must be included in the model.

A promising PCFC cathode material should meet several criteria including intrinsic phase stability, extrinsic chemical stability (e.g. against carbonate formation), high values for the catalytic activity, electronic conductivity and proton conductivity in order to function well. These properties can be tuned by A- and B-site doping of the perovskite, however there may be conflicting relations. A sufficient proton conductivity in the cathode is required to extend the oxygen reduction reaction beyond the triple phase boundary (where cathode, electrolyte and the gas phase meet) and activate the whole surface of the cathode (so-called "bulk path"). In the second part of the present thesis, the proton concentration of $(\text{Ba,Sr,La})(\text{Fe,Co,Zn,Zr,Y})\text{O}_{3-\delta}$ perovskites is measured using thermogravimetry. In most cases this is done for samples that are quenched from high temperature in N_2 (freezing the oxygen exchange reaction) in order to have a high $V_{\text{O}}^{\bullet\bullet}$ and low hole concentration. Then, protons are incorporated by the acid-base hydration reaction $\text{H}_2\text{O} + V_{\text{O}}^{\bullet\bullet} + \text{O}_{\text{O}}^{\times} \rightleftharpoons 2\text{OH}_{\text{O}}^{\bullet}$. In the case of high hole and low $V_{\text{O}}^{\bullet\bullet}$ concentration, the redox hydrogenation reaction $\text{H}_2 + 2h^{\bullet} + 2\text{O}_{\text{O}}^{\times} \rightleftharpoons 2\text{OH}_{\text{O}}^{\bullet}$ dominates.

Proton concentrations as high as 10 mol% (0.1 proton per perovskite formula unit) are found for quenched $(\text{Ba}_{0.95}\text{La}_{0.05})(\text{Fe}_{0.8}\text{Zn}_{0.2})\text{O}_{3-\delta}$ at 250 °C and 100 ppm O_2 , which decreases to 5.5 mol% and 2.5 mol% for samples with oxygen content equilibrated in 0.84% O_2 and 8.3% O_2 (still quite high for such oxidizing conditions). In general, the degree of hydration is much smaller for the cathode materials compared to the electrolyte perovskites which are fully hydrated below 300 °C. The cathode materials have more positive $\Delta G_{\text{hydrat}}^0$, with a more negative standard hydration entropy and less negative standard hydration enthalpy compared to the electrolytes.

Interestingly, for the material with the highest proton uptake $(\text{Ba}_{0.95}\text{La}_{0.05})(\text{Fe}_{0.8}\text{Zn}_{0.2})\text{O}_{3-\delta}$ a two-fold relaxation kinetics is observed in thermogravimetry when the sample is first equilibrated with an intermediate $p\text{O}_2$ (e.g. 0.1 bar O_2) and then $p\text{H}_2\text{O}$ increased. This can qualitatively be interpreted as an effect controlled by the surface exchange kinetics: fast water incorporation decreases the $V_{\text{O}}^{\bullet\bullet}$ concentration below the new equilibrium value, and as a consequence the slower oxygen release leads to a subsequent weight loss.

The results from variation of A- and B-site cations suggest that a partial substitution of Ba on the A-site is beneficial compared to Sr due to increased oxide ion basicity. La on the A-site stabilizes the cubic perovskite phase, but decreases the proton uptake due to increased hole concentration (detrimental proton-hole interaction). Co (which enhances the catalytic activity) suppresses the proton uptake due to increased covalency of the B–O bonds (stronger overlapping of the orbitals and increased defect interactions). Interestingly, partial Zn substitution on the B-site is found to be very beneficial for proton uptake. A plot of $\Delta G_{\text{hydrat}}^{\circ}$ (as a measure of proton uptake) versus cation electronegativity (which is expected to affect the oxide ion basicity) reveals that all cathode materials are located along a correlation line which differs from that of the electrolyte materials. This suggests that further parameters such as the B–O bond covalency, B-site cation oxidation state, *etc.* matter for the proton incorporation. The decreasing proton uptake with increasing B–O bond covalency which is closely related to the delocalization and mobility of the holes implies that for PCFC cathode materials a compromise has to be found between electronic conductivity and proton uptake. Cathode materials such as $\text{Ba}(\text{Co}_{0.4}\text{Fe}_{0.4}\text{Zr}_{0.1}\text{Y}_{0.1})\text{O}_{3-\delta}$ with rather low electronic conductivity ($\sim 1 \text{ Scm}^{-1}$) and moderate proton uptake (2.2 mol%) have shown good performance in literature, indicating that good compromises are possible.

The detailed defect chemical investigations in this thesis demonstrate that in the studied perovskites, defect interactions are important. The oxygen stoichiometry was measured by thermogravimetry in dry condition (different $p\text{O}_2$). The oxygenation van 't Hoff plot is not linear and changes with oxygen partial pressure, which clearly indicates deviation from ideal behavior. At lower temperature where hole concentration increases (oxygen vacancy concentration decreases), the slope of the van 't Hoff plot decreases, suggesting that the

oxygenation becomes less favored. This behavior can be explained by hole-hole interactions which becomes perceptible already at low hole concentrations because the holes (which in Fe-rich perovskites correspond to small polarons) are partially delocalized from the transition metal to the adjacent oxide ions. Since this hole delocalization affects the oxide ion basicity, the proton concentration also decreases. This is clearly seen in proton uptake measurements for oxygen-equilibrated samples which have less proton uptake than the quenched samples (despite a still high $V_O^{\bullet\bullet}$ concentration).

Quantitatively, the non-ideal behavior can be described by a first-order correction for hole-hole as well as hole-proton interaction. The oxygenation and hydration enthalpy changes linearly with the concentration of holes. Within the (Ba,La)FeO_{3-δ} materials family, the interaction parameters for hole-hole and hole-proton interaction change in parallel, even their absolute values are rather similar. This is consistent with the fact that holes interact with other holes and protons, both through influencing the oxide ions. For (Ba_{0.95}La_{0.05})(Fe_{0.8}Zn_{0.2})O_{3-δ}, the interaction parameter is found to be the smallest which emphasizes the beneficial effect of Zn on suppression of defect interactions.

The surface oxygen reduction reaction is another important aspect of a cathode material which is best studied through measurements on dense thin-film microelectrode which are geometrically well-defined. However, in gas-symmetrical cells at high pO_2 , a non-negligible electronic transference number of the electrolyte significantly complicates the measurements. In this work, bulk measurements are performed on fluorite-related La₂₇W₅O_{54+δ} and perovskite Ba(Zr,Ce,Y)O_{3-δ} proton-conducting electrolytes to quantify their electronic transference number. Among these, La₂₇W₅O_{54+δ} and Ba(Zr_{0.89}Ce_{0.1}Y_{0.01})O_{3-δ} are chosen as electrolyte substrates for surface kinetics study of (Ba_{0.5}Sr_{0.5})(Co_{0.8}Fe_{0.2})O_{3-δ} and Ba(Co_{0.4}Fe_{0.4}Zr_{0.1}Y_{0.1})O_{3-δ} cathode materials. The results demonstrate that the oxygen and in particular water partial pressure dependence of the low-frequency semicircle are sensitive to electronic leakage effects. The exponent of the pO_2 dependence of the surface reaction resistance is slightly below 1/2, nevertheless a comparison with realistic mechanisms indicates that molecular oxygen species appear in the rate determining step, similar to the observations for (Ba_{0.5}Sr_{0.5})(Co_{0.8}Fe_{0.2})O_{3-δ} microelectrodes on YSZ in literature (if only atomic oxygen species would appear in the rate determining step, the negative pO_2 dependences of other defects involved would decrease the overall pO_2 dependence to ≤ 0.25). According to the pH_2O dependence, protons are not involved before or in the rate determining step of the oxygen reduction to water. The dependence of the surface reaction resistance on the microelectrode diameter demonstrates that the reactive zone is significantly extended beyond the three-phase boundary, although the slope ideally expected for the “bulk path” (proton transport through the cathode film and whole cathode surface active) is not fully achieved.

Chapter 1

Introduction and Motivation

1 Introduction and motivation

Fuel cells are highly-efficient electricity generators with theoretical efficiencies exceeding Carnot's efficiency. Ceramic fuel cells are of great interest for stationary applications as they have relatively longer life times compared to polymer electrolyte fuel cells; furthermore, they do not require Pt catalysts and they generate heat at higher temperatures which makes them very suitable for using this heat in other processes, e. g., combined heat and power (CHP) systems for buildings.

One can in general categorize ceramic fuel cells into oxide-ion conducting ceramic fuel cells (O^{2-} -SOFCs) and proton-conducting ceramic fuel cells (PCFCs) as illustrated in Figure 1-1. In O^{2-} -SOFC, the oxygen is reduced at the cathode and travels through the oxide-ion conducting electrolyte (such as acceptor-doped zirconia or ceria) to the anode, where it reacts with the fuel and forms water (resulting in fuel dilution) and delivers electronic charge carriers to the outer circuit. In the PCFC however, the hydrogen fuel forms protonic defects at the anode which travel through the proton-conducting ceramic electrolyte such as Y-doped $BaZrO_{3-\delta}$ or $BaCeO_{3-\delta}$ perovskites to the cathode, where oxygen reduction reaction and steam formation occurs without dilution of the fuel.

Figure 1-2 shows the power efficiency of ceramic fuel cells as a function of temperature [1]. Since the activation energy for the oxide-ion conductivity is higher compared to that of proton conductivity [2] (oxide-ions are doubly charged), PCFCs can operate at relatively lower temperatures (400-600 °C) which simplifies the sealing material choice for interconnect and slows down degradation processes. Furthermore, steam formation at the cathode side prevents fuel dilution which facilitates higher fuel utilization compared to O^{2-} -SOFCs and increases the efficiency [3]. For some time, difficulties in sintering proton-conducting perovskites and the blocking behavior of grain boundaries impeded the development of PCFC. More efficient sintering methods such as solid-state reactive sintering (SSRS) for the electrolytes and promising material choices for mixed hole and proton-conducting cathodes recently make PCFCs a serious competitor for O^{2-} -SOFCs.

In 2013, a peak power density of 230 Wcm^{-2} at 500 °C was reported for a cell with $BaCe_{0.7}Zr_{0.1}Y_{0.1}Yb_{0.1}O_{3-\delta}$ (BZCYYb) electrolyte and LSCF-BZCY composite as cathode [4]. Later that year, Shang *et. al.*, used $BaCo_{0.4}Fe_{0.4}Zr_{0.2}O_{3-\delta}$ on a BZCYYb electrolyte and obtained 225 mWcm^{-2} PCFC at 600 °C which was ~ 20 times more than for a comparable cell with LSCF cathode, the same fabrication procedure, and testing condition [5]. In 2015, Duan *et. al.*, used the same electrolyte, this time with cathode material $BaCo_{0.4}Fe_{0.4}Zr_{0.1}Y_{0.1}O_{3-\delta}$ which showed a power density as high as $\sim 650 \text{ mWcm}^{-2}$ at 600 °C and 445 mWcm^{-2} at 500 °C on H_2 and 142 mWcm^{-2} on CH_4 [1]. Maximum power of 115-742 mWcm^{-2} at 450-650 °C was realized for a thin film PCFC on an anode support with non-protonic ceramic matrix (composite of Ni and yttria-stabilized zirconia), BZCY

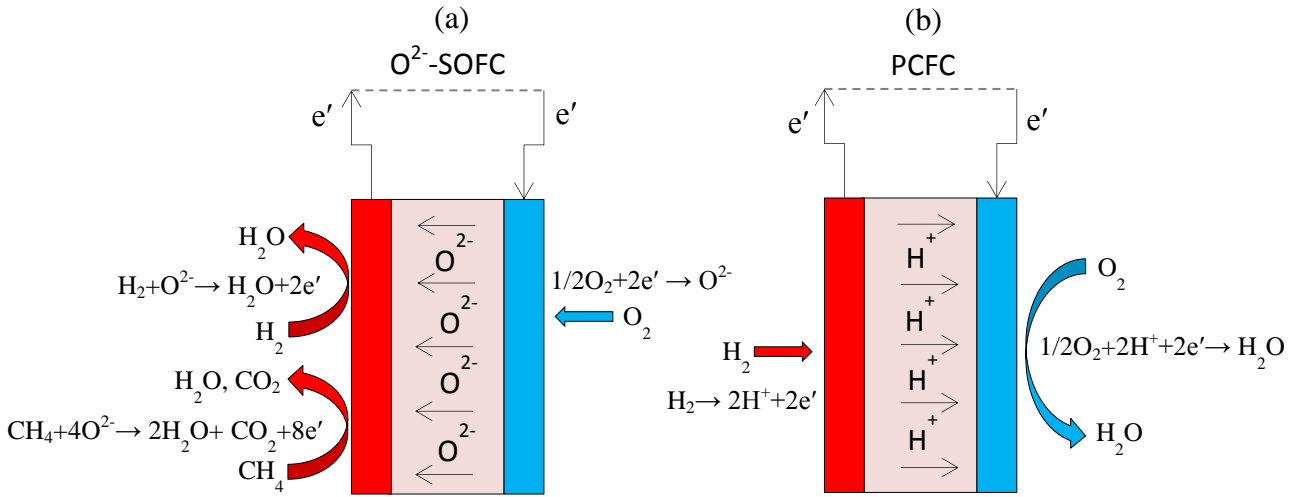


Figure 1-1: Schematic of an (a) oxide-ion conducting ceramic fuel cell with an oxide-ion conducting electrolyte where steam formation occurs at fuel side (anode) and (b) a proton-conducting ceramic fuel cell where water forms at the cathode.

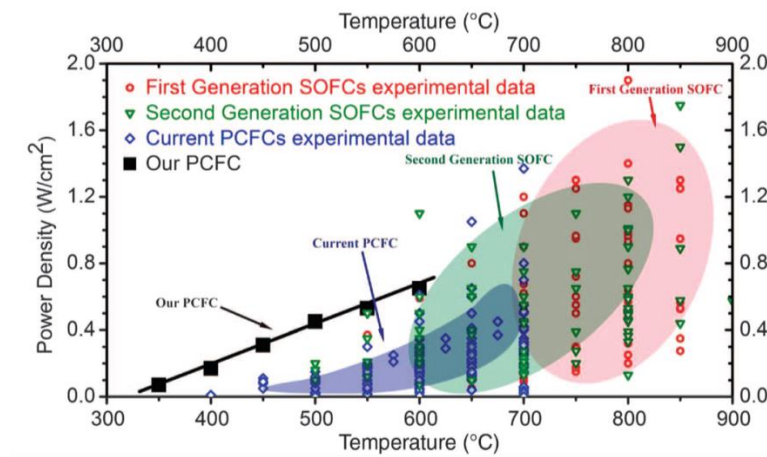


Figure 1-2: Power density as a function of temperature for different types of ceramic fuel cells including first generation O^{2-} -SOFC (Y-stabilized zirconia based solid oxide fuel cells), second generation O^{2-} -SOFC (based on other oxide-ion conducting electrolytes with lower operating temperatures) and PCFCs. The black squares refer to a PCFC with $BaCe_{0.7}Zr_{0.1}Y_{0.1}Yb_{0.1}O_{3-\delta}$ electrolyte and $BaCo_{0.4}Fe_{0.4}Zr_{0.1}Y_{0.1}O_{3-\delta}$ cathode which shows a power density of ~ 100 - 650 $mWcm^{-2}$ in the temperature range of 350 - 600 $^{\circ}C$ [1].

electrolyte, and $Ba_{0.5}Sr_{0.5}Co_{0.8}Fe_{0.2}O_3$ cathode in 2016 [6]; however, pulsed laser deposition was applied for fabrication of this cell which is not feasible in industry. Later in 2017, the same group reported a maximum power efficiency of 740 $mWcm^{-2}$ at 600 $^{\circ}C$ for a PCFC with $La_{0.6}Sr_{0.4}CoO_{3-\delta}$ cathode on PLD-deposited $BaZr_{0.85}Y_{0.15}O_{3-\delta}$ electrolyte [7]. A notable point of this cell is that the electrolyte resistance is smaller than that of the cathode reaction, i.e., the latter determines the performance. Recently, peak power density as high as 500 $mWcm^{-2}$ at 500 $^{\circ}C$ was reported using cathode material $PrBa_{0.5}Sr_{0.5}Co_{2-x}Fe_xO_{5+\delta}$ with a double perovskite structure on $BaCe_{0.4}Zr_{0.4}Y_{0.1}Yb_{0.1}O_{3-\delta}$ electrolyte. The most attractive feature of this cathode material is the pore channels in the $[PrO]$ and $[CoO]$ planes that could provide fast paths for oxygen transport, which in turn accelerates the kinetics of surface oxygen reduction reaction [8].

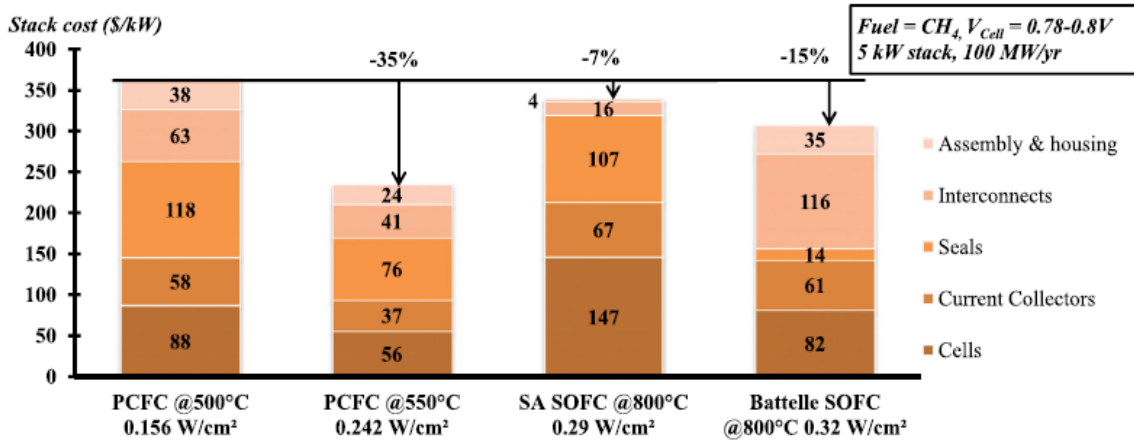


Figure 1-3: The total stack cost of PCFC at 500 °C and 550 °C compared to SOFCs at 800 °C and its different components including cells, current collectors, seals, interconnects, assembly and housing [9].

These promising performances result from optimized electrolytes as well as mixed hole and proton conductivity of these cathode perovskites. Analysis of small-scale PCFC and O²⁻-SOFC stacks has revealed that in comparable conditions, the prices can be competitive. Figure 1-3 shows the total cost and individual contribution of 5 kW stacks (yield of 20,000 stacks per year) with CH₄ as fuel and for a typical PCFC at 500 and 550 °C and two SOFCs at 800 °C. The cost for a PCFC stack operating at 550 °C can be 20% lower than O²⁻-SOFCs. In general, this shows that the lower material cost at lower operating temperature can compensate the lower power density of PCFCs (which requires larger number of cells at the same output power) compared to O²⁻-SOFCs. Any improvement in PCFC performance and fabrication methods can give significant economic advantages to the PCFC technology compared to the other counterparts [9].

For PCFCs, sintering of BZCY electrolytes represented a severe challenge for long time (high T , Ba loss, small grain sizes, and blocking grain boundaries [10]–[15]). In 2005, Babilo and Haile studied the influence of the transition metal oxide additives on the densification and electrical properties of Y-doped BaZrO_{3- δ} . In particular, they reported promising densifications when using NiO, CuO, and ZnO and succeeded to prepare > 93% dense BaZr_{0.85}Y_{0.15}O_{3- δ} by adding 4 mol% ZnO as a sintering aid at relatively low temperature of 1300 °C [16] and reported Zn accumulation at the grain boundaries. Tao and Irvine sintered 96% dense BaZr_{0.85}Y_{0.15}O_{3- δ} using 1 wt% ZnO at a T of 1325 °C [17]. In both studies, the better sintering was however achieved at the expense of degradation of the bulk and grain boundary conductivity.

Coors *et al.*, observed improved sinterability of BZY with 1 wt% of NiO which resulted in many other investigations for sintering electrolyte ceramics at relatively lower temperatures [18], [19]. The specific idea was that perovskite formation and transient liquid phase sintering (low-melting BaY₂NiO₅ phase) occur in a single step. This method is the so-called solid-state reactive sintering (SSRS). The resulting sintered material has larger grains compared to the

conventionally sintered one and the grain boundary conductivity is not decreased. However the proton concentration and bulk conductivity might slightly decrease and the optimization of NiO content is therefore necessary. SSRS offers a chance for simple processing and fabrication as it facilitates the sintering at comparably low temperature, allowing for simple fabrication methods such as tape-casting for large scale production of fuel cells.

The choice of cathode is also a decisive factor for PCFCs. Several characteristics should be considered for a promising cathode material including electronic conductivity, protonic conductivity, catalytic activity, phase stability and stability in CO_2 and H_2O containing atmosphere.

The oxygen reduction reaction at the cathode is a complex process which consists of several steps that depend on the type of the electrolyte and cathode material. For a proton-conducting electrolyte as in PCFCs, the overall reaction at the cathode ($\text{O}_2 + 4\text{H}^+ + 4e' \rightleftharpoons 2\text{H}_2\text{O}$) will comprise the following steps. The oxygen molecule in the gas phase diffuses to the cathode and is adsorbed taking one or two electrons (reduction to O_2^{-1} and O_2^{2-}) and finally dissociates forming O^{2-} . For proton-conducting cathode materials, the protons travel from the electrolyte through the cathode to the whole surface of the cathode where they can react with the reduced oxygen, form water and desorb it. In this case the whole surface of the cathode material is active for the oxygen reduction reaction. This mechanism is called “bulk path” (see Figure 1-4 right). Otherwise, for cathodes which are only conducting for oxygen vacancies or holes, the reduced oxygen must diffuse over the cathode surface to the triple phase boundary (TPB) where electrode, electrolyte and the gas phase meet and protons are available. The water would then form and desorb only at TPB (see Figure 1-4 left) and the much decreased active area decreases the cathode performance.

When cathodes with insufficient protonic conductivity are employed for a PCFC, the oxygen reduction reaction will be limited to the TPB (similar to a O^{2-} -SOFC cathode with

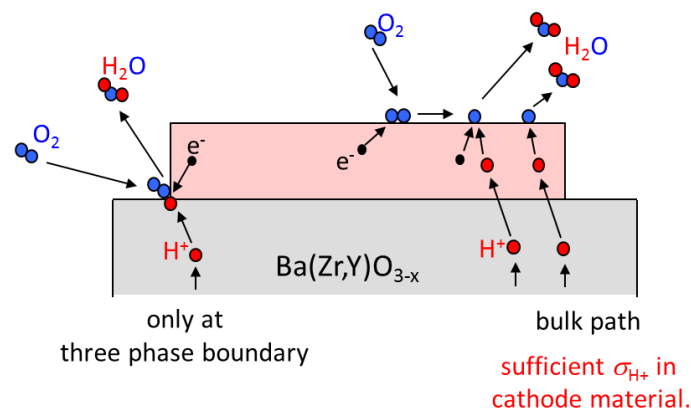


Figure 1-4: Bulk path (right) versus triple phase boundary path (left) in a proton-conducting ceramic fuel cell cathode. A certain protonic conductivity in a cathode material can activate the bulk path and increase the device power density by enabling the oxygen reduction reaction to happen on the whole surface of the cathode.

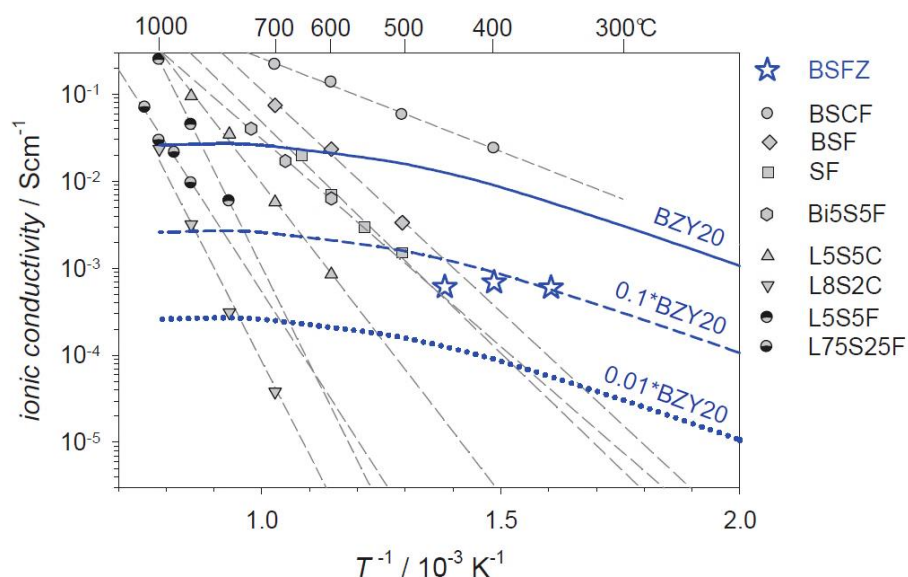


Figure 1-5: Oxygen vacancy conductivity for several cathode materials (in grey) for which the bulk path is known to be active and protonic conductivity for BSFZn and a typical electrolyte BZY20 (in blue) [20].

limited O^{2-} conductivity [21]). However, if the cathode shows some proton concentration and mobility, the protons will be enabled to travel from the electrolyte through the cathode to the whole surface of the cathode. In this case, the whole surface of the electrode will become active for the oxygen reduction reaction which is beneficial for the overall performance of the device. This is one major reason why cathode materials such as $Ba_{0.5}Sr_{0.5}Co_{0.8}Fe_{0.2}O_{3-\delta}$ and $BaCo_{0.4}Fe_{0.4}Zr_{0.1}Y_{0.1}O_{3-\delta}$ show promising performances, in addition to their relatively high catalytic activity. Simple calculations performed in the ref. [20] reveal that for a 100 nm thick microelectrode, the bulk path is active when the proton conductivity exceeds 10^{-5} Scm^{-1} ; i.e., rather moderate proton conductivity values suffice to extend the reactive zone.

In general, protonic conductivity measurements for cathode materials are very challenging. The direct measurement of the protonic conductivity needs the suppression of the predominant electronic conductivity which is difficult, as the electronic carriers are very mobile compared to ionic species. Already the measurement of proton concentration is challenging as the proton uptake mechanism depends on temperature and O_2 and H_2O partial pressures. The proton mobility measurements are also not straightforward; thermogravimetry and conductivity relaxation measurements on thick dense pellets should be performed to determine the diffusivity which are quite time-consuming measurement. Therefore, only few data on proton concentration and mobility of cathode materials is available in the literature.

An example of a cathode material with an active bulk path is $Ba_{0.5}Sr_{0.5}Fe_{0.8}Zn_{0.2}O_{3-\delta}$ (BSFZn) with a proton concentration of 0.32-1.3 mol% and proton diffusivity $\geq 3-0.7 \times 10^{-6} \text{ cm}^2\text{s}^{-1}$ in temperature range of 350-600 °C resulting in proton conductivity of $\geq 0.5-1 \times 10^{-3} \text{ Scm}^{-1}$ [22], [23]. The oxygen vacancy conductivity of several cathode materials on Y-stabilized zirconia electrolyte for which the bulk path is known to be active is shown in Figure 1-5 (in grey). The proton conductivity of BSFZn and the typical proton-conducting

electrolyte, $\text{BaZr}_{0.8}\text{Y}_{0.2}\text{O}_{3-\delta}$ is also shown (in blue). The results suggest that at intermediate temperatures (e.g., 500 °C), the proton conductivity of BSFZn is comparable with the oxygen vacancy conductivity of the SOFC cathode materials such as LSC and LSF with active bulk path. This qualitatively suggests that the bulk path is active for BSFZn. Microelectrode measurements indeed showed that the oxygen reduction activity scaled with the squared diameter of a dense microelectrode, i.e., cathode area rather than circumference [24]. For BSFZn, the measured proton diffusivities were comparable to that of electrolyte materials [22], [23]. The decisive parameter which determines whether the bulk path is active for a certain cathode material is then the proton concentration.

This work mainly focuses on mixed-conducting perovskites as potential cathode materials in proton-conducting ceramic fuel cells. The effects of element substitution on the A- and B-site of the perovskite on proton uptake are studied in particular. Thermogravimetry is applied in dry and humid oxidizing condition and different temperatures to characterize the defect chemistry of the triple-conducting cathode materials with holes, protons, and oxygen vacancies as charge carriers. The main work is done on Fe-containing perovskites, but some Co-containing ones such as BCFZr and BSCF are also studied, as Co is known to increase the cathode catalytic activity and electronic conductivity. Changing the conditions $p\text{O}_2$, $p\text{H}_2\text{O}$, and T , the change of proton uptake mechanisms from hydration, to mixed hydration-hydrogenation to hydrogenation regime can be traced. The results show that defect interactions cannot be neglected. They are studied by TG and quantified by means of a first order correction. High proton concentrations are found specifically in Zn-containing cathode materials. The fundamental relation between hydration thermodynamics and element substitution is thoroughly discussed, e.g., by means of defining ion electronegativity. The results are further confirmed by complementary methods of determining proton uptake such as Karl-Fischer titration and mass spectroscopy. This work provides strategies for designing a better cathode material.

Not only do cathode materials simultaneously contain oxygen vacancies, protons, and holes, but under certain conditions the presence of holes is also relevant for $\text{Ba}(\text{Zr,Ce,Y})\text{O}_{3-\delta}$ electrolyte materials. This may lead to a peculiar two-fold kinetics after $p\text{H}_2\text{O}$ and corresponding stoichiometry change [25]–[27]. In the present work, earlier studies are significantly extended to model the thermodynamics and then relaxation kinetics of ideally dilute triple-conducting perovskites upon $p\text{H}_2\text{O}$ change at different $p\text{O}_2$ and T . The effect of hole trapping is now incorporated in the model and in particular, activation energy of the phenomenological diffusion coefficients is investigated in detail.

The presence of a non-negligible hole concentration in BZY electrolyte materials at high $p\text{O}_2$ leads to electronic leakage in gas symmetric cells at high $p\text{O}_2$, which is a major challenge for determination of the surface reaction kinetics of the cathode materials. A fundamental solution is to apply alternative electrolytes with relatively lower electronic transference

numbers compared to typical BZY. A number of potential electrolytes are studied in this work. These alternative electrolytes are then used to perform microelectrode measurements to directly measure the surface reaction rate of specific cathode materials.

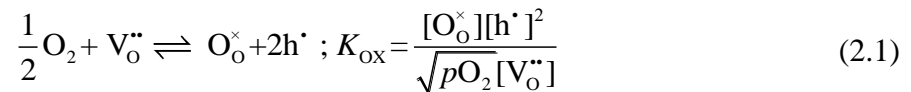
Chapter 2

Theoretical Background

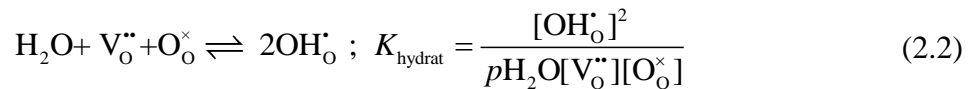
2 Theoretical background

The ideal image of inorganic compounds which assumes non-changing compositions and a perfect crystal structure started to change in the beginning of the 20th century. In fact, depending on the temperature and partial pressure, all inorganic compounds can be non-stoichiometric and their crystal structure will be imperfect [28]. These crystal imperfections or *defects* can be categorized into (i) point defects, (ii) line defects, and (iii) plane defects. The point defects refer to zero-dimensional imperfection in the lattice site or its surroundings; e.g., the vacant position of an oxide ion in a solid oxide (oxygen vacancy), or electronic defects (excess electrons or missing electrons = electron holes). In this work, only point defects including ionic and electronic defects are considered. They determine properties such as electronic and ionic conductivity of solid oxides and -in contrast to higher dimensional defects- can be equilibrated in a reasonable time scale. The commonly used Kröger-Vink notation is selected here to denominate the point defects. The oxide ion O²⁻ on its lattice site is denoted as O_O[×] where the subscript O represents the lattice site and the superscript × indicates the defect charge relative to the ideal lattice which is neutral in this case. Oxygen vacancies can be denoted as V_O^{''} which refers to positively double charged (superscript) vacant position at the oxygen lattice site (subscript). The protons are bound to oxide ions by a short covalent bond (~ 1 Å). The resulting protonic defect OH_O['] (hydroxide on an oxide site) has a single effective positive charge. Electronic charge carriers, electrons and holes are denoted as h['] and e['], respectively. In this work, dealing with mixed-conducting perovskites, holes, protons, and oxygen vacancies are the relevant electronic and ionic defects.

The equilibration with the gas phase for oxides that contain oxygen vacancies can be expressed by the oxygenation reaction (redox reaction)



([i] indicates the concentration of the defect i) and hydration reaction (dissociative absorption of water by acid-base reaction)



The right hand side terms of eq. (2.1) and eq. (2.2) give the respective mass action laws for dilute condition. Solving these two equations together with electroneutrality condition

$$[\text{A}'] = 2[\text{V}_\text{O}''] + [\text{OH}_\text{O}'] + [\text{h}'] \quad (2.3)$$

and oxygen site balance

$$3=[V_o^{\bullet\bullet}]+[OH_o^{\bullet}]+[O_o^{\times}] \quad (2.4)$$

one can derive defect concentrations as a function of the thermodynamic variables. Figure 2-1 (a) is a “material map” in which four types of materials are specified. (i) Oxygen vacancy conducting oxides such as yttria-doped zirconia (YSZ) or samaria-doped ceria which are applied as electrolyte in oxide-ion conducting ceramic fuel cells, (ii) perovskites with oxygen vacancy and hole conductivity such as $La_{0.5}Sr_{0.5}CoO_{3-\delta}$ which are used as cathode electrode in O^{2-} -SOFCs, (iii) proton-conducting electrolytes such as Y-doped $BaZrO_{3-\delta}$ or $BaCeO_{3-\delta}$ which are fully hydrated at lower temperatures and are candidates for PCFC electrolytes, and finally (iv) proton and hole conducting perovskites which are potential cathode materials for PCFCs, e.g. BSCF.

Another possibility of proton incorporation is the hydrogenation reaction which is the combination of hydration and oxygenation (not an independent reaction)

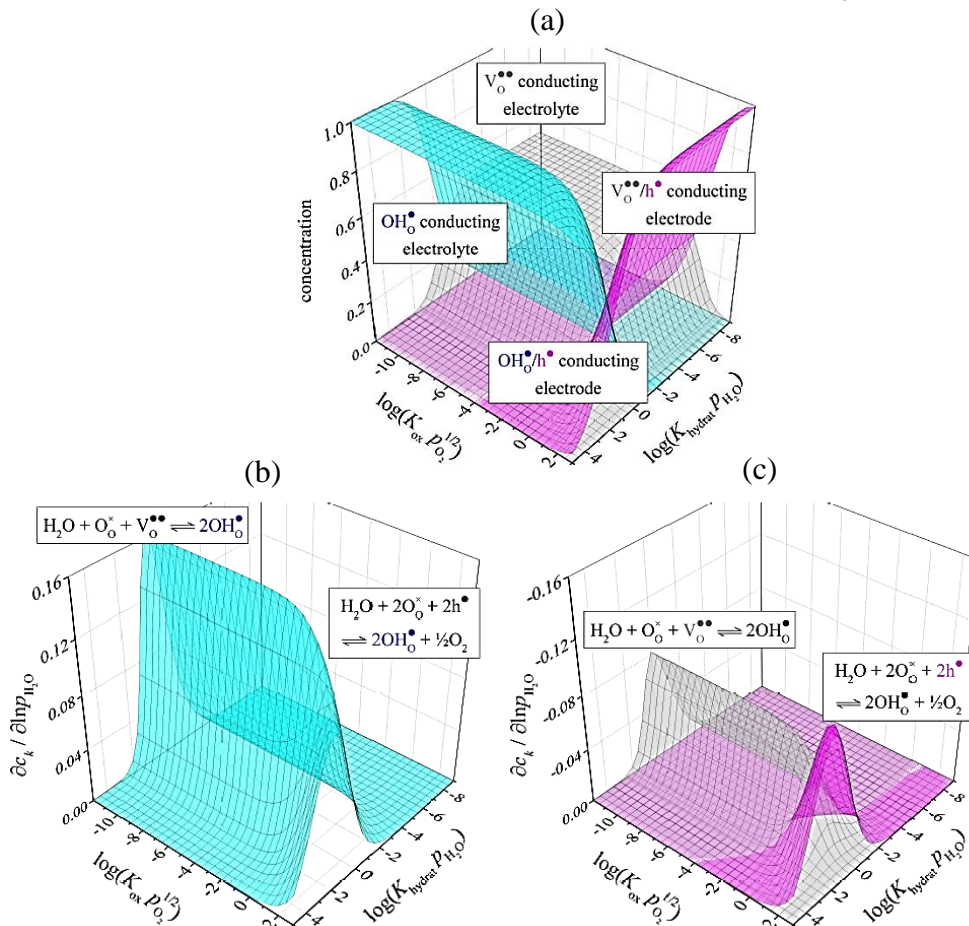
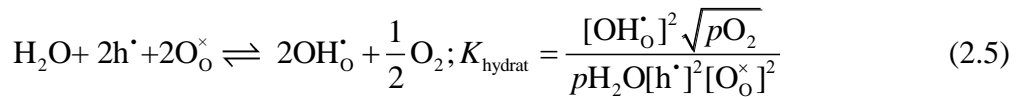


Figure 2-1: (a) Defect concentration including oxygen vacancies (grey), protons (blue) and holes (pink) as a function of $K_{\text{ox}} \sqrt{p_{\text{O}_2}}$ and $K_{\text{hydrat}} p_{\text{H}_2\text{O}}$. (b). change in proton concentration as a function of $K_{\text{ox}} \sqrt{p_{\text{O}_2}}$ and $K_{\text{hydrat}} p_{\text{H}_2\text{O}}$ (c) change in oxygen vacancy and hole concentration as a function of $K_{\text{ox}} \sqrt{p_{\text{O}_2}}$ and $K_{\text{hydrat}} p_{\text{H}_2\text{O}}$ [25].

Figure 2-1 (b) and (c) show the defect concentration changes as the material is exposed to humidity. According to Figure 2-1 (b) the proton concentration increases at the expense of holes through hydrogenation, or by consumption of oxygen vacancies in the hydration reaction. At equilibration, both processes happen simultaneously with the preference determined by the thermodynamics. It has been shown numerically and analytically that the borderline where both pathways of proton uptake contribute equally is given by the condition for which $2[V_{\text{O}}^{\bullet\bullet}] = [h^{\bullet}]$ (under ideally dilute condition). When hole concentration is high (typical for a cathode perovskite, especially at low T and high $p\text{O}_2$) the system is in the hydrogenation regime. Most of the measurements in section 4.2 will be performed under conditions of predominant hydration.

So far, the defect chemistry is established based on this assumption that the system is ideally dilute, i.e., there is no interaction between defects. This will not necessarily hold for systems with high hole concentration, e.g., the cathode perovskites. As will be discussed later in 4.2, a high concentration of trapped holes on the transition metal on the B-site of a perovskite can affect the thermodynamics of the system significantly. Any deviation from the ideal behavior (linear van 't Hoff plot, independent of partial pressures) suggests that there is defect interaction. A “first order correction” will be applied in section 4.2.5 to quantify such non-idealities.

The stoichiometry relaxation upon $p\text{O}_2$ and $p\text{H}_2\text{O}$ change is an important process for these perovskites. Assuming a fast oxygen/water surface exchange reaction and/or large sample thickness L ($L > L_{\text{crit}}, L_{\text{crit}} \equiv 2D/k$; D diffusion coefficient, k effective surface exchange rate constant) the kinetics is diffusion-controlled [29]. The relevant transport parameter is the ambipolar or chemical diffusion coefficient D^{δ} . For a system with two charge carriers, e.g., holes and oxygen vacancies, one can ideally write

$$D_{\text{O}}^{\delta} = t_{\text{h}} \cdot D_{\text{V}_{\text{O}}^{\bullet\bullet}} + t_{\text{V}_{\text{O}}^{\bullet\bullet}} \cdot D_{\text{h}}. \quad (2.6)$$

where D_j and t_j denote the diffusion coefficient and the transference number of defect j . However, in some systems such as in Fe-doped SrTiO_3 where holes can be trapped on the transition metal ($\text{Fe}'_{\text{Ti}} + h^{\bullet} \rightleftharpoons \text{Fe}^{\times}_{\text{Ti}}$) the chemical diffusion is modified considering the trapping factor $\chi_{\text{h}}^{\bullet}$. [30]–[32]

$$\chi_{\text{h}}^{\bullet} = \frac{\partial[h^{\bullet}]}{\partial[h^{\bullet}] + \partial[\text{Fe}^{\times}_{\text{Ti}}]} \quad (2.7)$$

resulting in

$$D_{\text{O}}^{\delta} = \frac{\sigma_{\text{h}}^{\bullet}}{\sigma} D_{\text{V}_{\text{O}}^{\bullet\bullet}} + \frac{\sigma_{\text{V}_{\text{O}}^{\bullet\bullet}}}{\sigma} \chi_{\text{h}}^{\bullet} \cdot D_{\text{h}}. \quad (2.8)$$

In systems with more than two charge carriers which are not necessarily in mutual equilibrium, peculiar relaxation kinetics such as non-monotonic change of conductivity with two characteristic time constants (“two-fold relaxation kinetics”) has been observed. This has been first reported for $p\text{H}_2\text{O}$ changes on slightly Fe-doped SrTiO_3 single crystals at high $p\text{O}_2$ and T by space-resolved optical spectroscopy [26], [27] and then, also for acceptor-doped $(\text{Ba,Sr})(\text{Zr,Ce})\text{O}_3$ at high T and $p\text{O}_2$ [33]–[36]. Qualitatively, one can assign this to the fast hydrogenation followed by slow oxygenation so that the overall reaction still remains hydration. The holes can transiently decouple the oxygen vacancy and proton flux.

Assuming negligible defect interactions, the defect fluxes can be written as

$$\begin{pmatrix} J_{\text{V}_\text{O}^\bullet\bullet} \\ J_{\text{OH}_\text{O}^\bullet} \\ J_{\text{h}^\bullet} \end{pmatrix} = \frac{-1}{F^2} \begin{pmatrix} \frac{\sigma_{\text{V}_\text{O}^\bullet\bullet}}{4} & 0 & 0 \\ 0 & \sigma_{\text{OH}_\text{O}^\bullet} & 0 \\ 0 & 0 & \sigma_{\text{h}^\bullet} \end{pmatrix} \begin{pmatrix} \nabla \tilde{\mu}_{\text{V}_\text{O}^\bullet\bullet} \\ \nabla \tilde{\mu}_{\text{OH}_\text{O}^\bullet} \\ \nabla \tilde{\mu}_{\text{h}^\bullet} \end{pmatrix} \quad (2.9)$$

where J refers to flux and $\nabla \tilde{\mu}$ is the gradient of the electrochemical potential. The flux of each charge carrier is then related to the concentration gradients of *all other defects* which are not necessarily linked by simple prefactors, since electroneutrality holds only for all charge carriers together. As a result, the fluxes are expressed as a function of $\nabla c_{\text{V}_\text{O}^\bullet\bullet}$ and $\nabla c_{\text{h}^\bullet}$ (c refers to concentration) as [25],[34]:

$$J_{\text{V}_\text{O}^\bullet\bullet} = [-(D_{\text{V}_\text{O}^\bullet\bullet} + t_{\text{V}_\text{O}^\bullet\bullet}(D_{\text{OH}_\text{O}^\bullet} - D_{\text{V}_\text{O}^\bullet\bullet}))]\nabla c_{\text{V}_\text{O}^\bullet\bullet} + [-0.5t_{\text{V}_\text{O}^\bullet\bullet}(D_{\text{OH}_\text{O}^\bullet} - D_{\text{h}^\bullet})]\nabla c_{\text{h}^\bullet} \quad (2.10)$$

$$J_{\text{OH}_\text{O}^\bullet} = [2(D_{\text{OH}_\text{O}^\bullet} + t_{\text{OH}_\text{O}^\bullet}(D_{\text{V}_\text{O}^\bullet\bullet} - D_{\text{OH}_\text{O}^\bullet}))]\nabla c_{\text{V}_\text{O}^\bullet\bullet} + [D_{\text{OH}_\text{O}^\bullet} + t_{\text{OH}_\text{O}^\bullet}(D_{\text{h}^\bullet} - D_{\text{OH}_\text{O}^\bullet})]\nabla c_{\text{h}^\bullet}$$

The four terms in brackets show that four diffusion coefficients are required to describe the system. Numerically solving these equations gives an understanding of the diffusion kinetics in systems with three charge carriers. The fast carriers (holes and protons in this case) can respond to the driving force without being delayed by the slow species (oxygen vacancies) and the acid-base reaction is decomposed into two redox reactions with different characteristic times. For these systems, the following four phenomenological diffusion coefficients describe the kinetics: $D_{\text{H}}^{\text{eff}}$, $D_{\text{O}}^{\text{eff}}$ (from e.g., transient thermogravimetry measurements yielding ionic defect concentration changes) and D_{fast} , D_{slow} (from transient behavior of conductivity yielding electronic defect concentration changes). The possible relaxation processes in such triple-conducting oxides are illustrated in Figure 2-2. When t_{h^\bullet} is small, the single-fold relaxation process is predominant and $D_{\text{H}}^{\text{eff}} \approx D_{\text{O}}^{\text{eff}} \approx D_{\text{H}_2\text{O}}^\delta$ while the two-fold stoichiometry relaxation appears at higher t_{h^\bullet} and would meet the condition $D_{\text{H}}^{\text{eff}} \approx D_{\text{OH}_\text{O}^\bullet}$, $D_{\text{O}}^{\text{eff}} \approx D_{\text{V}_\text{O}^\bullet\bullet}$ when $t_{\text{h}^\bullet} \approx 1$. In section 4.1, the effect of hole trapping on two-fold

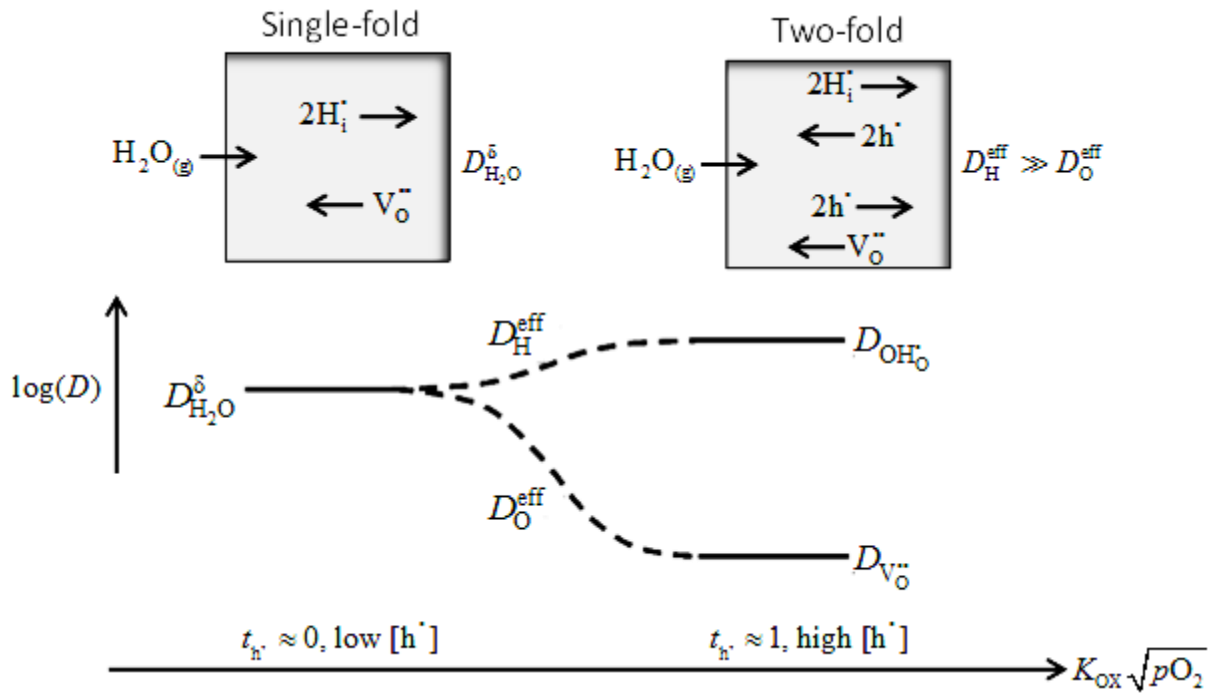


Figure 2-2: Possible stoichiometry relaxation processes upon $p_{\text{H}_2\text{O}}$ change in the gas phase [25].

relaxation will be investigated with the help of finite differences simulations.

Chapter 3

Experimental

3 Experimental

3.1 Sample preparation

The following electrolyte and cathode materials are investigated in this work (Please note that the abbreviations, B for Ba, C for Co, *etc.* should not be considered as elements boron, carbon, *etc.*):

Electrolytes- BaZr_{1-x-y}Ce_yY_xO_{3-δ} (BZCY): BZC80Y3 (i.e., $x = 3$, $y = 80$), BZC80Y1.2, BZC50Y3, BZC20Y1, BZC10Y1; also, La₂₇W₅O_{54+δ} (LWO), and La₂₇(W_{3.5}Mo_{1.5})O_{54+δ} (Mo-LWO).

Cathodes- SrFeO_{3-δ} (SF), Ba_{0.5}Sr_{0.5}FeO_{3-δ} (BSF), Ba_{0.5}Sr_{0.5}Co_{0.8}Fe_{0.2}O_{3-δ} (BSCF), La_{0.5}Sr_{0.5}FeO_{3-δ} (LSF), La_{0.5}Sr_{0.5}CoO_{3-δ} (LSC), Ba_{0.95}La_{0.05}FeO_{3-δ} (BL5F), Ba_{0.85}La_{0.15}FeO_{3-δ} (BL15F), Ba_{0.75}La_{0.25}FeO_{3-δ} (BL25F), Ba_{0.5}La_{0.5}FeO_{3-δ} (BL50F), Ba_{0.95}La_{0.05}Fe_{0.8}Zn_{0.2}O_{3-δ} (BL5FZn20), Ba_{0.5}Sr_{0.5}Co_{0.8}Nb_{0.2}O_{3-δ} (BSCN), Ba_{0.5}Sr_{0.5}Fe_{0.8}Zn_{0.2}O_{3-δ} (BSFZn), SrFe_{0.8}Zn_{0.2}O_{3-δ} (SFZn) and, BaCo_{0.4}Fe_{0.4}Zr_{0.2}O_{3-δ} (BCFZr).

3.1.1 Powder preparation

Solid state synthesis- All electrolytes as well as SF, BSF, BSCF, LSF, and LSC were prepared using classical solid state reaction. Stoichiometric amounts of starting powders including BaCO₃ (Alfa Aesar, 99%, Germany), Zr_{1-x}Y_xO_{2-δ} (Tosoh, TZ-0Y, TZ-3Y, TZ-8Y, Japan), CeO₂ (Alfa Aesar, 99.9%, Germany), La₂(CO₃)₃.xH₂O (Alfa Aesar, 99.9%, Germany), SrCO₃ (Sigma Aldrich, ≥ 99.9%, USA), Fe₂O₃ (Sigma Aldrich, ≥ 99%, USA), and Co₃O₄ (Alfa Aesar, 99.7%, Germany) were mixed in an agar mortar and calcined at certain T (see Table 3-1) followed by a sequence of post-annealing and ball milling until predominant perovskite phase (except for LWO and Mo-LWO which have fluorite crystal structure) was achieved. As La₂O₃ easily forms carbonates and adsorbs humidity, the starting powder was annealed at 900 °C for half an hour (heating rate 600 °C/h, cooling rate as fast as possible) and the powder was immediately weighted.

Wet chemical synthesis- The rest of the materials was synthesized starting from aqueous nitrate solutions. The procedure is briefly explained here for BCFZr and is similar for the other materials [5], [37]. Stoichiometric amounts of starting powders including Ba(NO₃)₂ (Alfa Aesar, ≥ 99%, Germany), Co(NO₃)₂.6H₂O (Sigma Aldrich, ≥ 98%, USA), Fe(NO₃)₃.9H₂O (Alfa Aesar, ≥ 98%, Germany), and ZrO(NO₃)₂.xH₂O (Aldrich, USA) were mixed with Ethylenediaminetetraacetic (EDTA, Alfa Aesar, 99%, Germany) and citric acid (Carl Roth, ≥99.5%, Germany) with a molar ratio of $\Sigma\text{cations}:n_{\text{EDTA}}:n_{\text{CA}} = 1:1.5:1$ (for each mole of cations, 1.5 and 1 mole of EDTA and citric acid are used). Water content, x , has been determined by thermogravimetry. The pH value was adjusted to 9 using aqueous ammonia solution while heating and stirring the solution constantly. At 200 °C, the stirrer was removed

and the hot plate temperature increased up to 500 °C to induce combustion. To complete the combustion, the resulting ash was ground repeatedly in an agar mortar and placed back in the beaker at 500 °C until no traces of combustion was observed. The final product was ground again, calcined in an alumina crucible at 1100 °C for 10 h in air and ball milled for an hour.

Table 3-1 summarizes the calcination conditions for different materials. Between the heating steps, the powders were dry ball milled for an hour. After synthesis, the phase purity and chemical composition of the powder was checked by X-ray diffraction and inductively coupled plasma optical emission spectroscopy (ICP-OES).

Table 3-1 Material synthesis: calcination condition and the respective lattice parameter (*a*).

Material	calcination	<i>a</i> / pm
BZC80Y3 BaZr _{0.17} Ce _{0.8} Y _{0.03} O _{3-δ}	(1200 °C,4h)×1 + (1300 °C,10h)×2	predominantly orthorhombic ¹
BZC80Y1.2 BaZr _{0.188} Ce _{0.8} Y _{0.012} O _{3-δ}	(1200 °C,4h)×1 + (1300 °C,10h)×2	predominantly orthorhombic ²
BZC50Y3 BaZr _{0.47} Ce _{0.5} Y _{0.03} O _{3-δ}	(1200 °C,4h)×1 + (1300 °C,10h)×2	not single phase ³
BZC20Y1 BaZr _{0.79} Ce _{0.2} Y _{0.01} O _{3-δ}	(1200 °C,4h)×1 + (1300 °C,4h)×2	2 cubic phases ⁴
BZC10Y1 BaZr _{0.89} Ce _{0.1} Y _{0.01} O _{3-δ}	(1200 °C,4h)×1 + (1300 °C,4h)×2	421
LWO La ₂₇ W ₅ O _{54+δ}	(1100 °C,4h)×2 + (1300 °C,4h)×1	2 cubic phases ⁵
Mo-LWO La ₂₇ (W _{3.5} Mo _{1.5})O _{54+δ}	(1100 °C,4h)×2 + (1300 °C,4h)×1	not single phase ⁶
SF SrFeO _{3-δ}	(1050 °C,4h)×3	not single phase ⁷
BSF Ba _{0.5} Sr _{0.5} FeO _{3-δ}	(1050 °C,4h)×3	394 (similar to [38])
BSCF Ba _{0.5} Sr _{0.5} Co _{0.8} Fe _{0.2} O _{3-δ}	(1050 °C,4h)×3	398 (similar to [39])
LSF La _{0.5} Sr _{0.5} FeO _{3-δ}	(1050 °C,4h)×3	not single phase ⁸
LSC La _{0.5} Sr _{0.5} CoO _{3-δ}	(1050 °C,4h)×3	383
BL5F Ba _{0.95} La _{0.05} FeO _{3-δ}	(1000 °C, 8h)	399
BL15F Ba _{0.85} La _{0.15} FeO _{3-δ}	(1000 °C, 8h)	398

BL25F $\text{Ba}_{0.75}\text{La}_{0.25}\text{FeO}_{3-\delta}$	(1000 °C, 8h)	396
BL50F $\text{Ba}_{0.5}\text{La}_{0.5}\text{FeO}_{3-\delta}$	(1000 °C, 8h)	394
BL5FZn20 $\text{Ba}_{0.95}\text{La}_{0.05}\text{Fe}_{0.8}\text{Zn}_{0.2}\text{O}_{3-\delta}$	(1000 °C, 8h)	405
SFZn20 $\text{SrFe}_{0.8}\text{Zn}_{0.2}\text{O}_{3-\delta}$	(1000 °C, 8h)	-
BCFZr $\text{BaCo}_{0.4}\text{Fe}_{0.4}\text{Zr}_{0.2}\text{O}_{3-\delta}$	(1100 °C, 4h) × 1	410

1: 96% orthorhombic BaCeO_3 ($878 \times 621 \times 623$ (pm)³), 4% cubic BZY1 (420 pm).

2: orthorhombic BaCeO_3 ($877 \times 622 \times 623$ (pm)³), cubic BZY1 (420 pm), cubic $\text{Ba}_2\text{CeZrO}_{5.5}$ (878 pm).

3: cubic BaCeO_3 (436 pm), cubic BZY1 (420 pm), cubic $\text{Ba}_2\text{CeZrO}_{5.5}$ (857 pm), orthorhombic BaCeO_3 ($878 \times 621 \times 624$ (pm)³).

4: cubic BZY1 (422 pm) and cubic BaCeO_3 (437 pm).

5: cubic $\text{La}_{26.27}\text{W}_5\text{O}_{52.8}$ (1118 pm) and cubic $(\text{La}_2\text{O}_3)_5 \cdot 2\text{WO}_3$ (1118 pm).

6: cubic $\text{La}_{26.27}\text{W}_5\text{O}_{52.8}$, cubic $(\text{La}_2\text{O}_3)_5 \cdot 2\text{WO}_3$ and rhombohedral $\text{La}_6\text{MoO}_{12}$.

7: became cubic after sintering.

8: Orthorhombic LSF, Rhombohedral LSF, tetragonal $\text{La}_2\text{Sr}_2\text{Fe}_2\text{O}_8$ and hexagonal La_2O_3 ; became cubic after sintering.

3.1.2 Pellet preparation

Conventional sintering and spark plasma sintering were used to produce dense pellets depending on the application.

3.1.2.1 Conventional sintering

Isostatic powder compaction or cold isostatic pressing (CIP) is a beneficial dry forming method compared to conventional single action and double action pressing as the sample suffers from less shrinkage during sintering and is more homogenous in shape. The calcined and ball milled powder was pressed ($F = 250\text{-}350$ kN) in a 15 mm rubber mold and sintered in O_2 (to avoid closed porosity) in optimized condition such that the single phase cubic perovskite was maintained. Table 3-2 summarizes the sintering condition for various cathode perovskites investigated in this work. The resulting pellet was either used for conductivity measurements or crushed and sieved to particles for thermogravimetry (TG). SEM images of BL5F, BL5FZn20, and BSF particles are shown in Figure 3-1. The particles are quite dense with no visible porosity and the particle size is, as expected, between 100-250 μm (see 3.1.3).

Table 3-2 Classical sintering for different cathode materials in pure O_2 : sintering temperature (T_{sint}), sintering duration (t_{sint}), lattice parameter (a), and maximum achievable density relative to the theoretical density (ρ/ρ_{th}).

Material	$T_{\text{sint}} / ^\circ\text{C}$	$t_{\text{sint}} / \text{h}$	a / pm	ρ / ρ_{th}
BL5F	1200	10	400	> 90 %
BL15F	1200	10	399	> 90 %
BL25F	1200	10	401	> 90 %
BL50F	1200	10	396	> 90 %
SF	1380	8	386*	82 %
LSF	1400	8	390	83 %
LSC	1200	8	383	74 %
BSF	1200	8	393	> 90 %
BSCF	1200	8	398	85 %
BCFZr	1200	8	410	95 %
SFZn20	1200	8	388	> 90 %
BL5FZn20	1200	8	405	88 %
BSFZn	1200	8	396	97 %
BSCN	1200	5	402	> 90 %

* Air-sintered SF is a cubic perovskite, but after being quenched from 700 $^\circ\text{C}$, it forms orthorhombic Brownmillerite structure with $a = 5.67$ \AA , $b = 5.52$ \AA , and $c = 15.60$ \AA .

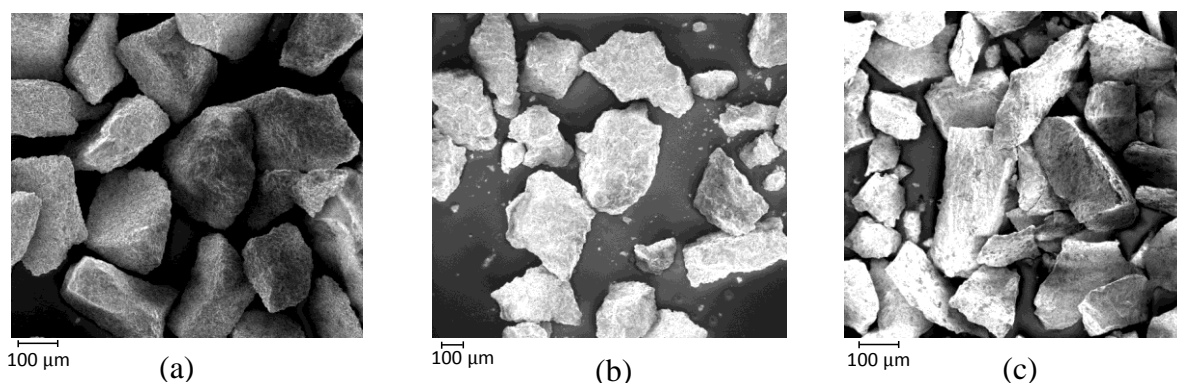


Figure 3-1: Example of SEM images of particles (100-250 μm diameter from crushed pellets) (a) BL5F (b) BL5FZn20, (c) BSF.

3.1.2.2 Spark plasma sintering

Spark plasma sintering (SPS) or more precisely, pulsed electric current sintering (PECS) is a uniaxial single action pressing sintering method (applicable for conducting and non-conducting materials) in which the green body formation and heating occur simultaneously. High heating rates (as high as 1000 Kmin^{-1}) and short holding times (few minutes) are achievable by flowing electric current through the graphite die and the conducting sample while applying uniaxial pressure to it [40]. The density is usually higher for the spark plasma sintered sample compared to conventional sintering and can exceed 95% of the theoretical density by carefully adjusting the sintering conditions.

In this work, HP D 5 (FCT systems GmbH, Germany) was used to sinter electrolyte as well as electrode materials typically using 20 mm tools consisting of dense, pure graphite die and two pistons. The initial powder (usually $\sim 4 \text{ g}$) was compacted inside the die between two pistons and was placed inside the vacuum chamber between two metal pistons which are responsible for applying the load. Whenever necessary, yttria-stabilized zirconia felt (ZYP-50, 0.5 mm thick, Zircar Zirconia, USA) or Platinum foils were placed between the powder and pistons to avoid excessive sample reaction due to direct contact. The pressure inside the chamber was always set to $\sim 25 \text{ mbar}$ during the sintering through two consecutive steps of vacuum and Argon injection. For $T > 1000 \text{ }^\circ\text{C}$, a pyrometer was used to optically read the temperature from top of the set up; otherwise, a thermocouple inserted in the middle of the die reads T (Figure 3-2). Typically, a heating rate of 100 Kmin^{-1} , maximum cooling rate achieved by switching off the electric current, and 50 MPa mechanical pressure was used in this work. The outmost layers of the spark plasma sintered pellets were ground off using silicon carbide polishing paper and the pellets were given a heat treatment at suitable T in air to remove the remaining graphite on the surface. The BZCY electrolyte materials were packed in between commercial BaZrO_3 (Sigma-Aldrich, USA) powder beforehand to minimize Ba loss during the post-annealing at high T . After polishing the surface once more, the phase purity of the pellets was checked by XRD. Table 3-3 summarizes the optimized sintering and post-annealing condition for spark plasma sintered pellets and the respective lattice

parameters extracted from X-ray measurements. The post annealing heating/cooling rate is typically $150\text{-}300\text{ Kh}^{-1}$. Figure 3-3 depicts the change of unit cell volume of BZCY series with different Ce and Y substitution with Zr content compared to the literature data (black spheres) [2].

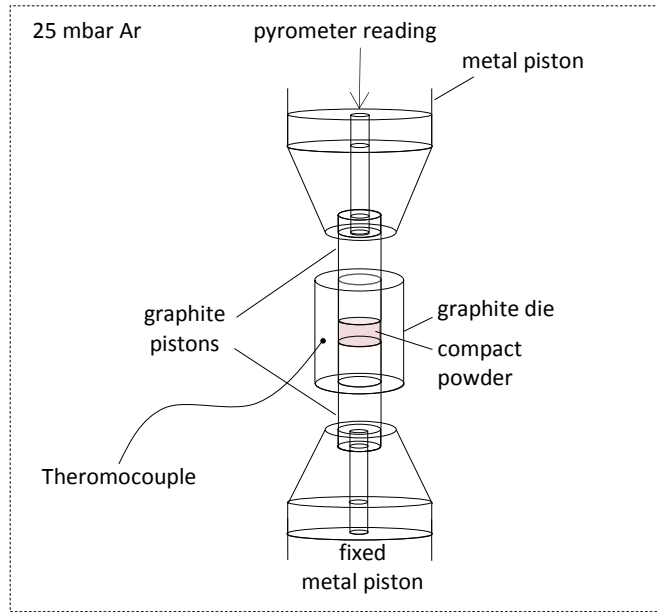


Figure 3-2: SPS configuration: The powder is compacted between graphite pistons under pressure at high T .

Table 3-3 Optimized sintering conditions for spark plasma sintered materials: sintering temperature (T_{sint}), sintering duration (t_{sint}), post annealing temperature ($T_{p.a}$), post annealing duration ($t_{p.a}$), lattice parameter (a).

Material	$T_{sint} / ^\circ\text{C}$	t_{sint} / min	$T_{p.a} / ^\circ\text{C}$	$t_{p.a} / \text{h}$	a / pm
LWO	1300	3	1500	12	1118
Mo-LWO	1300	5	1500	12	1118
BZC80Y3	1300	5	1600	1	predominantly orthorhombic ¹
BZC80Y1.2	1300	5	1600	1	predominantly orthorhombic ²
BZC50Y3	1400	5	1400	1	not single phase ³
BZC20Y1	1400	5	1600	20	421
BZC10Y1	1400	5	1600	20	420
BL5FZn20 ⁴	950	3	800	2	407

1: orthorhombic BC9Y1 ($917 \times 596 \times 660$ (pm)³) and cubic BZY1 (419 pm).

2: orthorhombic BaCeO₃ ($920 \times 651 \times 593$ (pm)³), cubic BaZrO₃ (441 pm), cubic Ba₂CeZrO_{5.5} (900 pm).

3: cubic BaCeO₃, cubic BZY1, cubic Ba₂CeZrO_{5.5}.

4: The initial powder was pretreated in N₂ at 800 °C for half an hour. Pt foil was used as buffer layer.

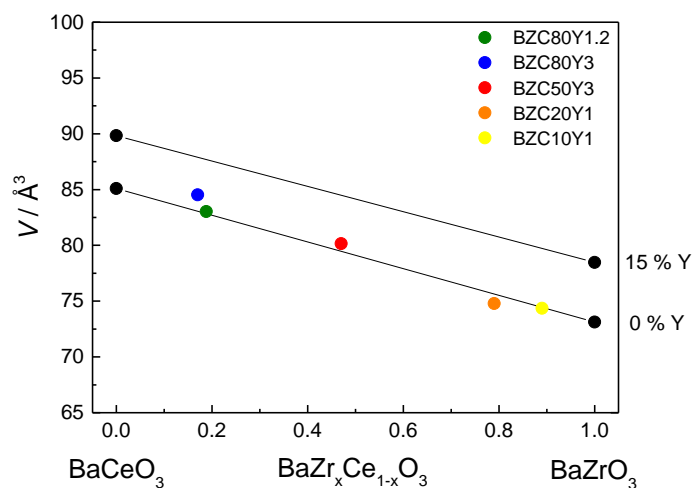


Figure 3-3: Unit cell volume vs. Zr content in $\text{BaZr}_x\text{Ce}_{1-x}\text{O}_3$ with different yttrium substitution. The black spheres refer to [2].

3.1.3 Particle preparation for TG

After grinding off the outermost layer of the conventionally sintered pellet, it was crushed and sieved to particles of 100-250 μm size to be used in TG measurements in humid conditions. Such a particle size helps to avoid errors by surface water adsorption while still allowing for moderate equilibration times after $p\text{O}_2$ and $p\text{H}_2\text{O}$ changes. As grain boundaries are not blocking for the cathode perovskites (see e.g., [23]), the particle size is the main determining factor for equilibration times.

3.1.4 Pulsed laser deposited samples: Microelectrodes

Microelectrode cathodes are used in microelectrode measurements as a standard way of studying the catalytic activity of cathode materials and its dependence on several control parameters including T , $p\text{O}_2$, $p\text{H}_2\text{O}$, diameter, *etc.* Pulsed laser deposition (PLD) is used to deposit the 100 nm thick cathode layer on the electrolyte substrate. As PLD is performed at temperatures as high as 800 $^\circ\text{C}$, the chemical compatibility of the electrolyte and cathode at high T should be examined. LWO and selected materials including BCFZr, BSFZn, BSCF, LSF, LSC, and BZY1 were mixed 1:1 by volume in a mortar. The mixture was divided into two series and calcined for 3 days at 600 $^\circ\text{C}$ and 800 $^\circ\text{C}$ in air. Comparison of the XRD before and after calcination suggests that LWO reacts with Ba-rich cathode materials while no reaction occurred with BZY1. The XRD of LWO-BSFZn mixture before and after annealing shown in Figure 3-4 confirms the reaction at high T .

Spark plasma sintered pellets of selected electrolyte materials (LWO and BZC10Y1) were cut into $5 \times 5 \times 0.5 \text{ mm}^3$ pieces and were then polished on one side to optical quality (Plastic Polish HPA10, Pipelow & Brandt, Germany) in the crystal preparation group of Max Planck Institute for Solid State Research. As LWO reacts with Ba-rich cathode materials, a 10 nm layer of BZY15 was pulsed laser deposited on top of it at 750-770 $^\circ\text{C}$ and 10^{-4} mbar O_2

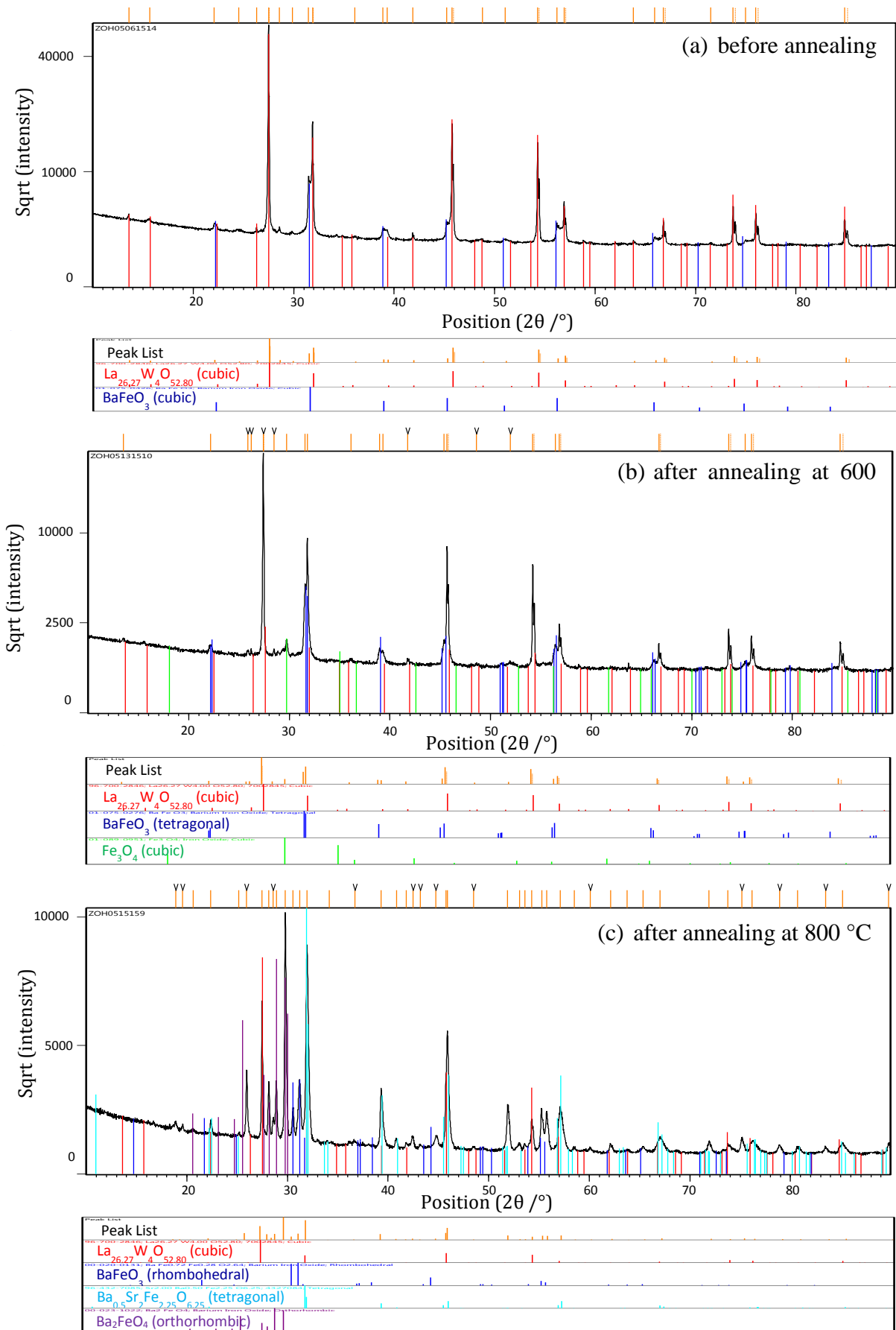


Figure 3-4: X-ray diffraction of the LWO-BSFZn mixture before (a) and after annealing at 600 °C (b) and 800 °C (c) for three days.

(laser pulse frequency = 10 Hz, energy density = $1.6\text{-}3\text{ Jcm}^{-2}$) at the technology service group of MPI FKF. The resulting pieces were used as substrate in PLD to deposit 100 nm thick layers of BSFZn and BCFZr at 770 °C and 0.4 mbar O₂ (laser pulse frequency = 5 Hz, pulse energy of typically 660 mJ, 30 min post annealing at 770 °C after deposition) to achieve dense thin films according to SEM. By grazing incidence X-ray diffraction, the substrate, thin buffer layer and cathode crystal structure were identified. The cathode was then structured to microelectrodes of 20, 40, 60, 80, and 100 μm diameter (Frank Baumann mask [41]) by photolithography and Ar ion beam etching.

In order to have porous cathodes, the laser repetition frequency was increased to 10 Hz and the oxygen partial pressure to 1.2-2 mbar, following the condition used in ref. [42]. In another attempt, the PLD was performed at room temperature in 0.4 mbar O₂ to deposit an amorphous layer of the cathode and then the sample was annealed at 850 °C for 2 h (heating rate: 10 Kmin⁻¹ up to 750 °C and 1 Kmin⁻¹ afterwards, cooling rate: 10 Kmin⁻¹) to form a poly-crystalline cathode with high porosity.

To prepare the counter electrode, silver foil (25 μm, Chempur, Germany) was attached to a 0.1 mm sapphire substrate (Crys Tec, Berlin) by means of silver paste (Demetron, Germany) and annealed at 700 °C in air for 2-3 h. The sample was then attached to it using Ag paste and was baked at 400 °C for half an hour to evaporate the organic binder.

The SEM image of the dense and porous BSCF microelectrodes on BZC10Y1 substrate is shown in Figure 3-5.

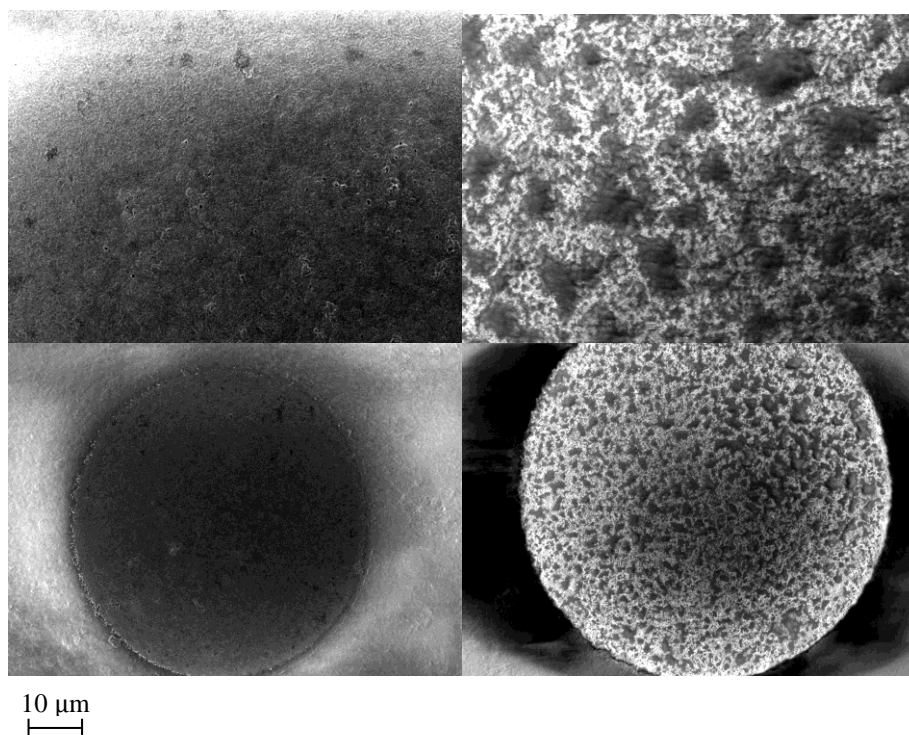


Figure 3-5: SEM image of the dense (left) and porous (right, 1.2 mbar O₂) BSCF microelectrodes on proton-conducting substrate (BZC10Y1).

3.2 Characterization techniques

3.2.1 X-ray diffraction (XRD)

Room temperature X-ray diffraction was used for phase identification and purity determination on a Panalytical diffractometer EMPYREAN, equipped with a PIXcel 3D detector, using CuK_α radiation ($\lambda = 1.541874 \text{ \AA}$, 40 kV, 40 mA). Samples were measured in Bragg-Brentano geometry and lattice parameters were refined using HighScore Plus, V3.0e. Grazing incidence measurements were carried out with parallel beam optics, using an incident angle of 2° .

3.2.2 Inductively coupled plasma optical emission spectroscopy (ICP-OES)

The accurate cation stoichiometry of the synthesized perovskite powders was measured by ICP-OES (Spectro Ciros CCD, Spectro Analytical Instruments, Germany) in the analytical chemistry lab of Max Planck Institute for Intelligent Systems. The measurements were carried out on the solutions obtained by high pressure microwave assisted decomposition in HCl, HNO_3 or HF (depending on the sample).

3.2.3 Thermogravimetry coupled with mass spectroscopy (TG-MS)

Thermogravimetry (STA 449 C Jupiter, Netzsch, Germany) is used to quantify the defect chemistry of different cathode materials. This thermo-microbalance consists of a gas tight assembly which can be used in inert, oxidizing, reducing, static and dynamic condition in T range up to 1650°C with heating and cooling rate of $0.01\text{-}50 \text{ Kmin}^{-1}$. The TG resolution is $0.1 \mu\text{g}$ (this is not however practically achievable due to noisy baseline) with weighting range of 5000 mg. A quadrupole mass spectrometer (QMS 200 F1, balzers Prisma, Germany) with mass range of 1-100 amu coupled to the system is used to monitor the exhaust gas.

Thermogravimetry was carried out with typically 3-4 g of sample in an alumina crucible and a gas flow of 60 mlmin^{-1} . Oxygen partial pressure was controlled by mixing O_2 , 1000 ppm O_2 in N_2 , 1 % O_2 in N_2 and N_2 using mass flow controllers. Under humid conditions, water partial pressure $p_{\text{H}_2\text{O}}$ was adjusted by bubbling the gas stream through a thermostated water evaporator running at 5, 12, or 18°C . The flow of 10 mlmin^{-1} “protective gas” through the balance compartment of the STA 449 was always kept dry. The oxygen and water partial pressures are measured independently by an oxygen analyzer Rapid 2100 (cambridge sensotec, UK) and humidity sensor Hygroclip (rotronic, Germany). The schematic of the TG-MS set up with all gas connections is shown in Figure 3-6.

For non-isothermal measurements buoyancy changes were measured with a crucible filled with an appropriate amount of inert alumina ceramics and then subtracted from the sample weight changes. For isothermal $p\text{H}_2\text{O}$ changes, the measured buoyancy effects were negligible. The buoyancy for isothermal $p\text{O}_2$ changes was small in N_2 and 1% O_2 and was corrected for higher $p\text{O}_2$ s.

3.2.3.1 Oxygen non-stoichiometry measurements

The sample (fine powder or particles) weight was measured in dry oxidizing condition for stepwise T changes between 250 and 900 °C. The necessary equilibration times in 100 ppm O_2 for BCFZr particles decreased from 60 h at 250 °C to 8 h (or less) at 500 °C and above, in pure O_2 the equilibration (largely surface reaction controlled) was faster, also for the powder with approximately 1 μm particle size.

The absolute oxygen non-stoichiometry of BCFZr was determined from reducing a small amount of sample (~ 100 mg) in $\sim 6\%$ H_2 (in N_2) at 1100 °C in the TG such that BCFZr fully decomposed to oxides with known oxidation state and metals (Co and Fe) as confirmed by XRD. For ferrates, the absolute oxygen stoichiometry was determined from the weight plateaus at high T and low $p\text{O}_2$ where all Fe ions are in their 3+ oxidation state.

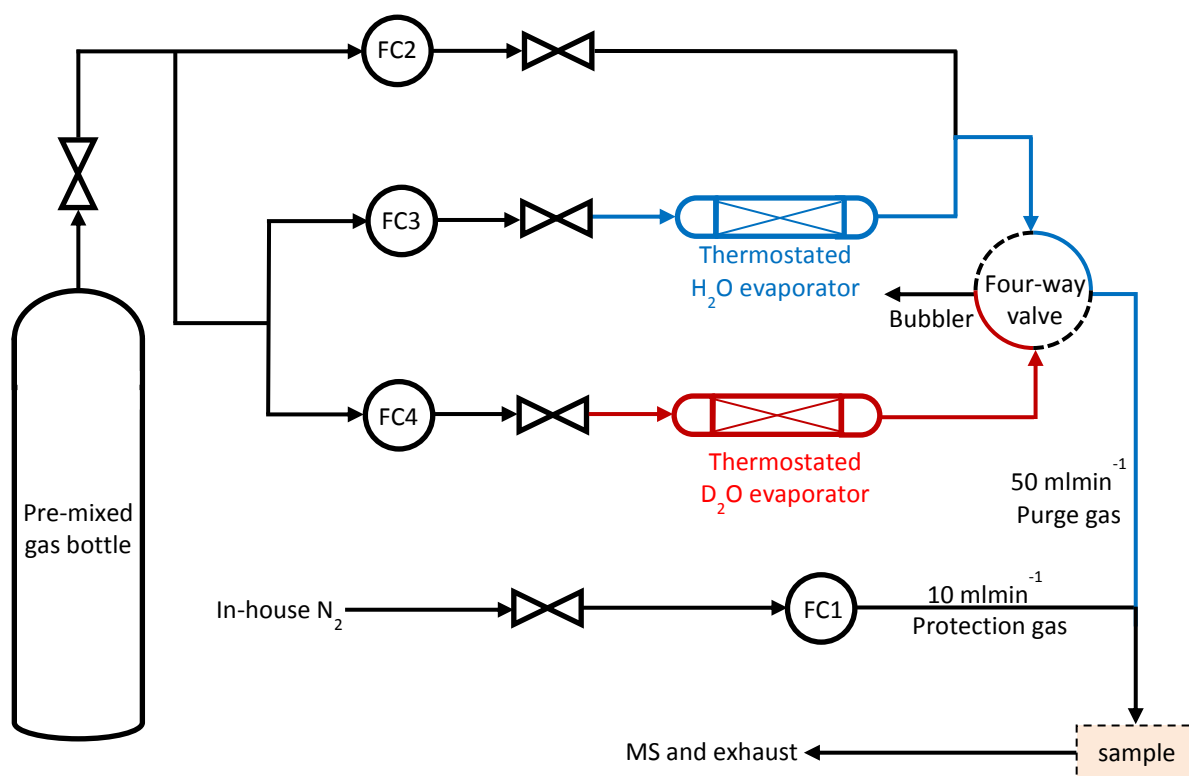


Figure 3-6: Schematic of thermogravimetric set up and its configuration. The dry path is shown in black and the humidified paths are in blue and red. The mixture of gases coming from humid and dry path flows to the sample. For instance, with 40 mlmin⁻¹ of the dry 100% O_2 , 10 mlmin⁻¹ of humid O_2 (thermostat at 5°C) and 10 mlmin⁻¹ of N_2 as protection gas, the sample experiences 60 mlmin⁻¹ of 83% O_2 with 1.45 mbar H_2O .

3.2.3.2 Proton incorporation measurements

Oxygen equilibrated samples- For fully equilibrated measurements, the particles were equilibrated with given T and pO_2 . In order to accelerate the oxygen equilibration in low pO_2 where the process is slow (surface reaction is limiting), a higher pO_2 was applied until the sample was close to the expected oxygen stoichiometry.

Quenched samples- Measurements of proton uptake were also performed under condition of frozen-in oxygen surface exchange reaction (“quenched condition”): the sample was equilibrated with typically low pO_2 (100 ppm O_2 or N_2) at high T (600-800 °C) and then quenched with cooling rate of 20 °Cmin⁻¹ to the desired temperature. This preserves the oxygen stoichiometry owing to the sluggish oxygen exchange surface reaction at low T and low pO_2 for 100 μm particles while the faster water uptake reaction (which does not require O=O double bond dissociation) still equilibrates. Then, proton uptake was measured by pH_2O changes at T of 200-500 °C.

The pH_2O was changed stepwise either by starting from an initial low pH_2O (typically 6.6 mbar) or from nominally dry condition and back again. The first approach allows for quicker measurements since steps from dry to humid condition are slow, but the latter has a higher sensitivity since a larger pH_2O range is covered. An example of the latter case is shown in Figure 3-7 for BL15F in N_2 at 250 °C. Each number in Figure 3-7 (a) refers to a certain pH_2O and the reversibility of the results has been checked by changing back to initial condition. In the regime of predominant hydration, $[OH'_O] \propto \sqrt{pH_2O}$ ideally holds as long as $[V_O^{\bullet\bullet}]$ is constant. Plotting the data points in Figure 3-7 (b) gives a straight line with an intercept close to zero. The fact that $[OH'_O] \propto \sqrt{pH_2O}$ is fulfilled indicates that for the experimentally observed moderate proton concentrations, proton-proton interaction is negligible. For some materials (e.g., BCFZr) a slight positive intercept occurs. This can be explained by formation of a thin oxide layer on the surface of the particles which tends to easily hydrate when changing from dry to wet condition for the first time and forms $Ba(OH)_2$ irreversibly. After correcting for this positive offset value, the proton concentrations are close to what was measured starting from 6.6 mbar H_2O . The effect of cracks formation and capillary condensation on the proton uptake is negligible in the covered T range [43]. How the weight changes can be related to proton concentration will be discussed later in 4.2.2. Proton concentration of the quenched BL15F for two different case of starting from nominally dry condition (green solid circles, 16.7 mbar H_2O) and starting from 6.6 mbar H_2O (green crosses, 15.7 mbar) is shown in Figure 3-7 (c) and the results are almost the same. The linearity of the corresponding van 't Hoff plot confirms once more that there is negligible proton-proton interaction in the covered proton concentration range.

In order to check for weight effects from surface water adsorption, TG control experiments of pH_2O steps are performed on $BaCO_3$ and $Ba(OH)_2$ powder which show no bulk water uptake, but are chemically closely related to Ba-rich cathode materials. For this,

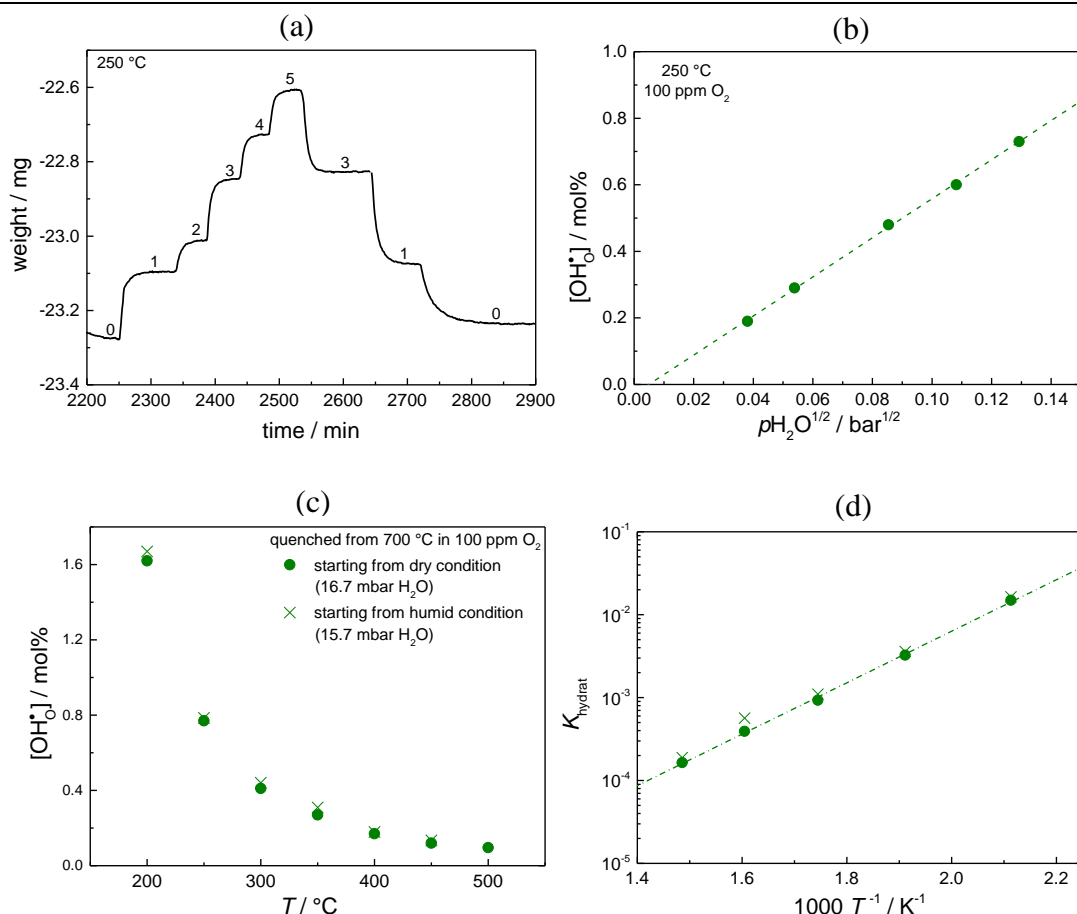


Figure 3-7: (a) Example of stepwise changing of $p_{\text{H}_2\text{O}}$ from nominally dry condition for BL15F at 250 °C in dry 100 ppm O_2 quenched from 700 °C (0: dry, 1: 1.45 mbar, 2: 2.9 mbar, 3: 7.3 mbar, 4: 11.7 mbar, 5: 16.7 mbar H_2O). The reversibility is also checked. (b) Proton concentration versus square root of water partial pressure at 250 °C. (c) T dependence of proton concentrations for the quenched BL15F. Solid green circles refer to measurements starting from nominally dry condition (16.7 mbar H_2O), green crosses refer to measurements starting from 6.6 mbar H_2O (15.7 mbar). (d) The corresponding van 't Hoff plot.

0.375 g of the BaCO_3 (BET surface area: 1.9 m^2/g) as well as 0.545 g $\text{Ba}(\text{OH})_2$ (BET surface area: 1.3 m^2/g) powder were equilibrated at 200-400 °C in humid N_2 and $p_{\text{H}_2\text{O}}$ was stepwise changed as in other humid experiments. The sample gained about 7-14 $\mu\text{g}/\text{m}^2$ depending on T . For a typical sample weight of 4 g (density about 5.7 gcm^{-3}) and 100 μm particle size, the total surface area would be 0.042 m^2 resulting in less than 1 μg weight gain due to water adsorption which is negligible compared to total weight gain of the sample in similar condition.

3.2.3.3 Mass spectroscopy

The exhaust gas is constantly monitored during the TG measurements using a quadrupole mass spectrometer (QMS 200 F1, balzers Prisma, Germany). MS shows the ion current of various molecules including water (I_{18}) and nitrogen (I_{28}). It is then possible to make a calibration plot of I_{18}/I_{28} as a function $p_{\text{H}_2\text{O}}$ (measured by the humidity sensor independently). Using the data from the different $p_{\text{H}_2\text{O}}$ applied in typical TG measurements, results are shown in Figure 3-8. Contributions from fragments I_{OH^-} and I_{H^+} are much lower

than I_{18} and can be neglected. Having the total flow of humidified N_2 (60 mlmin^{-1}), the flow of water molecules F_{H_2O} can be calculated. Integrating F_{H_2O} with respect to time then gives the number of H_2O molecules which are desorbed/adsorbed. An example is shown in Figure 3-9 in which BL5FZn20 is quenched in dry N_2 from $700 \text{ }^\circ\text{C}$ to $400 \text{ }^\circ\text{C}$; in minute 180, the sample is exposed to humidified N_2 ($7.3 \text{ mbar } H_2O$) and in min 320, T is increased to $600 \text{ }^\circ\text{C}$. The sample desorbs water which shows itself as a sharp peak in the I_{18} signal. When switching back to $400 \text{ }^\circ\text{C}$ in minute 360, the similar effect can be seen in reversed direction, but slower. The derivative of the TG (with negative sign) is in agreement with the change in I_{18}/I_{28} , but in a different scale. Finally, taking the integral of F_{H_2O} relative to the baseline results in $\sim 2 \text{ mg}$ of weight change when switching from $400 \text{ }^\circ\text{C}$ to $600 \text{ }^\circ\text{C}$ and back, which is consistent with the TG weight change.

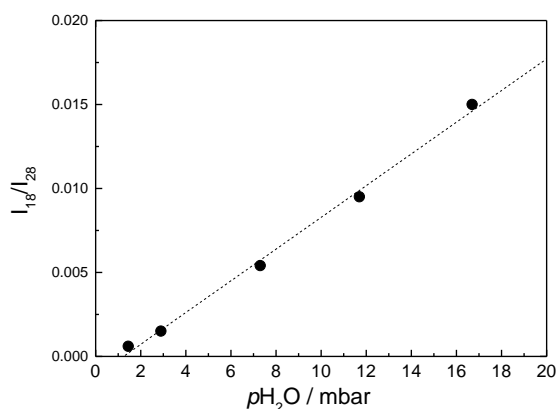


Figure 3-8: Calibration plot which correlates I_{18}/I_{28} to water partial pressure. The linear fit has a slope of 9.4×10^{-3} and an intercept of -0.00117 .

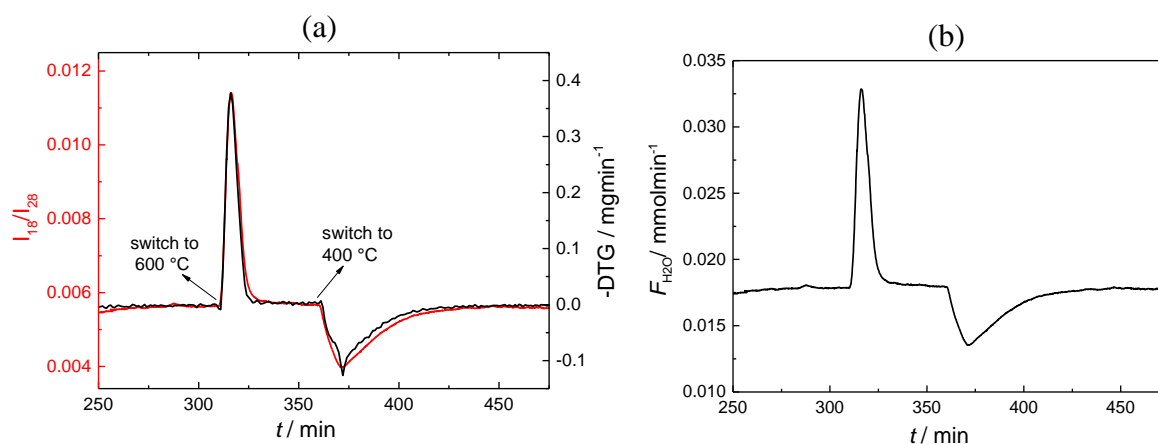


Figure 3-9: (a) I_{18}/I_{28} and the derivative of TG ($-DTG$) as a function of time recorded during T steps agree very well (inlet $p_{H_2O} = 7.3 \text{ mbar}$). (b) F_{H_2O} as a function of time: the area under the peaks (relative to the baseline) gives the number of desorbed/adsorbed water molecules.

3.2.4 Karl-Fischer titration

The proton concentration of hydrated samples can be measured independently by Karl-Fischer titration (831 KF-Coulometer, Metrohm, Germany) (KFT) which is a chemical ex-situ method [44]. Few hundred milligrams of $\text{BaCo}_{0.4}\text{Fe}_{0.4}\text{Zr}_{0.2}\text{O}_{3-\delta}$ particles were hydrated in humid N_2 and 100% O_2 (20 mlmin^{-1} , 20 mbar H_2O) at 250 °C and 500 °C for one and half a day and then moved to the cold zone of the hydration set up and quenched to room temperature while being flushed with 20 mlmin^{-1} dry N_2 . The sample was then inserted to the cold zone of the KFT setup and flushed with dry argon until a stable baseline was achieved. Then, it was moved to the hot zone (600 °C) and the released water in the Ar carrier gas flow was measured. The schematic of the hydration and KFT set up is illustrated in Figure 3-10. The results yield qualitatively the same trends as the TG analysis in section 4.2.3.3 (smaller proton concentration at higher T and more oxidizing conditions) and semi-quantitatively agree regarding the absolute $[\text{OH}'_0]$ percent range at 250 °C. However, issues in the quenching procedure and crack formation in the particles (probably leading to water surface adsorption during quenching resulting in too high $[\text{OH}'_0]$) cause the Karl-Fischer technique to overestimate the proton content.

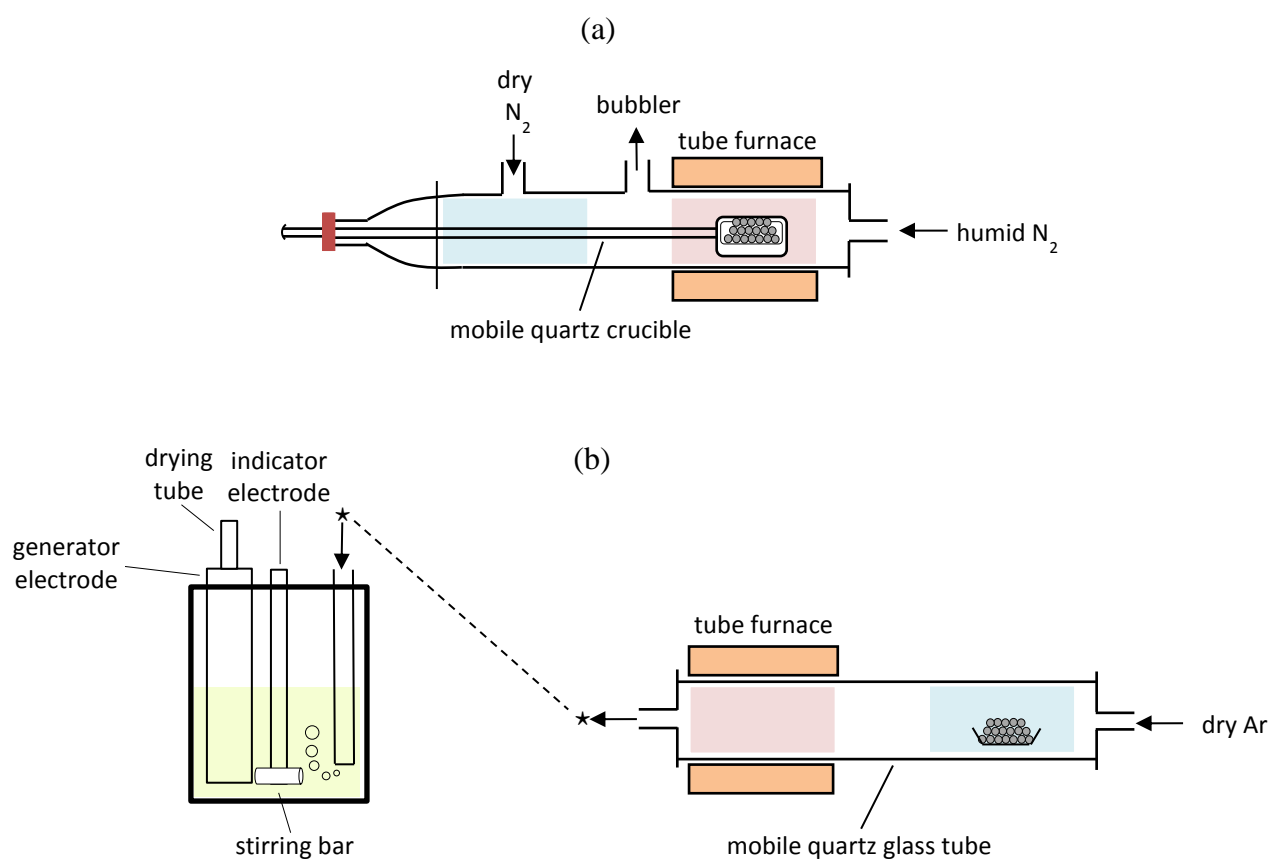


Figure 3-10: a) Hydration set up: The quartz sample holder can be moved inside the glass tube. After thermal treatment of the sample at elevated T in hot zone (red) of the setup, the sample holder is moved to the cold zone (blue) and quenched in dry N_2 . b) KFT set up: The sample is flushed with Ar in the cold zone (blue) first, and is moved to the hot zone (red) afterwards. The titration vessel setup then measures the released water.

3.2.5 Impedance measurement

An Alpha-A high resolution impedance analyzer (Novocontrol, Germany) was used to record the impedance spectra of samples in the frequency range of typically 1 MHz to 10 mHz at 20 mV amplitude.

Conductivity measurements on bulk electrolyte samples- The electronic transference number of electrolyte materials were studied by means of impedance spectroscopy in different atmospheres. The spark plasma sintered pellets of electrolytes were cut into squares of 0.5-0.7 mm thick (crystal preparation group, Max Planck Institute for Solid State Research) and ~ 400 nm of Pt was sputtered (Edwards auto 306, UK) on both surfaces as electrodes. For complete dehydration, the sample was then placed into a gold crucible and vacuum treated in a quartz tube at 800 °C for 4 h until the pressure dropped to 2×10^{-7} mbar (no protons, frozen-in oxygen vacancies).

The impedance spectra were measured in dry N₂ at temperatures up to 500 °C immediately without waiting for equilibration to measure oxygen vacancy conductivity. The measurement was then repeated in humidified oxidizing (N₂) and reducing condition (1.5 % H₂ in N₂) with 20 mbar H₂O up to 700 °C where protons and holes also contribute to the total conductivity. The total gas flow was always kept at 30 mlmin⁻¹ and pO_2 (1.5 % H₂ in N₂, 0.1 % O₂, 100 % O₂) and pH_2O (0.2, 2, 20 mbar H₂O) dependence of the conductivity was also studied at the same T .

Conductivity measurements on cathode materials- A direct measurement of the proton conductivity of cathode materials is challenging as $\sigma_{H^+} \leq \sigma_{\text{con}}$ due to the much higher mobility of electronic charger carriers compared to protonic defects; Pt was sputtered on conventionally sintered pellets of cathode materials BL5F, BSFZn, and BL5FZn20 and the conductivity measurements were performed by quenching the sample at its minimum conductivity (where both n-type and p-type electronic carriers are suppressed) as a function of pO_2 to lower T and then measuring conductivity upon changing pH_2O from dry to humid condition. It is important to check the reversibility (decrease of conductivity after switching back to dry condition) to distinguish proton conductivity from other effects such as re-oxidation of the sample by oxygen traces.

Another possibility is the use of proton selective layer of LWO; for this, 20 nm BZY15 and 200 nm LWO were deposited by PLD on a sintered pellet of BL5FZn20 from the polished side at 710 °C (slow heating/cooling rate) and 0.4 mbar pO_2 . If the holes are completely blocked, the impedance measurements can directly give the proton conductivity going from dry to humid condition and back again. However, due to presence of pinholes in LWO layer, the electronic carrier might not be completely blocked. Therefore, an impedance measurement of the quenched sample from a higher temperature and at the minimum conductivity, as described above, is also helpful.

The oxygen vacancy conductivity of BL5FZn20 can be measured after quenching the sample from 600 °C in dilute hydrogen at its minimum conductivity and then measuring the impedance spectra at different temperatures.

Since the electronic resistance of the cathode materials is expected to be in the range of lead and contact resistance, a pseudo four-point-probe (current and voltage line meeting at the Pt foil electrode which is pressed against the sputtered Pt film) is applied on Pt sputtered sintered pellets of cathode materials. This ensures that the lead and contact resistances are eliminated. The experiment was performed at different pO_2 and T range of 0.1-100% O_2 and 25-600 °C. The samples were used in the shape of bars (~ 1 cm long, $\sim 3 \times 3$ mm² thick) contacted at the small faces to prevent the resistances from becoming unpractically low.

3.2.6 Microelectrode measurement

Microelectrode measurements were performed to study the surface oxygen reduction reaction at cathode materials on proton conducting electrolytes. The potential electronic leakage in gas symmetric cells at high pO_2 has to be considered when electrolyte materials with non-zero electronic transference number are used (see 3.3 for more detail). The microelectrode structured sample (see 3.1.4) was placed in a vacuum tight chamber at certain T , pO_2 , and pH_2O and a fresh Pt/20%Ir needle with tip radius of nominally 2.5 μm (Moser Jewel, USA) was connected to the working electrode (WE, cathode). The counter electrode (silver) was also connected to a used Pt/Ir needle. The impedance spectra were then measured with an Alpha-A high resolution impedance analyzer (Novocontrol, Germany) in the frequency range of typically 1 MHz to 1 mHz at 20 mV amplitude in the following procedure:

- T dependence (400-750 °C in 50 K steps, measurement in both heating and cooling direction), 1000 ppm O_2 , 20 mbar H_2O , 100 μm (the thermovoltage is typically 50 K in the covered T range).
- pO_2 dependence (100 ppm to 100 % O_2), 600/650 °C, 20 mbar H_2O , 100 μm .
- pH_2O dependence (dry to 20 mbar H_2O), 600/650 °C, 1000 ppm O_2 , 100 μm .
- Diameter (d) dependence (40-100 μm), 600/650 °C, 1000 ppm O_2 , 20 mbar H_2O .

The oxygen and water partial pressure are cross-checked with an oxygen analyzer Rapid 2100 (cambridge sensotec, UK) and humidity sensor Hygroclip (rotronic, Germany) and the total flow is always kept constant (150 mlmin⁻¹). The schematic of the microelectrode set up is shown in Figure 3-11.

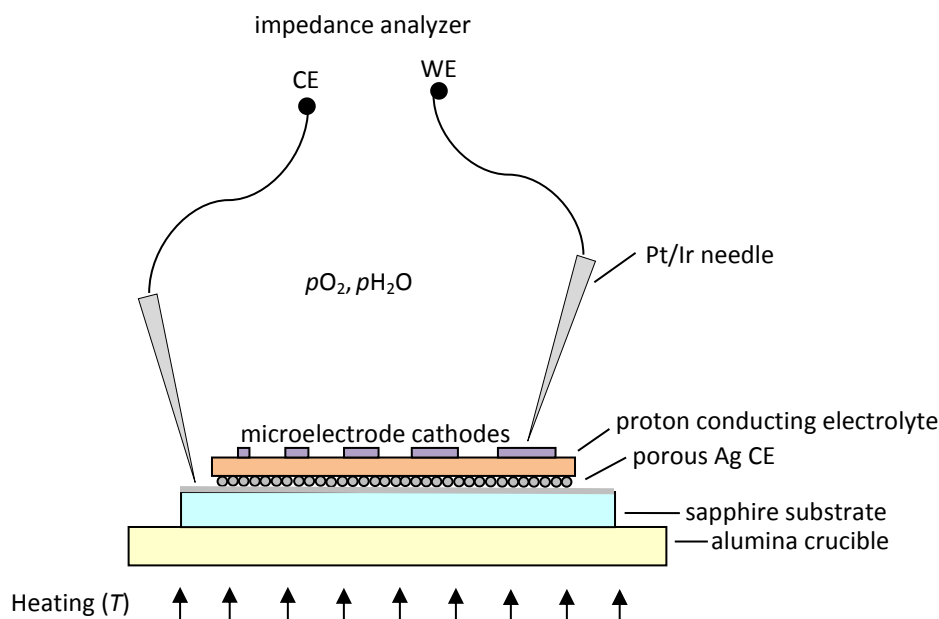


Figure 3-11: The schematic of the microelectrode set up: The sample is placed on an Alumina crucible which is heated from below and is in a gas tight chamber in certain pO_2 and pH_2O .

3.3 Alternative electrolytes for surface oxygen exchange kinetics study of cathodes

The electronic transference number of the typical electrolyte materials in a gas symmetric setup at high pO_2 ($t_{eon} \approx 0.1-0.2$) makes precise determination of the surface reaction resistance sophisticated (see [45]). Although this is not troublesome in a real fuel cell (as t_{eon} approaches zero at the anode due to decrease of oxygen chemical potential across the electrolyte), it is crucial to decrease the electronic leakage in the gas symmetric setup as an important experimental tool in many studies. While this becomes more important for dense cathodes, where the small surface area leads to large oxygen surface reaction resistance (R_s), it is also not necessarily negligible for porous ones with large surface area. Figure 3-12 (a) shows the equivalent circuit of the electrochemical cell considering the electronic leakage. When R_{eon} is small compared to R_s , the low frequency semicircle would not represent the surface reaction resistance anymore. As Figure 3-12 (b) shows, the ratio of apparent surface resistance (observed in the measurement) to real one (R'_s / R_s) does not solely depend on t_{eon} but on $r = R_{eon} / R_s$ as well according to

$$\frac{R'_s}{R_s} = \frac{R_{eon}^2}{(R_{ion} + R_{eon} + R_s)(R_{ion} + R_{eon})} = \frac{r(1-t_{eon})^2}{(1+r-t_{eon})} \quad (3.1)$$

So far, several methods have been applied to tackle this problem including use of electrolyte with lower acceptor dopant [45], applying cathodic DC bias to decrease μ_O at the anode and

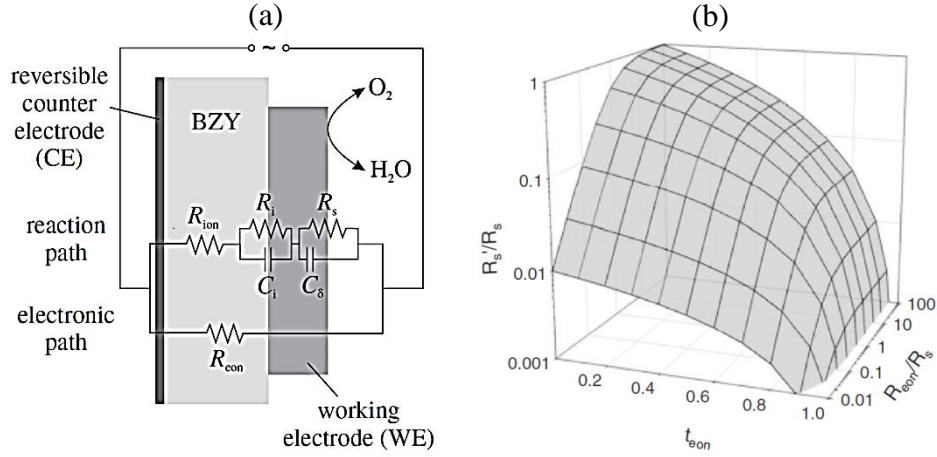


Figure 3-12: (a) Electrochemical cell for investigating oxygen kinetics on proton-conducting oxides and its equivalent circuit [45]. (b) Ratio of apparent to true surface reaction resistance (R'_s/R_s) versus t_{eon} and R_{eon}/R_s [46].

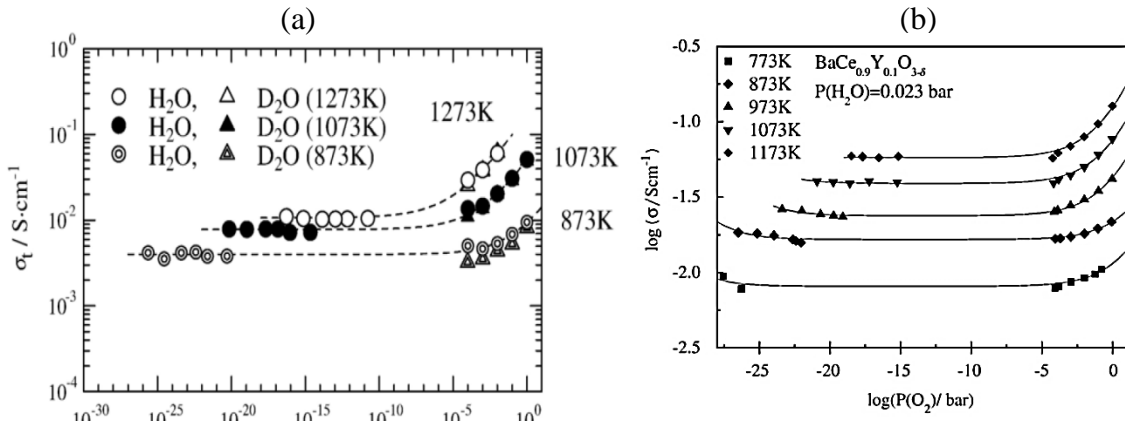
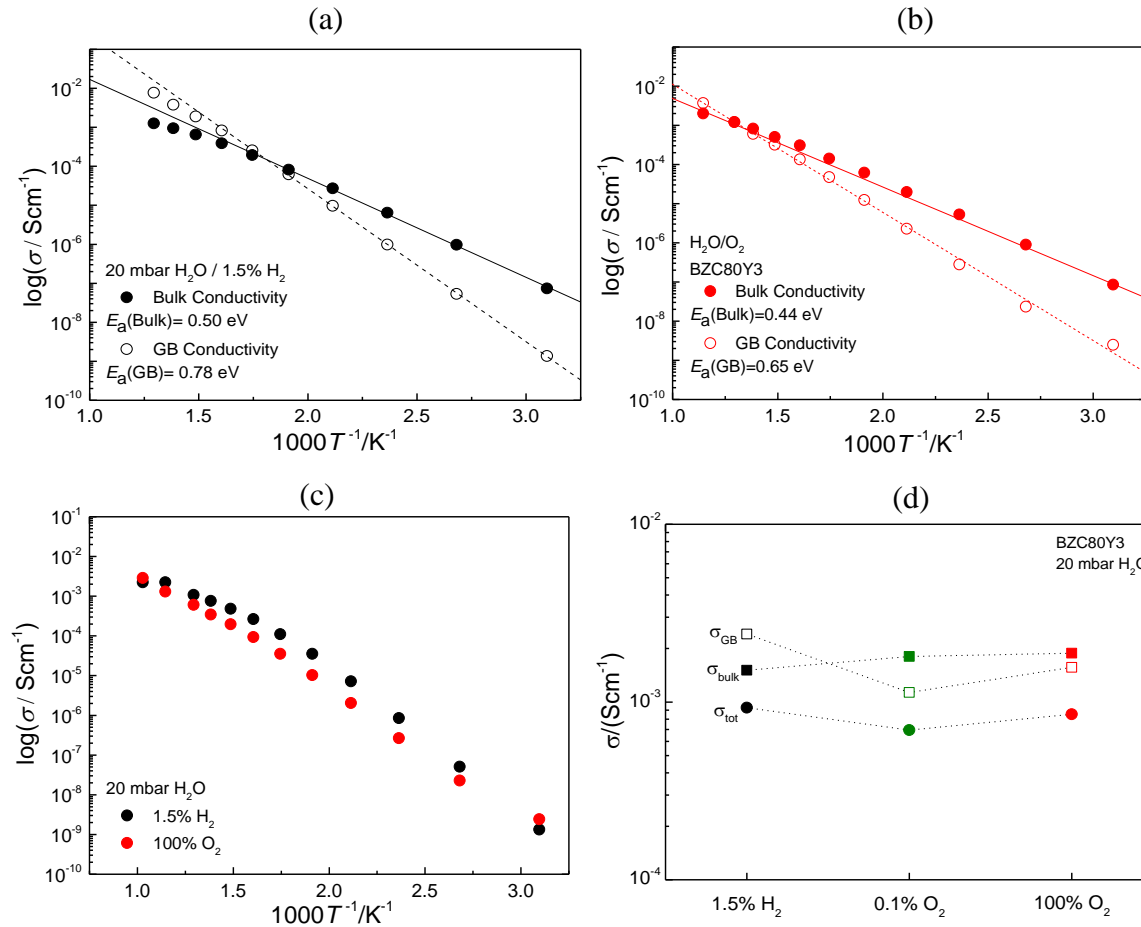
use of proton selective double layer (molten KOH) [24], but all come with some practical drawbacks. The following electrolytes have been selected for further investigations: LWO, BZC80Y3, BZC80Y1.2, BZC50Y3, BZC20Y1, and BZC10Y1. Conductivity measurements on bulk samples were performed to quantify the electronic transference number in these materials in the relevant experimental conditions, and LWO and BZC10Y1 were selected for further investigations with microelectrode measurements (3.2.6).

It has been shown in the literature that Ce can moderately increase the total proton conductivity σ_{tot} of $\text{Ba}(\text{Zr},\text{Y})\text{O}_{3-\delta}$ (by improving GB conductivity and higher dehydration temperature) while it suppresses the hole transference number given by

$$t_{\text{eon}} = \frac{i_{\text{eon}}}{i_{\text{tot}}} = \frac{\sigma_{\text{eon}}}{\sigma_{\text{ion}} + \sigma_{\text{eon}}} \quad (3.2)$$

The Brouwer diagram for $\text{Ba}(\text{Zr}_{0.8}\text{Y}_{0.2})\text{O}_{3-\delta}$ and $\text{Ba}(\text{Ce}_{0.9}\text{Y}_{0.1})\text{O}_{3-\delta}$ is shown in Figure 3-13. At 1073 K and $p\text{O}_2 = 1$ bar, $t_{\text{eon}} \approx 0.85$ for BZY20 ($\sigma_{\text{tot}}|_{p\text{O}_2=10^{-15}\text{bar}} \approx \sigma_{\text{ion}} \approx 8 \times 10^{-3} \text{ Scm}^{-1}$, $\sigma_{\text{eon}}|_{p\text{O}_2=1\text{bar}} \approx \sigma_{\text{tot}}|_{p\text{O}_2=1\text{bar}} - \sigma_{\text{ion}} \approx 5.2 \times 10^{-2} \text{ Scm}^{-1}$) while for BCY10, t_{eon} decreases to ≈ 0.50 ($\sigma_{\text{tot}}|_{p\text{O}_2=10^{-15}\text{bar}} \approx \sigma_{\text{ion}} \approx 4 \times 10^{-2} \text{ Scm}^{-1}$, $\sigma_{\text{eon}}|_{p\text{O}_2=1\text{bar}} \approx \sigma_{\text{tot}}|_{p\text{O}_2=1\text{bar}} - \sigma_{\text{ion}} \approx 4 \times 10^{-2} \text{ Scm}^{-1}$) due to presence of Ce.

The conductivity measurements performed on BZCY series is exemplified for BZC80Y3 in Figure 3-14. The blocking nature of the grain boundaries (GB) for these perovskites shows itself as a medium frequency semicircle in impedance spectroscopy and therefore unlike LWO, GBs contribute to the total conductivity with a higher activation energy than bulk conductivity (in humid 100% O_2 , E_a is 0.65 eV for grain boundaries and 0.44 eV for bulk in BZC80Y3 according to Figure 3-14 (b)). Comparison of the total conductivity in different T and $p\text{O}_2$ shows that the total conductivity only slightly increases as the environment becomes

Figure 3-13: Brouwer diagram for (a) $\text{Ba}(\text{Zr}_{0.8}\text{Y}_{0.2})\text{O}_{3-\delta}$ [47]. (b) $\text{Ba}(\text{Ce}_{0.9}\text{Y}_{0.1})\text{O}_{3-\delta}$ [48].Figure 3-14: a) T dependence of GB and bulk conductivity in humid 1.5% H_2 . b) T dependence of GB and bulk conductivity in humid 100% O_2 . c) T dependence of total conductivity in humid 100% O_2 and 1.5% H_2 . d) $p\text{O}_2$ dependence of bulk, GB and total conductivity at 600 °C.

more oxidizing. This means although hole transference number is still non-zero, it is quite smaller for this series compared to BZY compounds according to the measurements. For example in BZC80Y1.2, $\sigma_{\text{eon}}|_{p\text{O}_2=1\text{bar}} \approx \sigma_{\text{tot}}|_{p\text{O}_2=1\text{bar}} - \sigma_{\text{tot}}|_{p\text{O}_2=1\text{mbar}} = 0.5 \times 10^{-4} \text{ Scm}^{-1}$ (since at high $p\text{O}_2$ the conductivity is mainly electronic and at low $p\text{O}_2$, mainly ionic); ideally, $\sigma_{\text{eon}} \propto p\text{O}_2^{1/4}$ and therefore, $\sigma_{\text{eon}} = 8.9 \times 10^{-6} \text{ Scm}^{-1}$ in 0.1% O_2 . Since $\sigma_{\text{tot}} = \sigma_{\text{ion}} + \sigma_{\text{eon}} = 1.72 \times 10^{-4} \text{ Scm}^{-1}$ in

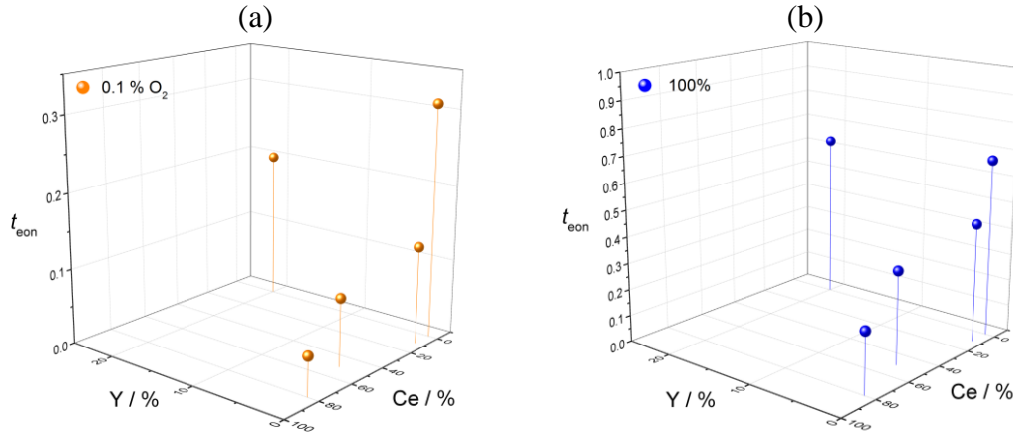


Figure 3-15: electronic transference number as a function of Y and Ce content at 600 °C in (a) 0.1% O₂. (b) 100% O₂.

0.1% O₂, $\sigma_{\text{ion}} = 1.63 \times 10^{-4} \text{ Scm}^{-1}$. This results in $t_{\text{eon}} = 0.23$ in 100% and $t_{\text{eon}} = 0.05$ in 0.1% O₂.

Figure 3-15 shows how t_{eon} changes for a number of materials as a function of Ce and Y content. One can see that the Ce content drastically changes the electronic transference number while Y has negligible effect. However, according to eq. (3.1) t_{eon} is not the only decisive parameter, but r is also important.

In Figure 3-16, R'_s / R_s as a function of t_{eon} and $r = R_{\text{con}} / R_s$ is shown for BZC80Y1.2, BZC10Y1, BZC50Y3 and BZY1 (as electrolyte) on BSCF and BSFZn (as cathode). This has been done in 0.1% and 100% O₂ at 600 °C for a 100 μm microelectrode. For BSCF on BZY1, R_s values of $\sim 30 \text{ M}\Omega$ (1mbar O₂) and $\sim 1.5 \text{ M}\Omega$ (1 bar O₂) were reported in 20 mbar H₂O, at 550 °C and 80 μm after correction for the electronic leakage [24]. Assuming an activation energy of 1.5 eV and an ideal diameter dependence of R_s for active bulk path, R_s values of $\sim 6 \text{ M}\Omega$ (1 mbar O₂) and $\sim 300 \text{ k}\Omega$ (1 bar O₂) can be estimated for a 100 μm microelectrode at 600 °C. For 100 μm BSFZn microelectrode at 600 °C, effective oxygen reduction rate constant k_o^q of $1.3 \times 10^{-9} \text{ cms}^{-1}$ (1 mbar O₂) and $2.5 \times 10^{-8} \text{ cms}^{-1}$ (1 bar O₂) were reported [24].

The area specific resistance ASR_s can be calculated according to

$$ASR_s = \frac{RT}{4F^2 k_o^q c_o} \quad (3.3)$$

where R is the gas constant, F is the Faraday constant and $c_o \approx 0.08 \text{ molcm}^{-3}$. This would result in R_s values of $\sim 24 \text{ M}\Omega$ (1 mbar O₂) and $\sim 1.2 \text{ M}\Omega$ (1 bar O₂) for BSFZn. R'_s / R_s is in general smaller for BSFZn than BSCF which emphasizes that the electronic leakage is more troublesome for slower cathode materials (larger R_s). Although t_{eon} is larger for BZC10Y1 than BZC50Y3, R'_s / R_s is smaller for the latter.

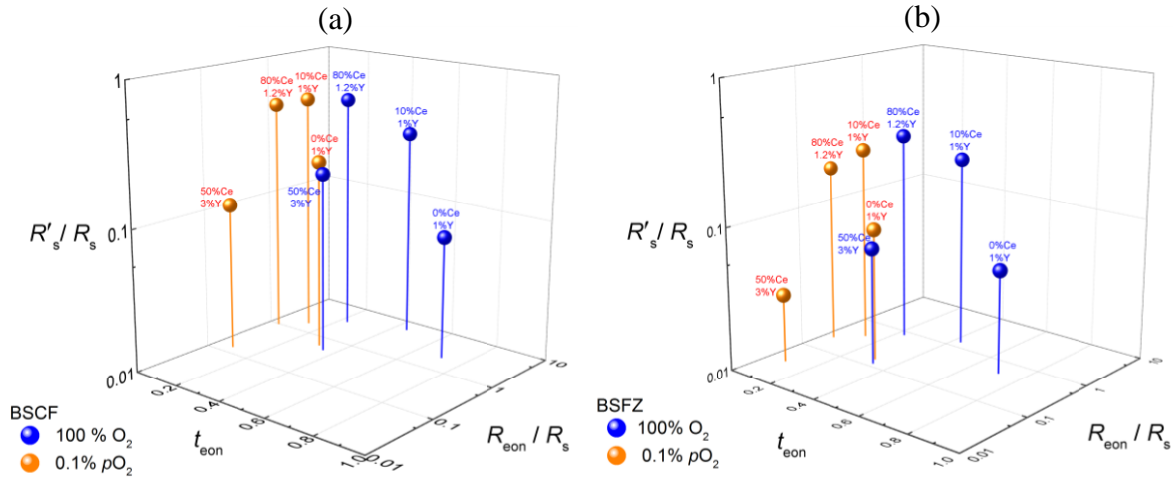


Figure 3-16: R'_s/R_s as a function of t_{eon} and R_{eon}/R_s in 0.1% and 100% O₂ for BZC80Y1.2, BZC10Y1, BZC50Y3 and BZY1 for (a) BSCF (b) BSFZn 100 μ m microelectrodes (with nominal thickness of 100 nm) at 600 $^{\circ}$ C.

Practically, it is difficult to sinter dense pellets for samples with high Ce content using SPS. Although, Ce decreases the sintering T , but as it easily reduces in the SPS process and creates pores in the sample, the resulting samples are mechanically less stable. The use of YSZ felts as buffer layer might be helpful in this case; however, it was not applied in this work. The comparison of the unit cell volume compared to theory shown in Figure 3-3 shows a good agreement indicating that the samples are dense enough. Eventually, BC10Y1 is chosen for further investigation since R'_s/R_s is sufficiently high, the lower Ce content makes the sintering process more feasible, and samples with lower Ce content have better long term stability in CO₂.

For correction of apparent surface reduction resistance R'_s , the following procedure is taken. Impedance measurements performed on bulk BZC10Y1 give σ_{tot} at different pO₂s (see Table 3-4). Assuming mainly contribution of the ionic conductivity at lowest pO₂ of 0.01% as the starting point, σ_{eon} in 100% O₂ is obtained having σ_{tot} . Ideally, $\sigma_{eon} \propto pO_2^{1/4}$ and this gives σ_{eon} in 0.01% O₂ and the new corrected value for σ_{ion} ($3.6 \times 10^{-5} \text{ Scm}^{-1}$). Then, σ_{eon} is calculated having σ_{tot} at different pO₂s. Knowing the electronic resistance in 0.1% O₂ and 20 mbar H₂O and assuming the limiting case of $R_{eon} \propto pH_2O^{0.5}$ (expected to hold for $[OH'_o] \approx \text{const.}$), the electronic conductivity in different pH₂O is also listed in Table 3-5. This has been done also for the case of $R_{eon} \propto pH_2O^{0.25}$ (regime with $[OH'_o]$ being slightly dependent on pH₂O). R_{eon} for 100 μ m microelectrode is finally calculated according to [45]

$$R_{eon} = (2d\sigma_{eon})^{-1} \quad (3.4)$$

These values are kept fixed in the equivalent circuit of Figure 3-12 (a) and the spectra are then fitted (see section 4.3).

Table 3-4: pO_2 dependence of total conductivity (σ_{tot}), electronic conductivity (σ_{eon}), electronic transference number (t_{eon}) and the electronic resistance (R_{eon}) for a 100 μm dense microelectrode on BZC10Y1 electrolyte. ($\sigma_{ion} = 3.6 \times 10^{-5} \text{ Scm}^{-1}$ and $pH_2O = 20 \text{ mbar}$)

pO_2	$\sigma_{tot} / \text{Scm}^{-1}$	$\sigma_{eon} / \text{Scm}^{-1}$	t_{eon}	$R_{eon} (100 \mu\text{m}) / \text{M}\Omega$
0.01 %	3.90×10^{-5}	2.9×10^{-6}	7%	17
0.1%	3.97×10^{-5}	5.1×10^{-6}	12%	10
1%	4.43×10^{-5}	9.1×10^{-6}	20%	5.5
10%	-	1.6×10^{-5}	31%	3.1
100%	6.8×10^{-5}	2.9×10^{-5}	45%	1.7

Table 3-5: pH_2O dependence of electronic conductivity (σ_{eon}) and the electronic resistance (R_{eon}) for a 100 μm dense microelectrode on BZC10Y1 electrolyte assuming (1) $R_{eon} \propto pH_2O^{0.5}$ and (2) $R_{eon} \propto pH_2O^{0.25}$.

pH_2O / mbar	(1) $\sigma_{eon} / \text{Scm}^{-1}$	(1) $R_{eon} (100 \mu\text{m}) / \text{M}\Omega$	(2) $R_{eon} (100 \mu\text{m}) / \text{M}\Omega$
20	5.1×10^{-6}	10	10
16.7	5.6×10^{-6}	9	9.6
5	1.0×10^{-5}	5	7
1.2	2.1×10^{-5}	2.4	4.9
1	2.9×10^{-5}	2.2	4.7

LWO, with a fluorite related structure [49], is an almost pure ion conductor up to 800 °C in oxidizing conditions [50]. The conductivity of a 0.5 mm thick LWO sample in different conditions is measured and shown in Figure 3-17. The grain boundaries are not blocking for LWO cells according to impedance measurements. The similar conductivity in humid oxidizing and reducing condition in different T and pH_2O confirms that t_{eon} is negligible for LWO in the covered T range, in contrast to $\text{Ba}(\text{Zr,Ce,Y})\text{O}_{3-\delta}$. This makes LWO a promising candidate as electrolyte in gas symmetric cells. However, LWO reacts with Ba-rich cathode materials and a thin layer of BZY buffer layer is needed to prevent the reaction (see 3.1.4).

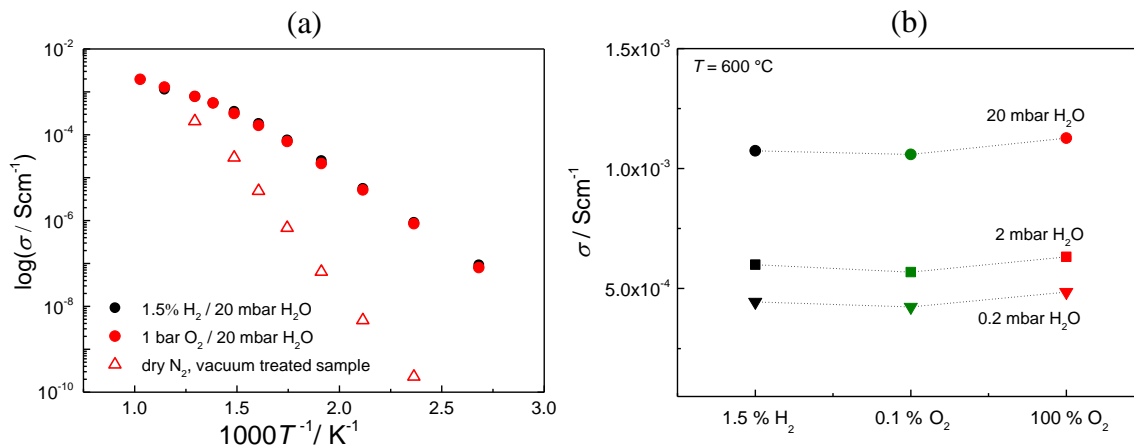


Figure 3-17: (a) The total conductivity of 0.5 mm thick LWO for vacuum treated sample (oxygen vacancies conductivity), and in humid 1.5% H_2 (proton conductivity) and 100% O_2 (proton and hole conductivity). (b) The change of total conductivity with pO_2 and pH_2O at 600 °C.

Chapter 4

Results and Discussion

4 Results and discussion

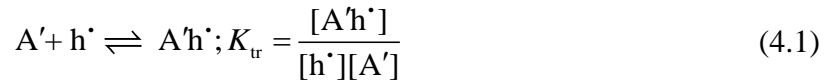
4.1 Two-fold stoichiometry relaxation in electrolyte perovskites

The stoichiometry relaxation of triple-conducting oxides (containing oxygen vacancies, protons and holes as defects) upon $p\text{H}_2\text{O}$, $p\text{O}_2$, and T change is simulated and discussed in this section (see [51] for more detail). The procedure explained in more detail in chapter 2 is extended to investigate the temperature dependence and to consider trapping of holes. Oxygenation and hydration mass action constants as well as $D_{\text{V}_\text{O}^\bullet}$, $D_{\text{OH}_\text{O}^\bullet}$, D_{h^\bullet} are chosen to represent typical proton-conducting electrolytes such as acceptor-doped BaZrO_3 and BaCeO_3 .

4.1.1 Details of the simulations

The computational details of the one-dimensional finite difference simulations for a finite sample with a thickness of 0.001 cm with diffusion occurring from both surfaces are given in ref. [25]. The key points of the model are (i) assumption that all surface exchange reactions are comparatively fast, (ii) ideally dilute behavior of the point defects, (iii) local electroneutrality (i.e., the stoichiometry relaxation is purely determined by bulk transport, no interfacial space charge effects), and (iv) application of small $p\text{H}_2\text{O}$ changes. The simulation input parameters are the defect diffusivities and the defect concentrations as well as their change for a 10% increase of $p\text{H}_2\text{O}$ at given $p\text{O}_2$ and T . These concentrations are calculated from the oxygenation and hydration mass action constants and an acceptor concentration of 10% assuming ideally dilute behavior (absence of defect interactions, which also implies that the defect diffusivities depend only on T).

The effect of defect trapping is included assuming the following reaction



where $\text{A}'\text{h}^\bullet$ refers to the trapped holes and $[\text{A}'] = [\text{A}'_{\text{tot}}] - [\text{A}'\text{h}^\bullet]$ with total acceptor dopant concentration $[\text{A}'_{\text{tot}}]$ of typically 0.1. The electroneutrality can then be written as

$$[\text{A}'] = 2[\text{V}_\text{O}^{\bullet\bullet}] + [\text{h}^\bullet] + [\text{OH}_\text{O}^\bullet] \quad (4.2)$$

The defect concentrations are then calculated with these equations together with $3 = [\text{O}_\text{O}^\times] + [\text{OH}_\text{O}^\bullet] + [\text{V}_\text{O}^{\bullet\bullet}]$ assuming two cases of weak ($\Delta H_{\text{tr}}^\circ = -0.3 \text{ eV}$ and $\Delta S_{\text{tr}}^\circ = 0$) and strong ($\Delta H_{\text{tr}}^\circ = -0.6 \text{ eV}$ and $\Delta S_{\text{tr}}^\circ = 0$) trapping. In the stoichiometry relaxation simulation, free holes are transferred between the simulation cells according to their concentration difference and mobility. Then the trapping equilibrium (4.1) is updated in the cells (i.e. in case of strong

trapping most of the transferred free holes will become trapped), and finally the next carrier transfers are calculated from the defect mobilities and the new concentration differences.

The parameters for proton diffusivity D_{OH° and K_{hydrat} were chosen close to the values given for $\text{BaZr}_{0.9}\text{Y}_{0.1}\text{O}_{2.95}$ in [2] with a proton migration enthalpy of 0.4 eV and $\Delta H_{\text{hydrat}}^\circ$ -0.8eV. The vacancy diffusivity $D_{\text{V}_\circ^{\bullet\bullet}}$ is taken a bit lower than the values derived in [52] for $\text{BaZr}_{0.9}\text{Y}_{0.1}\text{O}_{2.95}$ to obtain better agreement with $D_{\text{H}_2\text{O}}^\delta$ from [53], and a $\text{V}_\circ^{\bullet\bullet}$ migration energy of 0.8 eV typical for many perovskites is used. The hole diffusivity is assumed T -independent (cf. the even slight decrease of hole mobility with increasing T for acceptor-doped SrTiO_3 , BaTiO_3), with a value $D_{\text{h}^\bullet} = 8.6 \times 10^{-3} \text{ cm}^2/\text{s}$ in the typical range for acceptor-doped SrTiO_3 or BaTiO_3 [54]–[56]. At all T considered, $D_{\text{h}^\bullet} > D_{\text{OH}^\circ} > D_{\text{V}_\circ^{\bullet\bullet}}$. For K_{ox} , ab initio calculations [57] for acceptor-doped BaZrO_3 yielded values of $\Delta H_{\text{ox}}^\circ$ in the range of +0.88 to +1.53 eV strongly depending on the chosen exchange correlation functional (for the PBE functional which is known to strongly underestimate the band gap, even $\Delta H_{\text{ox}}^\circ = -1.31$ eV is obtained). Taking a value of $\Delta H_{\text{ox}}^\circ = 0.9$ eV proved suitable to reproduce the experimentally observed change from protonic to hole electronic conductivity at high T and $p\text{O}_2$ and the T -dependence of the conductivity in the hole-dominated regime [47], [58]. However, the values of $\Delta H_{\text{ox}}^\circ$ and the temperature dependence of D_{h^\bullet} are strongly correlated (a non-negligible hole migration barrier will directly lead to less positive $\Delta H_{\text{ox}}^\circ$). While the chosen parameters are in a range typical for acceptor-doped $\text{Ba}(\text{Zr,Ce})\text{O}_{3-\delta}$ perovskite proton conductors, it is not attempted to achieve the best possible fit for an individual member of this materials family.

The effective diffusivities $D_{\text{H}}^{\text{eff}}$ and $D_{\text{O}}^{\text{eff}}$ were calculated from the linear initial regions of the normalized integral defect concentration versus \sqrt{t} according to $D = (\text{slope})^2 \pi l^2 / 16$ (l is the sample thickness). The transient behavior of the total conductivity for conditions of non-monotonic relaxation was fitted by a sum of two individual diffusion-limited relaxation curves as suggested in [34], yielding D_{fast} and D_{slow} . The chemical diffusion coefficients D_{H}^δ , D_{O}^δ , and $D_{\text{H}_2\text{O}}^\delta$ (strictly valid only in situations without perceptible contribution from a third carrier) are calculated using the transference numbers of the full three carrier defect model from

$$D_{\text{H}}^\delta = \frac{t_{\text{h}^\bullet}}{t_{\text{h}^\bullet} + t_{\text{OH}^\circ}} D_{\text{OH}^\circ} + \frac{t_{\text{OH}^\circ}}{t_{\text{h}^\bullet} + t_{\text{OH}^\circ}} D_{\text{h}^\bullet} \quad (4.3)$$

$$D_{\text{O}}^\delta = \frac{t_{\text{h}^\bullet}}{t_{\text{h}^\bullet} + t_{\text{V}_\circ^{\bullet\bullet}}} D_{\text{V}_\circ^{\bullet\bullet}} + \frac{t_{\text{V}_\circ^{\bullet\bullet}}}{t_{\text{V}_\circ^{\bullet\bullet}} + t_{\text{h}^\bullet}} D_{\text{h}^\bullet} \quad (4.4)$$

$$D_{\text{H}_2\text{O}}^\delta = \frac{t_{\text{OH}_0^\bullet}}{t_{\text{OH}_0^\bullet} + t_{\text{V}_0^{\bullet\bullet}}} D_{\text{V}_0^{\bullet\bullet}} + \frac{t_{\text{V}_0^{\bullet\bullet}}}{t_{\text{OH}_0^\bullet} + t_{\text{V}_0^{\bullet\bullet}}} D_{\text{OH}_0^\bullet} \quad (4.5)$$

in absence of hole trapping. These expressions deviate from the respective two carrier equations (e.g., $D_{\text{H}}^\delta = t_{\text{h}^\bullet} D_{\text{OH}_0^\bullet} + t_{\text{OH}_0^\bullet} D_{\text{h}^\bullet}$) by the fact that the t_i are divided by $(t_i + t_j)$. This corresponds to hypothetically setting the mobility of the respective third carrier to zero.

4.1.2 Results and discussion

In this section, first the temperature dependence of stoichiometry relaxation in a three carrier system is analyzed in absence of hole trapping. Trapping effects are then discussed in figure 4-5 and 4-6. The oxygenation and hydration mass action constants, defect diffusivities, defect concentrations and their respective conductivities are shown in Figure 4-1. The results show that even at elevated T up to 1400 K, a perceptible proton concentration is present which is in agreement with literature data on acceptor-doped BaZrO₃ and BaCeO₃ [2]. The material is predominantly an ionic conductor at low $p\text{O}_2$; however the electronic (hole) conductivity dominates the total conductivity at higher $p\text{O}_2$. The increased number of mobile holes can lead to transition from single-fold water chemical diffusion for low $[\text{h}^\bullet]$ to two-fold relaxation at high $[\text{h}^\bullet]$ as is apparent in Figure 4-2.

Figure 4-2 plots the time evolution of defect concentrations and of total conductivity in different $p\text{O}_2$ at constant T and $K_{\text{hydrat}} p\text{H}_2\text{O}$ referring to different h^\bullet concentration. The initial slopes (indicated by straight solid lines) of the concentration plots yield the effective diffusivities $D_{\text{H}}^{\text{eff}}, D_{\text{O}}^{\text{eff}}$. The conductivity curves are fitted by the sum of two contributions (dashed lines) yielding $D_{\text{fast}}, D_{\text{slow}}$.

For lowest $K_{\text{OX}} \sqrt{p\text{O}_2}$, where the hole concentration is small, the relaxation of the ionic species are determined by $D_{\text{H}_2\text{O}}^\delta$ (single-fold relaxation). The splitting of $\text{V}_0^{\bullet\bullet}$ and OH_0^\bullet concentration becomes more visible for $K_{\text{OX}} \sqrt{p\text{O}_2} = 3 \times 10^{-5}$ and more pronounced for $K_{\text{OX}} \sqrt{p\text{O}_2} = 3 \times 10^{-4}$. In this case, the material is still in the predominant hydration regime and the contribution of hydrogenation reaction to the relaxation kinetics is small. However, for high $K_{\text{OX}} \sqrt{p\text{O}_2}$ (high K_{OX} as in redox-active cathode perovskites or extremely high $p\text{O}_2$ for electrolytes), hydrogenation would perceptibly contribute to the proton incorporation. An initial fast proton uptake (hydrogenation, change in $[\text{OH}_0^\bullet]$ and $[\text{h}^\bullet]$) followed by a slower proton uptake (hydration, change in $[\text{OH}_0^\bullet]$ and mainly $[\text{V}_0^{\bullet\bullet}]$) can be observed. $\text{V}_0^{\bullet\bullet}$ and OH_0^\bullet concentration then approach $D_{\text{V}_0^{\bullet\bullet}}$ (the slower species in the oxygenation reaction) and $D_{\text{OH}_0^\bullet}$

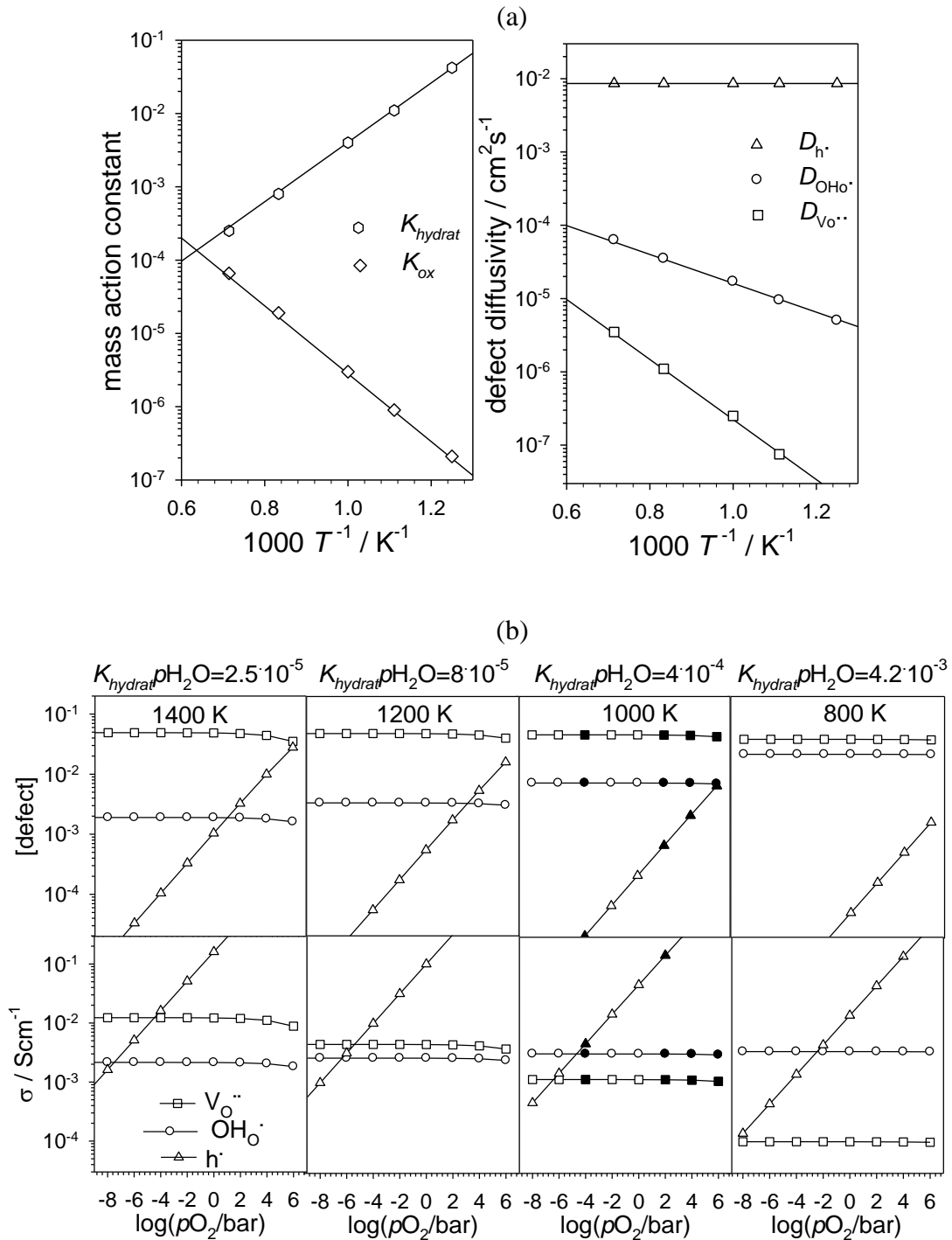


Figure 4-1: (a) Mass action constants and defect diffusivities, (b) defect concentrations and partial conductivities for the conditions investigated (intermediate degree of hydration). Solid symbols in (b) refer to the conditions used for Figure 4-2.

(the slower specie in hydrogenation reaction) curve for a short time and will approach $D_{H_2O}^{\delta}$ for longer times where hydration is predominant.

When the total conductivity is predominantly electronic or contains at least a significant contribution from holes, the two-fold non-monotonic relaxation is observed already for the lowest pO_2 with a minimum followed by an increase to a final value only slightly below the

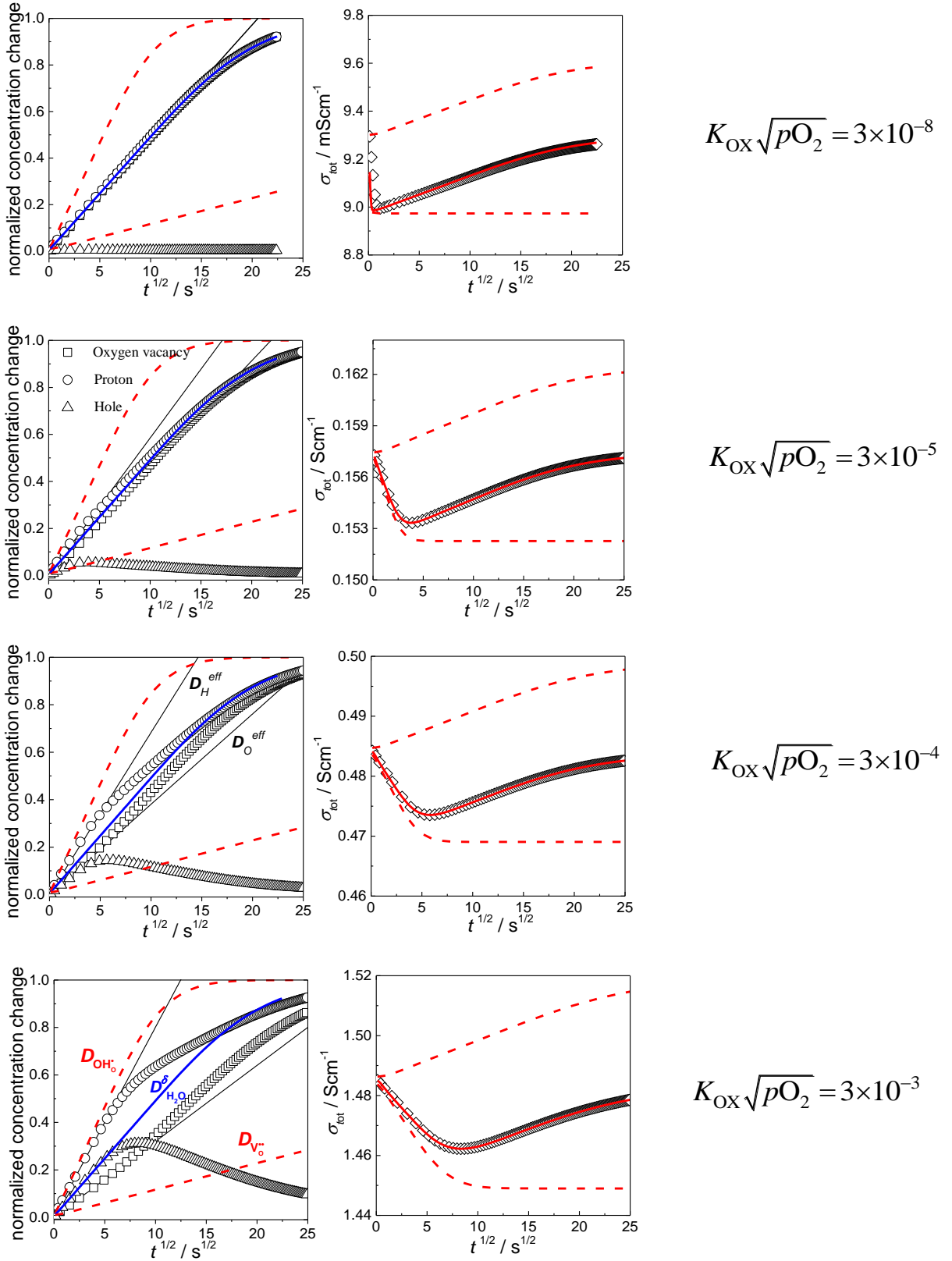


Figure 4-2: Simulated time evolution of integrated normalized defect concentration changes after a 10% increase in $p\text{H}_2\text{O}$ (left column; the dashed lines correspond to diffusivities equal to $D_{\text{OH}_2^+}$, $D_{\text{V}_o^{2+}}$, solid blue line: $D_{\text{H}_3\text{O}^+}^{\delta}$) and of total conductivity changes (right column) for low, intermediate and high $[\text{h}^{\bullet}]$ ($K_{\text{OX}}\sqrt{p\text{O}_2} = 3 \times 10^{-8}$ to 3×10^{-3} , corresponding to $[\text{h}^{\bullet}] = 2.2 \times 10^{-5}$, 6.8×10^{-4} , 2.1×10^{-3} , and 6.6×10^{-3}) for 1000 K and intermediate degree of hydration ($K_{\text{hydrat}} p\text{H}_2\text{O} = 4 \times 10^{-4}$).

initial value. This characteristic overshooting behavior is found for all conditions investigated here.

Figure 4-3 plots the phenomenological diffusion coefficients, $D_{\text{H}}^{\text{eff}}$, $D_{\text{O}}^{\text{eff}}$, D_{fast} , D_{slow} at 1000 K as a function of $p\text{O}_2$ for intermediate and low degree of hydration and Figure 4-4 shows the Arrhenius plots. These four diffusion coefficients are in general not identical and are all required to fully describe the relaxation behavior of the system.

The values for $D_{\text{H}}^{\text{eff}}$ and $D_{\text{O}}^{\text{eff}}$ calculated from defect concentrations are equal to $D_{\text{H}_2\text{O}}^{\delta}$ at lower $p\text{O}_2$ and approach $D_{\text{OH}^{\cdot}_\text{o}}$ and $D_{\text{V}_\text{o}^{\cdot\cdot}}$ for increased $p\text{O}_2$ where the non-monotonic behavior is more pronounced. For sufficiently high $[\text{h}^{\cdot}]$ where the hydrogenation reaction is predominant, $D_{\text{H}}^{\text{eff}}$ approaches D_{H}^{δ} ($\approx D_{\text{OH}^{\cdot}_\text{o}}$ for high hole conductivity). Nevertheless, the kinetics of the remaining small amount of oxygen uptake is determined by $D_{\text{O}}^{\text{eff}}$ which even decreases for high $[\text{h}^{\cdot}]$ towards $D_{\text{V}_\text{o}^{\cdot\cdot}}$.

The behavior of D_{fast} and D_{slow} extracted from the predominant electronic conductivity is different from $D_{\text{H}}^{\text{eff}}$ and $D_{\text{O}}^{\text{eff}}$. An important consequence is that relaxation times extracted from thermogravimetry ($D_{\text{H}}^{\text{eff}}$, $D_{\text{O}}^{\text{eff}}$) are not necessarily identical to those from conductivity (D_{fast} ,

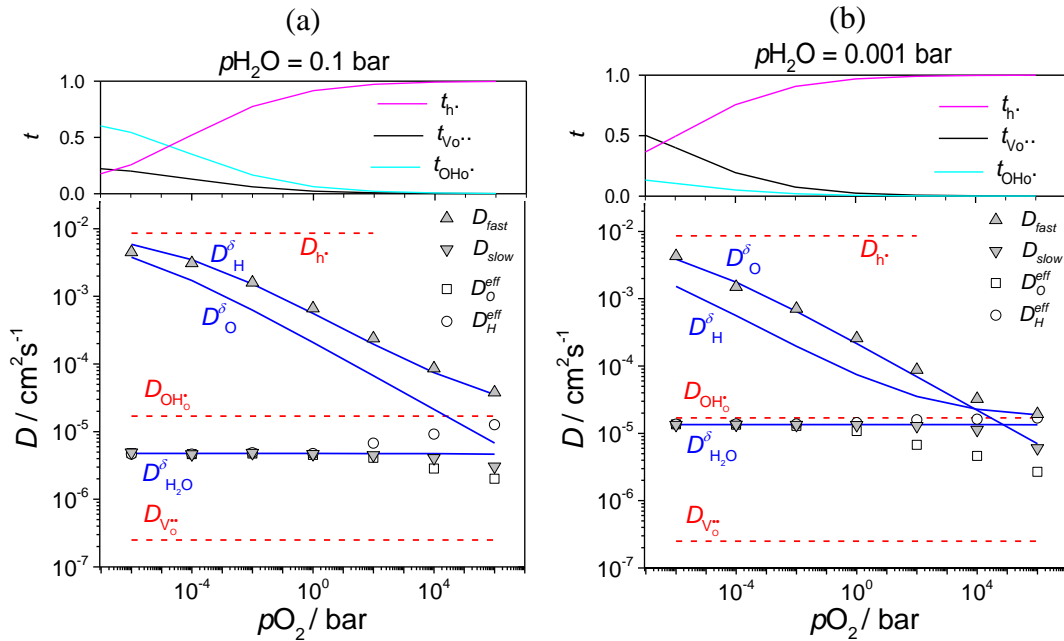


Figure 4-3: Extracted effective diffusion coefficients $D_{\text{H}}^{\text{eff}}$, $D_{\text{O}}^{\text{eff}}$ from the ionic defect concentration changes and D_{fast} , D_{slow} from the hole concentration change (= conductivity relaxation) at 1000 K after an increase of $p\text{H}_2\text{O}$, shown as function of $p\text{O}_2$: (a) for intermediate degree of hydration $p\text{H}_2\text{O} = 0.1$ bar, (b) for low degree of hydration $p\text{H}_2\text{O} = 0.001$ bar. The dashed and solid lines indicate the values of $D_{\text{OH}^{\cdot}_\text{o}}$, $D_{\text{V}_\text{o}^{\cdot\cdot}}$, $D_{\text{h}^{\cdot}}$ and D_{H}^{δ} , D_{O}^{δ} , $D_{\text{H}_2\text{O}}^{\delta}$.

D_{slow}). The non-monotonic behavior can be seen in the conductivity curves already for low $p\text{O}_2$. D_{fast} is similar to that value of the chemical diffusion coefficients D_{H}^{δ} or D_{O}^{δ} which is larger (under most of the studied conditions $D_{\text{H}}^{\delta} > D_{\text{O}}^{\delta}$, but for $t_{\text{V}_\bullet\bullet} > t_{\text{OH}_\bullet}$ this relation is inverted). Correspondingly, D_{fast} increases with decreasing $p\text{O}_2$ because for very low electronic transference number D_{H}^{δ} and D_{O}^{δ} approach $D_{\text{h}\cdot}$. D_{slow} is roughly similar to $D_{\text{H}_2\text{O}}^{\delta}$, only for the highest T in Figure 4-4 (c) (very high $p\text{O}_2$) it rather approaches D_{O}^{δ} . The difference between $D_{\text{H}}^{\text{eff}}$, $D_{\text{O}}^{\text{eff}}$, D_{fast} and D_{slow} can be understood as follows:

- $D_{\text{H}}^{\text{eff}}$ refers to the total proton uptake kinetics from hydration (low $[\text{h}\cdot]$) or hydrogenation (high $[\text{h}\cdot]$) reactions.
- $D_{\text{O}}^{\text{eff}}$ refers to the oxygen uptake kinetics which is determined by $D_{\text{H}_2\text{O}}^{\delta}$ in lower $p\text{O}_2$ where oxygen vacancies are consumed in the hydration reaction (single-fold process) and decreases to $D_{\text{V}_\bullet\bullet}$ at higher $p\text{O}_2$ where oxygen vacancies are annihilated through oxygenation reaction due to two-fold relaxation process.
- D_{fast} refers to the time-change of hole concentration caused by the redox reactions. For $t_{\text{V}_\bullet\bullet} < t_{\text{OH}_\bullet}$, $D_{\text{H}}^{\delta} > D_{\text{O}}^{\delta}$ holds, the respective redox reaction is hydrogen incorporation, and one finds $D_{\text{fast}} \approx D_{\text{H}}^{\delta}$. On the other hand, when $t_{\text{V}_\bullet\bullet} > t_{\text{OH}_\bullet}$, D_{O}^{δ} exceeds D_{H}^{δ} . This changes the relevant initial fast redox process from hydrogen uptake to oxygen release. Correspondingly, $D_{\text{fast}} \approx D_{\text{O}}^{\delta}$ holds.
- D_{slow} refers to the slow increase of $[\text{h}\cdot]$ after its minimum with a characteristic time typically related to the lower value of D_{O}^{δ} or $D_{\text{H}_2\text{O}}^{\delta}$.

For intermediate $p\text{H}_2\text{O}$, the material gradually changes from complete hydration below 500 K ($[\text{OH}_\bullet] \rightarrow 0.1$, $[\text{V}_\bullet\bullet] \rightarrow 0$) to almost complete dehydration above 1400 K. Correspondingly, $D_{\text{H}_2\text{O}}^{\delta}$ (blue solid line in Figure 4-4) changes from values close to $D_{\text{V}_\bullet\bullet}$ for large hydration towards D_{OH_\bullet} (see eq. (4.5)). In the transition region the effective activation energy of $D_{\text{H}_2\text{O}}^{\delta}$ rises up to 1.2 eV, i.e., clearly exceeds the migration energies of OH_\bullet (0.4 eV) as well as of $\text{V}_\bullet\bullet$ (0.8 eV).

The decoupling of $D_{\text{H}}^{\text{eff}}$ and $D_{\text{O}}^{\text{eff}}$ is not present at low $p\text{O}_2$ ($= 10^{-6}$ bar) bar (Figure 4-4 (a)), starts above 1200 K for $p\text{O}_2 = 1$ bar (Figure 4-4 (b)) and is present for all T at $p\text{O}_2 = 10^6$ bar (Figure 4-4 (c)). One interesting finding is the small or even negative activation energy for

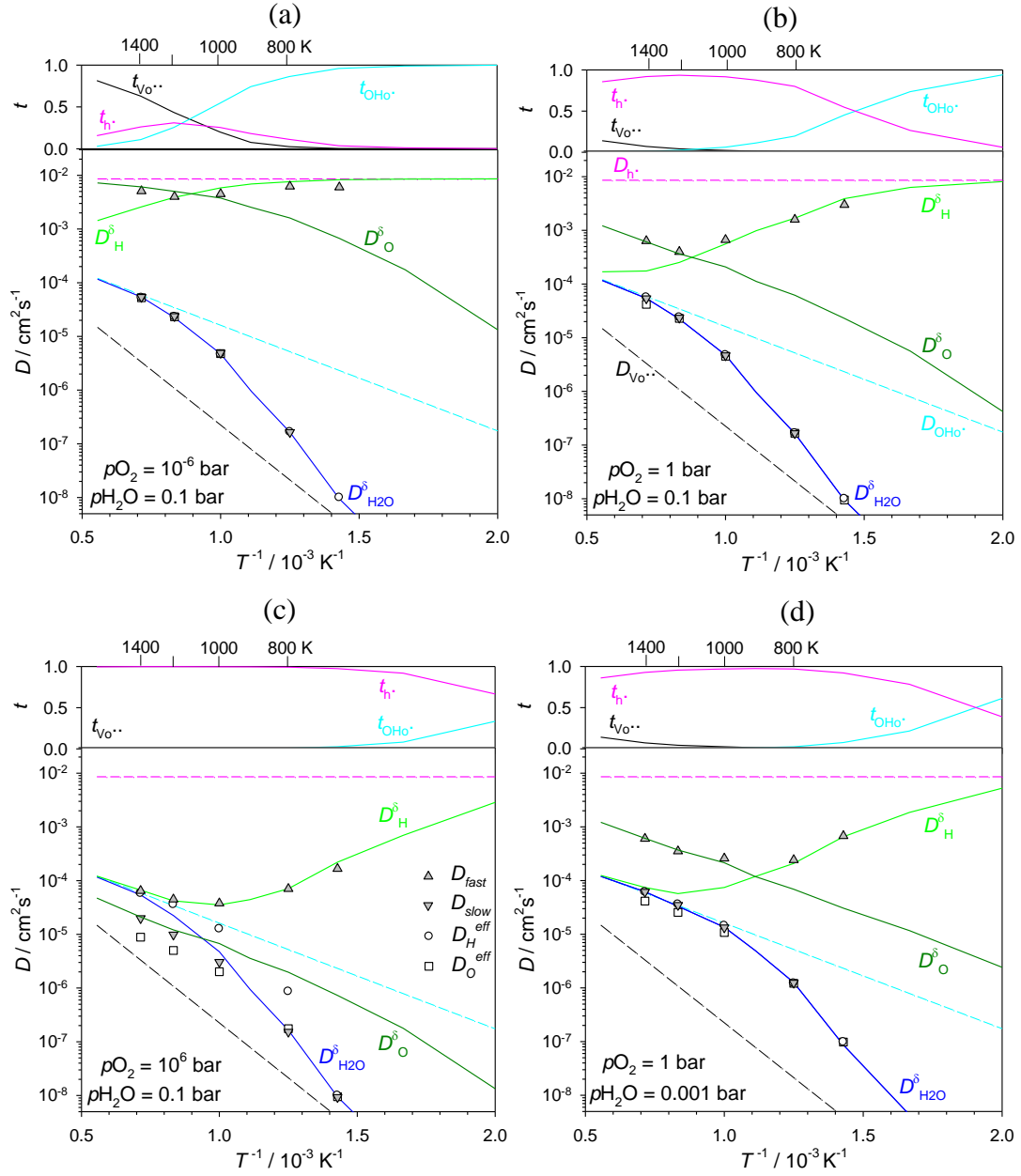


Figure 4-4: Arrhenius plot of $D_{\text{H}}^{\text{eff}}$, $D_{\text{O}}^{\text{eff}}$, D_{fast} , D_{slow} for (a) $p\text{O}_2 = 10^{-6}$ bar, (b) $p\text{O}_2 = 1$ bar, (c) $p\text{O}_2 = 10^6$ bar, (d) $p\text{O}_2 = 1$ bar, low hydration. Values of K_{hydrat} and K_{ox} according to the defect model in Figure 4-1, $p\text{H}_2\text{O} = 0.1$ bar for (a)-(c) and 0.001 bar for (d). For comparison, the defect diffusivities as well as D_{H}^{δ} , $D_{\text{H}_2\text{O}}^{\delta}$ are shown (dashed lines). Top plots: transference numbers.

D_{fast} due to the fact that D_{H}^{δ} changes from $D_{\text{H}}^{\delta} \approx D_{\text{OH}_0^{\delta}}$ at high T to $D_{\text{H}}^{\delta} \approx D_{\text{h}}^{\delta} > D_{\text{OH}_0^{\delta}}$ at low T (see eq. (4.3)).

The experimental results of non-monotonic relaxation in acceptor-doped $(\text{Ba,Sr})(\text{Zr,Ce})\text{O}_{3-\delta}$ perovskites report the activation energy of the fast process to be similar to D_{O}^{δ} in $T = 600\text{-}950^\circ\text{C}$ [53] (there are not experimental data available for $T < 600^\circ\text{C}$, i.e., the regime with negative apparent E_{a} for D_{fast}). This can hold according to the simulations, since

when $t_{V_O^{\bullet\bullet}} > t_{OH_O^{\bullet}}$ (high T), D_O^{δ} exceeds D_H^{δ} and $D_{fast} \approx D_O^{\delta}$. This is realized by a fast O release instead of H uptake as explained before. However, the magnitude of the simulated D_{fast} and D_O^{δ} activation energy is smaller than the experimental values found in [53]. This can have two reasons: (i) for acceptor-doped BaZrO₃ and BaCeO₃ materials the holes might have a non-negligible migration barrier corresponding to small polarons (in contrast to SrTiO₃; possibly caused by the larger lattice constant in BaZrO₃ and BaCeO₃). Such a defect model is suggested in [59], however, comprising a comparably high hole migration barrier of 0.9 eV. (ii) Trapping of holes, e.g., at transition metal impurities or close to acceptor dopants might play a role, too. Both effects would increase the activation energy of D_O^{δ} .

Therefore, the effect of hole trapping is now included in the defect model and stoichiometry relaxation simulation. In particular, this will modify the activation energy (E_a) of D_{fast} at low T . Considering the two cases of weak ($\Delta H_{tr}^{\circ} = -0.3$ eV and $\Delta S_{tr}^{\circ} = 0$) and strong ($\Delta H_{tr}^{\circ} = -0.6$ eV and $\Delta S_{tr}^{\circ} = 0$) trapping, the change of defect concentrations (including also the trapped holes $[A'h^{\bullet}]$) as a function of pO_2 is shown in Figure 4-5 (800 K and intermediate degree of hydration). The trapping does not alter the defect conductivities much. With weak trapping (figure 4-5 middle) the concentrations of $V_O^{\bullet\bullet}$, OH_O^{\bullet} and untrapped h^{\bullet} remain essentially unchanged, but since $[A'h^{\bullet}] > [h^{\bullet}]$ the total (free+trapped) hole concentration is significantly increased. Only for strong trapping at high pO_2 , $[A'h^{\bullet}]$ becomes important in the electroneutrality condition and modifies also $V_O^{\bullet\bullet}$ and OH_O^{\bullet} concentrations (figure 4-5 right).

However, there can be a strong effect on D_{fast} as can be seen in Figure 4-6. For the case of only h^{\bullet} and $V_O^{\bullet\bullet}$, hole trapping affects D_O^{δ} according to [60]

$$D_O^{\delta} = t_{h^{\bullet}} \cdot D_{V_O^{\bullet\bullet}} + t_{V_O^{\bullet\bullet}} \chi_{h^{\bullet}} \cdot D_{h^{\bullet}} \quad (4.6)$$

where the trapping factor $\chi_{h^{\bullet}}$

$$\chi_{h^{\bullet}} = \frac{\partial[h^{\bullet}]}{\partial[h^{\bullet}] + \partial[A'h^{\bullet}]} \quad (4.7)$$

gives the differential fraction of the untrapped holes. Analogously, D_O^{δ} in the 3-carrier case from eq. (4.4) is modified to

$$D_O^{\delta} = \frac{t_{h^{\bullet}}}{t_{h^{\bullet}} + t_{V_O^{\bullet\bullet}}} D_{V_O^{\bullet\bullet}} + \frac{t_{V_O^{\bullet\bullet}}}{t_{h^{\bullet}} + t_{V_O^{\bullet\bullet}}} \chi_{h^{\bullet}} \cdot D_{h^{\bullet}} \quad (4.8)$$

The Arrhenius plot for the case of weak trapping is almost identical to that without hole trapping (figure 4-4 (b)) except that D_{fast} is less than an order of magnitude smaller due to

decrease from D_h to $\chi_h D_h$. For the case of strong trapping, D_{fast} is strongly different in the whole T range. In this case, $D_{fast} \approx D_H^{eff} \approx D_{OH_O}$ and $D_{slow} \approx D_O^{eff} \approx D_{H_2O}^\delta$ and thus D_{fast} exhibits a positive E_a for the complete T range. While strong trapping decreases the ratio between D_{fast} and D_{slow} (i.e. brings the time constants of the two-fold conductivity relaxation process closer together) because the effective hole mobility is decreased to $\chi_h D_h$, on the other hand the splitting between D_H^{eff} and D_O^{eff} becomes more pronounced. This is caused by the fact that the sum of free and trapped holes is much larger than the hole concentration without trapping, and both free and trapped holes contribute to the decoupling of V_O^\bullet and OH_O^\bullet migration after a pH_2O change.

In conclusion, the simulation procedure for typical electrolytes such as acceptor-doped $BaZrO_3$ and $BaCeO_3$ reveals that all phenomenological diffusion coefficient including D_{fast} , D_{slow} , D_H^{eff} and D_O^{eff} are needed to be considered for fully understanding the relaxation kinetics. The non-monotonic behavior appears at higher pO_2 and T where t_h is larger. The complex variation in the Arrhenius plots suggests that the study of phenomenological diffusion coefficients performed in an extended T range could be used to validate a defect model without or with trapping. The model is in principle also applicable for the cathode perovskite, but is further complicated by the hole-hole and hole-proton defect interactions which are discussed in more detail in section 4.2.5.

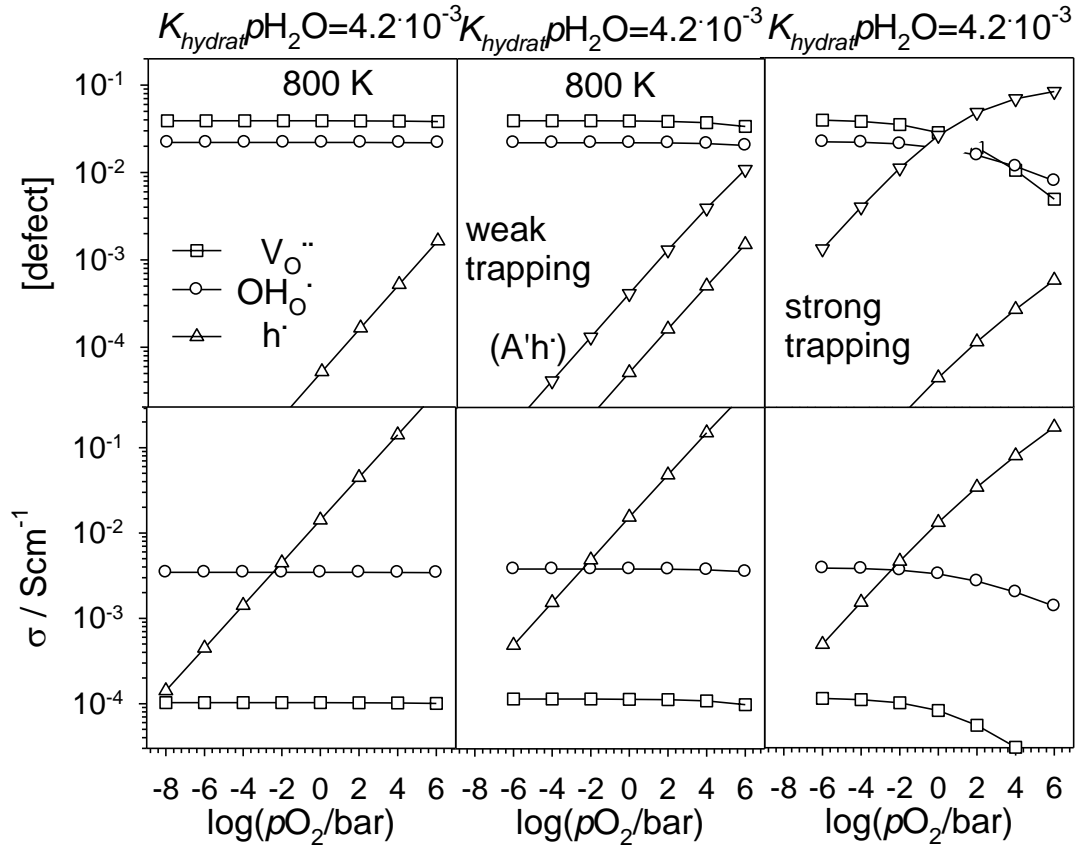


Figure 4-5: Defect concentrations and partial conductivities for intermediate degree of hydration ($K_{\text{hydrat}} p_{\text{H}_2\text{O}} = 4.2 \times 10^{-3}$) at 800 K with no trapping (left), weak trapping (0.3 eV, middle) and strong trapping (0.6 eV, right).

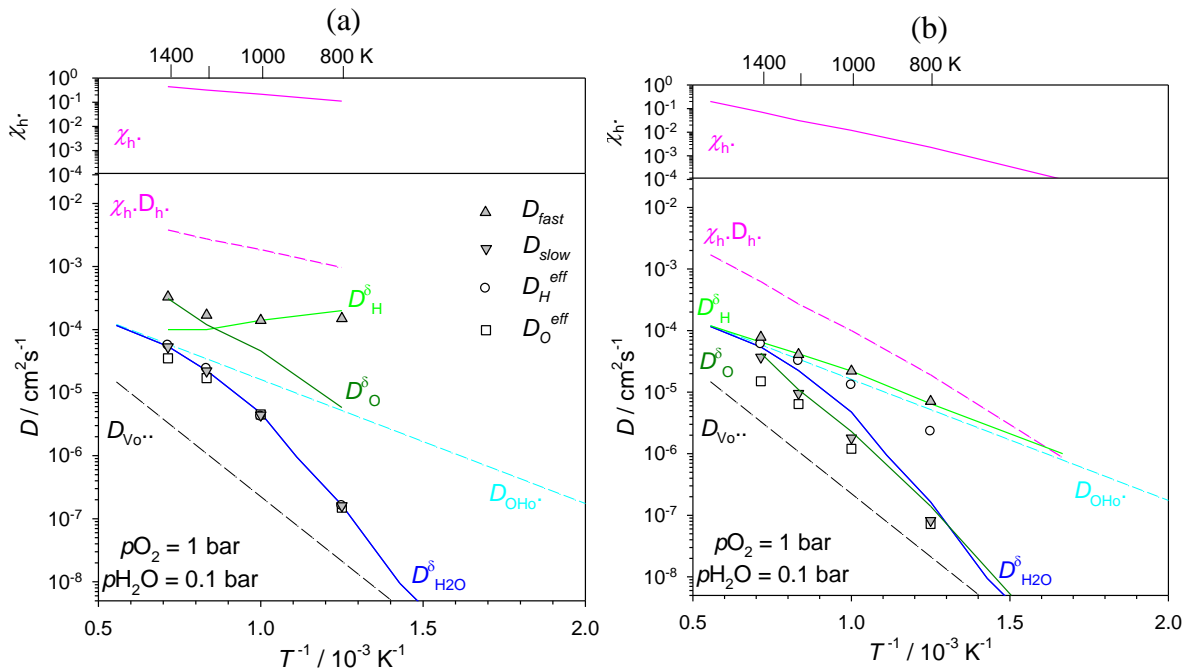


Figure 4-6: Arrhenius plot of $D_{\text{H}}^{\text{eff}}$, $D_{\text{O}}^{\text{eff}}$, D_{fast} , D_{slow} for $p_{\text{O}_2} = 1 \text{ bar}$ and $p_{\text{H}_2\text{O}} = 0.1 \text{ bar}$ for (a) weak and (b) strong trapping. For comparison, the defect diffusivities as well as D_{H}^{δ} , $D_{\text{H}_2\text{O}}^{\delta}$ are shown (dashed lines). Top plots: transference numbers.

4.2 Proton uptake in mixed-conducting perovskites

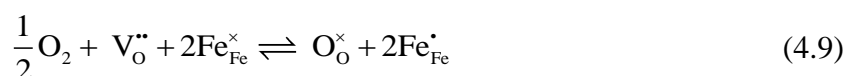
4.2.1 Proton-conducting cathode materials

A promising proton-conducting cathode material should show both sufficient electronic (σ_{eon} larger than about 10 Scm^{-1} [61]) and proton conductivity ($\sigma_{\text{OH}\cdot} \geq 10^{-5} \text{ Scm}^{-1}$ [20]) to function well in a PCFC. The latter is required to activate the whole surface of the cathode for the oxygen reduction reaction by enabling the protons to travel from electrolyte through the cathode material to the whole cathode surface (“bulk path”). Mixed-conducting perovskites with redox active transition metals (Fe, Co, Ni and Mn) on the B-site provide highly electronically conducting cathode materials with promising catalytic activity for the oxygen reduction reaction. Only minor substitution of transition metal by ($\leq 30\%$) Zn, Zr and Y on the B-site are allowed since they suppress the electronic conductivity. Examples are $\text{Ba}(\text{Zr,Pr})\text{O}_{3-\delta}$ [62], $\text{Ba}(\text{Zr,Mn})\text{O}_{3-\delta}$ [63], $\text{Ba}(\text{Zr,Fe})\text{O}_{3-\delta}$ [64] in which the electronic conductivity is not high enough to satisfy the required criterion for a good cathode.

This work mainly focuses on Fe-containing perovskites since they show relatively higher proton incorporation compared to Co-rich counterparts [24], but also studies some Co containing materials as they tend to have a higher catalytic activity. The TG results for BL15F in dry and humid oxidizing condition are first exemplified in detail; then the proton incorporation in different perovskite cathodes and correlation between proton incorporation and various element substitutions in A- and B-sites is discussed. The non-ideal behavior and defect interactions are then qualitatively and quantitatively explained. Alternative methods such as Karl-Fischer titration, mass spectroscopy and impedance spectroscopy are applied to measure proton concentration/mobility in some of these materials. Finally, relevant points about PCFC kinetics are discussed.

4.2.2 Detailed example: $\text{Ba}_{0.85}\text{La}_{0.15}\text{FeO}_{3-\delta}$ (BL15F)

TG results for BLF15F in dry 850 ppm, 0.84%, 8.3%, and 83% O_2 comprising the oxygen non-stoichiometry profile and oxygenation van 't Hoff plot are shown in Figure 4-7. At higher T and lower $p\text{O}_2$, δ reaches a plateau since all iron ions are in their 3+ oxidation state ($\delta = 2.575$). Due to polaron type mobility of holes in ferrates [65], one can assume that the holes are trapped as Fe^{4+} ($\text{Fe}_{\text{Fe}}^{\bullet} =$ trapped holes) and therefore, the oxygenation reaction can be written as



with mass action constant of

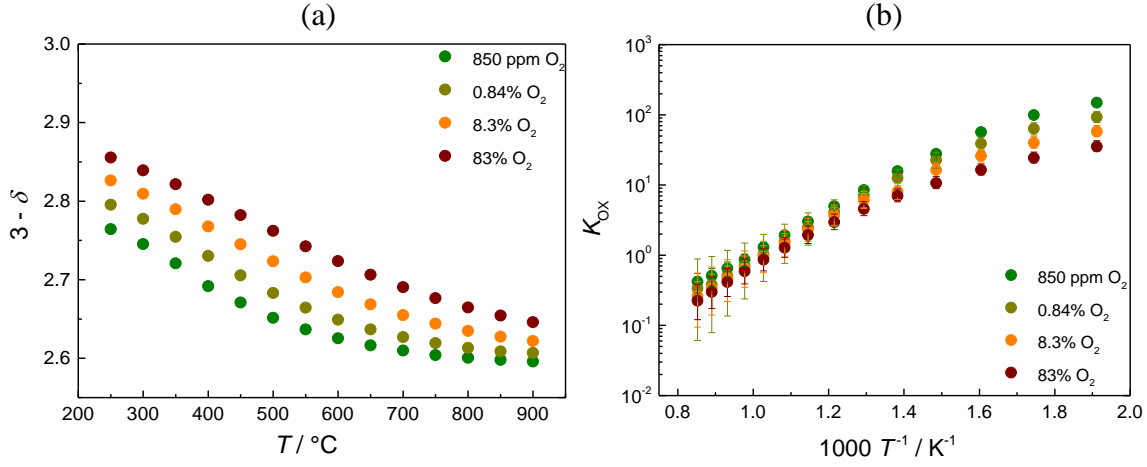


Figure 4-7: TG results for BL15F fine powder in dry 850 ppm, 0.84%, 8.3% and 83% O_2 . (a) Oxygen non-stoichiometry. (b) oxygenation van 't Hoff plot. The error bars are calculated assuming $\Delta\delta = 0.02$.

$$K_{\text{OX}} = \frac{[\text{O}_\text{O}^\times][\text{Fe}_\text{Fe}^\bullet]^2}{\sqrt{p\text{O}_2}[\text{V}_\text{O}^{\bullet\bullet}][\text{Fe}_\text{Fe}^\times]^2} = \frac{(3-\delta)(0.85-2\delta)^2}{\sqrt{p\text{O}_2}\delta(0.15+2\delta)^2} \quad (4.10)$$

The nonlinearity of van 't Hoff plot, but also different values of K_{OX} in different $p\text{O}_2$ indicate that the system is not ideally dilute. At lower T where the hole concentration increases, the van 't Hoff plot becomes less steep corresponding to less favorable oxygenation. This can be attributed to stronger hole-hole interaction at lower T where hole concentration increases. K_{OX} is higher at lower $p\text{O}_2$ corresponding to more favorable oxygenation when more oxygen vacancies are available.

The results for BL15F in humid 100 ppm O_2 for an equilibrated and quenched sample are shown in Figure 4-8. The sample was quenched from 700 $^\circ\text{C}$ ($\delta = 0.4$, $[\text{Fe}_\text{Fe}^\bullet] = 0.05$) where the hole concentration is small. The proton concentration is calculated assuming that the sample is always in the predominant hydration regime ($2[\text{V}_\text{O}^{\bullet\bullet}] > [\text{Fe}_\text{Fe}^\bullet]$, $\text{H}_2\text{O} + \text{V}_\text{O}^{\bullet\bullet} + \text{O}_\text{O}^\times \rightleftharpoons 2\text{OH}_\text{O}^\bullet$) and therefore, the mass action law can be written as

$$K_{\text{hydrat}} = \frac{[\text{OH}_\text{O}^\bullet]^2}{p\text{H}_2\text{O}[\text{V}_\text{O}^{\bullet\bullet}][\text{O}_\text{O}^\times]} \quad (4.11)$$

At certain T and $p\text{O}_2$, at least two data points at different $p\text{H}_2\text{O}$ are required to numerically solve for $[\text{OH}_\text{O}^\bullet]$ and K_{hydrat} since oxygen non-stoichiometry is already known from dry measurements.

The proton concentration of the sample with equilibrated oxygen stoichiometry (solid blue circles, 15.7 mbar H_2O) is smaller than for the quenched sample and the difference is larger than what one expects from the change in oxygen vacancy concentration. This can be explained by more detrimental proton-hole interaction for the equilibrated sample with higher hole concentration (see 4.2.5). Despite $\delta = 0.4$, $[\text{OH}_\text{O}^\bullet]$ increases only to 0.016 per BL15F formula unit even at lowest T of 200 $^\circ\text{C}$. The hydration van 't Hoff plot is linear and is more

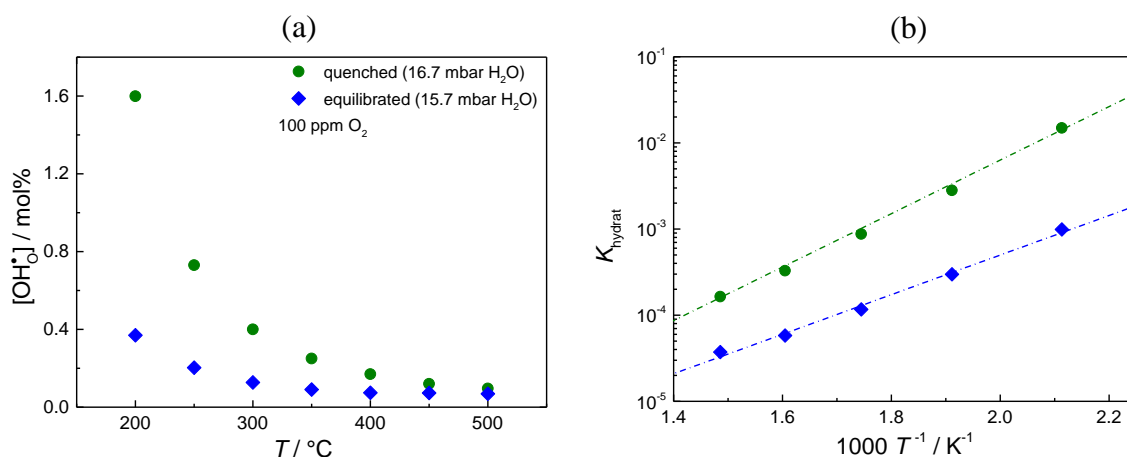


Figure 4-8: TG results in humid condition for BL15F particles: (a) Proton concentration of the sample with equilibrated O-stoichiometry (solid blue circles, 15.7 mbar H_2O) and quenched O-stoichiometry (solid green circles, 16.7 mbar H_2O). (b) Hydration van 't Hoff plot.

step for the quenched sample than the O-equilibrated one resulting in $\Delta H_{\text{hydrat}}^{\circ} = -44 \pm 2$ kJmol^{-1} and $\Delta S_{\text{hydrat}}^{\circ} = -151 \pm 4$ $\text{Jmol}^{-1}\text{K}^{-1}$ for the equilibrated sample and $\Delta H_{\text{hydrat}}^{\circ} = -60 \pm 2$ kJmol^{-1} and $\Delta S_{\text{hydrat}}^{\circ} = -160 \pm 2$ $\text{Jmol}^{-1}\text{K}^{-1}$ for the quenched one.

In humid 100% O_2 , ~ 2.5 g of BL15F gained 10-17 μg in the T range of 200-300 $^{\circ}\text{C}$ ($\delta \sim 0.17$, $[\text{h}^{\bullet}] \sim 0.51$) and $p\text{H}_2\text{O}$ range of 6.6-15.7 mbar which is much smaller than in 100 ppm O_2 which gained ~ 40 -120 μg in this T range. Assuming proton uptake by hydrogenation reaction ($[\text{Fe}_{\text{Fe}}^{\bullet}] > 2[\text{V}_{\text{O}}^{\bullet\bullet}]$, $\text{H}_2\text{O} + 2\text{h}^{\bullet} + 2\text{O}_{\text{O}}^{\times} \rightleftharpoons 2\text{OH}_{\text{Fe}}^{\bullet} + 1/2\text{O}_2$), this would result in less than 0.5 mol% of proton incorporation. The proton concentration in humid 100% O_2 and the respective hydration van 't Hoff plot is shown in Figure 4-9.

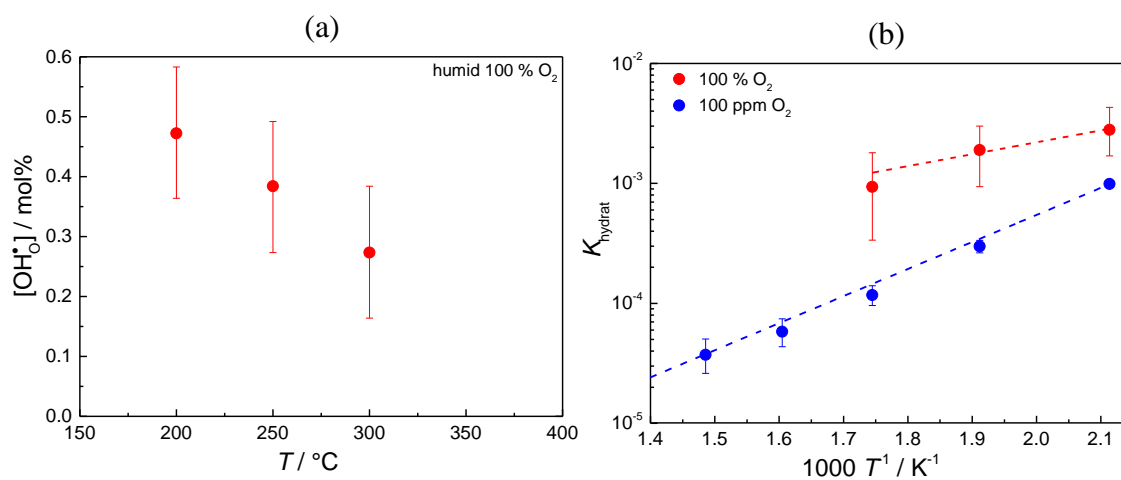


Figure 4-9: (a) BL15F proton concentration in humid 100 % O_2 assuming hydrogenation. (b) Corresponding van 't Hoff plot in 100 ppm O_2 and 100% O_2 . The error bars are calculated assuming $\Delta m = \pm 2$ μg due to noisy baseline.

4.2.3 Proton uptake in different materials

In this section, the results of TG measurements in dry and humid oxidizing condition for different materials are briefly presented and the trends of proton uptake and correlation to properties such as electronegativity, Goldschmidt tolerance factor and oxygen vacancy concentration are discussed.

4.2.3.1 SF, BSF, LSF

SF- ~ 3.3 g of SF particles were quenched from 700 °C to 200-300 °C and the sample gained only 20-40 µg when humidity changed from 6.6 to 15.7 mbar H₂O corresponding to [OH₀[•]] ~ 0.01-0.03%. XRD after TG confirmed that the Brownmillerite phase (oxygen vacancy ordered super-structure) is formed. This is expected to disfavor proton uptake despite $\delta = 0.5$ [66].

LSF- The oxygen non-stoichiometry and oxygenation van 't Hoff plot for LSF are shown in Figure 4-10. At lower T , δ approaches zero independent of pO_2 which is in line with data in the literature [67]. The van 't Hoff plot is calculated assuming that all holes in the system are trapped as Fe⁴⁺ (Fe_{Fe}[•]). It deviates from linearity and K_{OX} changes with pO_2 , indicating that the system is not ideally dilute. Regarding proton uptake, LSF is in the hydrogenation regime ($2[V_O^{\bullet\bullet}] < [Fe_{Fe}^{\bullet}]$) and TG measurements in humid 100 ppm and 100% O₂ showed that for ~ 4 g of LSF, the weight gain in T range of 250-400 °C ($\delta = 0$) is less than 10 µg when pH_2O changed from 6.6 to 15.7 mbar. The sample was then quenched from 800 °C ($\delta = 0.18$, [h[•]] = 0.14, 100 ppm O₂) to lower T and the weight gain was still small. This can be rationalized by a very unfavorable hydration enthalpy or strong interaction of protons and holes. In the latter case, the activity of the trapped holes exceeds their nominal concentration and thus in terms of activity, $a_{V_O^{\bullet\bullet}} < a_{Fe_{Fe}^{\bullet}}$ and correspondingly the system would switch to predominant hydrogenation.

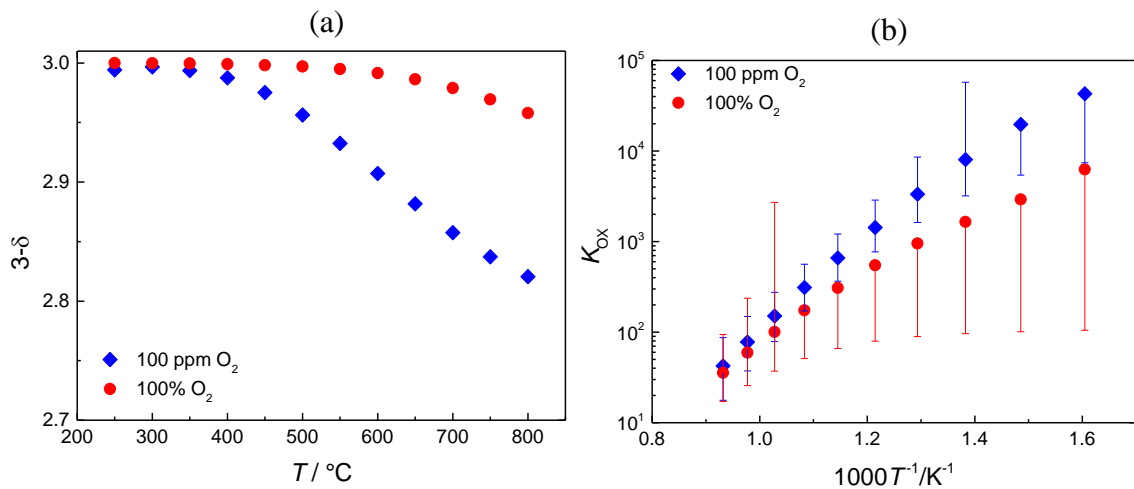


Figure 4-10: TG measurements in dry 100 ppm and 100% O₂ for LSF particles (a) oxygen non-stoichiometry: δ approaches 0 at low T . (b) Corresponding nonlinear oxygenation van 't Hoff plot.

BSF- TG results in dry and humid condition for *BSF* are shown in Figure 4-11. The oxygen non-stoichiometry approaches 0.5 at high T and low pO_2 corresponding to the point where all Fe ions are in their 3+ oxidation state (Figure 4-11 (a)). The nonlinearity of the van 't Hoff plot confirms the non-ideal behavior of these cathode materials once more (Figure 4-11 (b)). The proton concentration and hydration van 't Hoff plot is shown in Figure 4-11 (c) and (d). For the sample with quenched O stoichiometry, a similar behavior is found as for the other materials. The van 't Hoff plot of the quenched sample is linear with $\Delta H_{\text{hydrat}}^{\circ} = -61 \pm 3 \text{ kJmol}^{-1}$ and $\Delta S_{\text{hydrat}}^{\circ} = -150 \pm 5 \text{ Jmol}^{-1}\text{K}^{-1}$. In contrast, for the O-equilibrated sample, the proton uptake decreases below a certain T where proton-hole interaction increases, resulting in a bent van 't Hoff plot (see 4.2.5 for more details). To ensure that this might not be due to oxygen vacancy ordering at low T , a small amount of particles was annealed at 600 °C for two days and then at 300 °C for fourteen days, but the XRD showed no traces of super structure formation. In humid 100% O_2 , no significant weight change was observed in TG due to large contribution of holes at lower T (250 °C, $\delta = 0.18$, $[h^{\bullet}] = 0.64$) which pushes the system into hydrogenation regime ($2[V_{\text{O}}^{\bullet\bullet}] < [Fe_{\text{Fe}}^{\bullet}]$) and also disfavors proton uptake by proton-hole interaction.

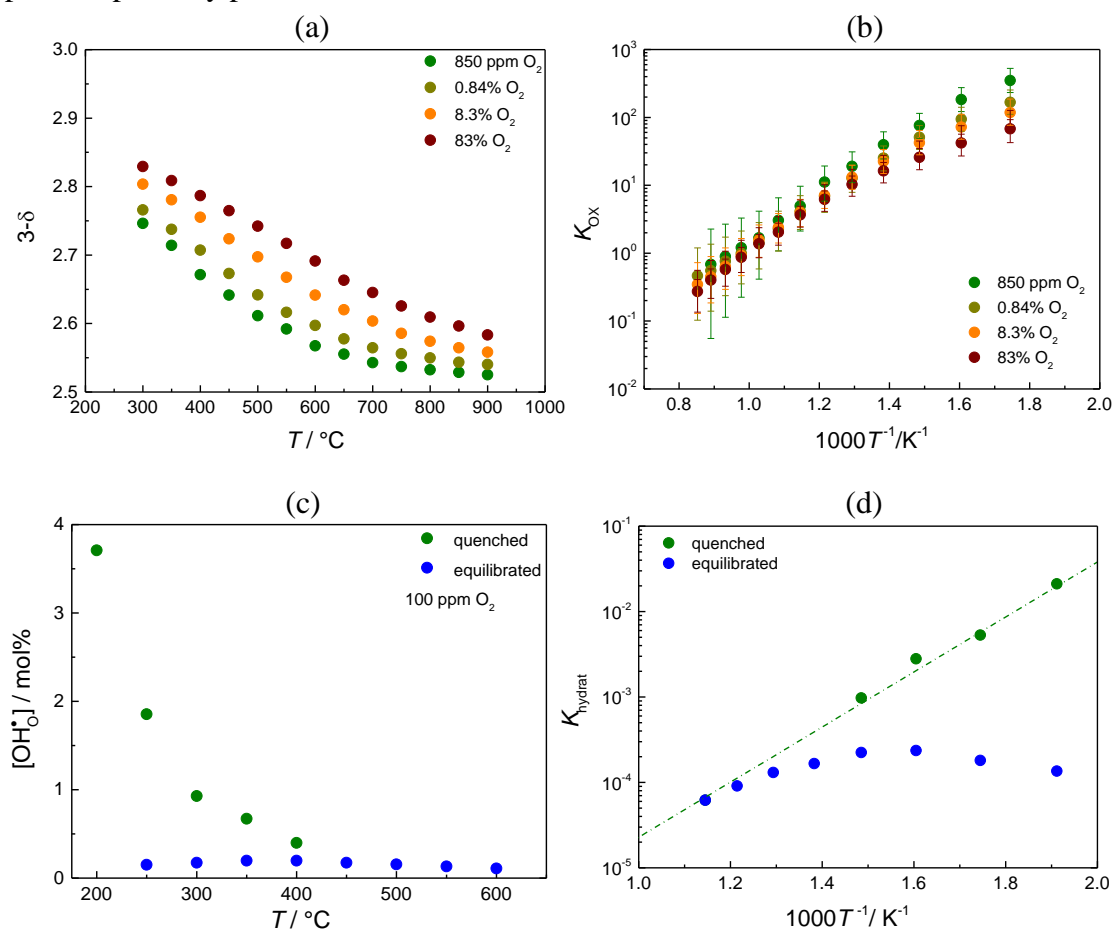


Figure 4-11: (a) Oxygen non-stoichiometry of fine powder of *BSF* (b) and the respective nonlinear oxygenation van 't Hoff plot. (c) Proton concentration for the quenched (from 600 °C, where $\delta = 0.43$ and $[h^{\bullet}] = 0.14$) and equilibrated *BSF* particles in 100 ppm O_2 and 15.7 mbar H_2O . (d) Corresponding hydration van 't Hoff plot.

In general, BSF takes up more protons compared to SF due to presence of Ba on the A-site which prevents formation of the Brownmillerite phase and increases the oxide ion basicity. LSF takes up fewer protons compared to SF and BSF as La^{3+} is less basic than Sr^{2+} and Ba^{2+} and $[\text{V}_\text{O}^{\bullet\bullet}]$ is smaller.

4.2.3.2 BL5F, BL15F, BL25F, BL50F

The oxygen non-stoichiometries of the BLF series with different La substitution are shown in Figure 4-12. For BL50F, the weight gain reaches a plateau at low T and high $p\text{O}_2$ indicating that all Fe ions are Fe^{4+} . For the rest of the materials, a plateau is observed at high T and low $p\text{O}_2$ where all Fe ions are reduced to Fe^{3+} . The results show that by increase of La content δ decreases, which has a significant effect on hydration of the systems. The van 't Hoff plots and hole-hole interaction will be later discussed in 4.2.5.

The proton concentration for the equilibrated and quenched samples in 100 ppm O_2 are shown in Figure 4-13, the van 't Hoff plots of K_{hydrat} and possible proton-hole interactions will be explored later in 4.2.4.

BL5F with highest oxygen vacancy concentration (approaching 0.475 at high T and low

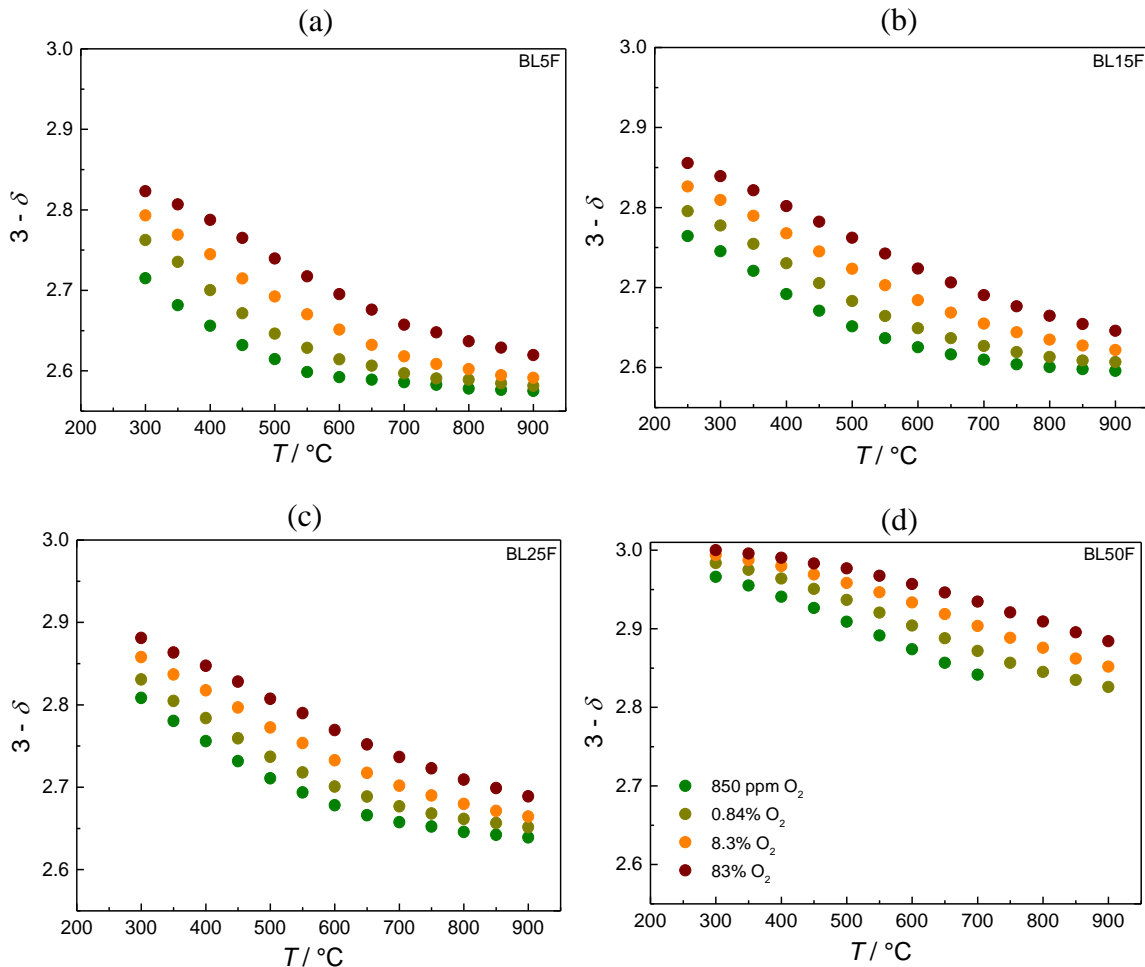


Figure 4-12: Oxygen non-stoichiometry for (a) BL5F, (b) BL15F, (c) BL25F and (d) BL50F powder in dry $p\text{O}_2$.

$p\text{O}_2$, hydration regime) takes up more than 3 mol% of protons at 200 °C and 15.6 mbar H_2O in equilibrium. $[\text{OH}_\text{O}^\bullet]$ is more than 5 mol% for the sample quenched from 700 °C starting from dry condition (16.7 mbar H_2O , 200 °C). The higher $[\text{OH}_\text{O}^\bullet]$ for the sample with quenched O-stoichiometry is due to higher $[\text{V}_\text{O}^{\bullet\bullet}]$ and smaller proton-hole interaction due to decreased hole concentration. Standard hydration enthalpy and entropy for the equilibrated and quenched samples are $\Delta H_{\text{hydrat}}^\circ = -53 \pm 2 \text{ kJmol}^{-1}$ and $\Delta S_{\text{hydrat}}^\circ = -134 \pm 3 \text{ Jmol}^{-1}\text{K}^{-1}$ and $\Delta H_{\text{hydrat}}^\circ = -62 \pm 3 \text{ kJmol}^{-1}$ and $\Delta S_{\text{hydrat}}^\circ = -144 \pm 5 \text{ Jmol}^{-1}\text{K}^{-1}$, respectively. In humid 100% O_2 , the weight gain is negligible and only buoyancy effect can be observed.

BL15F takes up fewer protons compared to BL5F due to decrease of $[\text{V}_\text{O}^{\bullet\bullet}]$ and basicity of oxide ion (La^{3+} is more electronegative than Ba^{2+}). The system is still mainly in the hydration regime and the thermodynamic parameters are $\Delta H_{\text{hydrat}}^\circ = -44 \pm 2 \text{ kJmol}^{-1}$ and $\Delta S_{\text{hydrat}}^\circ = -151 \pm 4 \text{ Jmol}^{-1}\text{K}^{-1}$ for the O-equilibrated and $\Delta H_{\text{hydrat}}^\circ = -60 \pm 2 \text{ kJmol}^{-1}$ and $\Delta S_{\text{hydrat}}^\circ = -160 \pm 2 \text{ Jmol}^{-1}\text{K}^{-1}$ for the quenched sample. In humid 100% O_2 , the sample gained $\sim 9\text{-}18 \mu\text{g}$ in T range of 200-300 °C. Assuming hydrogenation, this would result in proton concentrations less than 0.5 mol%.

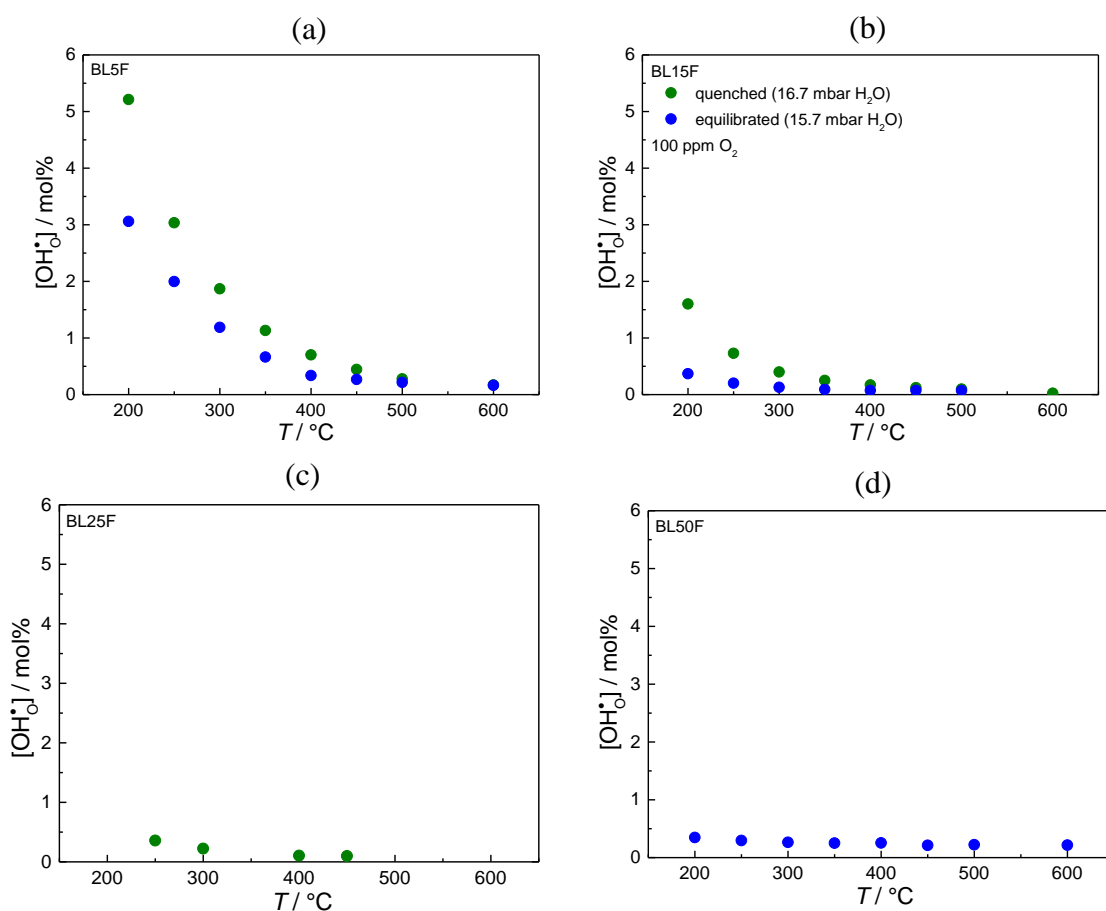


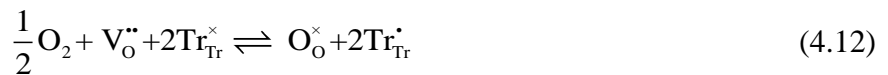
Figure 4-13: Proton concentration for the equilibrated (blue, 6.6-10.6-15.6 mbar H_2O) and quenched (from 700 °C, green) particles of (a) BL5F (b) BL15F (c) BL25F (d) BL50F in 100 ppm O_2 .

The proton concentration decreases even more in BL25F to less than 0.5 mol% at 250 °C and 16.7 mbar H₂O for the quenched sample with $\Delta H_{\text{hydrat}}^{\circ} = -44 \pm 5 \text{ kJmol}^{-1}$ and $\Delta S_{\text{hydrat}}^{\circ} = -143 \pm 7 \text{ Jmol}^{-1}\text{K}^{-1}$. The sample is still assumed to be predominantly in the hydration regime.

In BL50F, the hole concentration increases and the system is predominantly in the hydrogenation regime ($[\text{Fe}_{\text{Fe}}^{\bullet}] > 2[\text{V}_{\text{O}}^{\bullet\bullet}]$). The proton concentration of the equilibrated sample decreases to less than 0.35 mol% in the covered T range, with $\Delta H_{\text{hydrog}}^{\circ} = -53 \pm 2 \text{ kJmol}^{-1}$ and $\Delta S_{\text{hydrog}}^{\circ} = -133 \pm 2 \text{ Jmol}^{-1}\text{K}^{-1}$. The BL50F particles were also equilibrated at 800 °C and quenched to lower T and the weight gain upon water partial pressure change was almost the same as for the equilibrated sample. This is either because the hole concentration even at high T is high enough to suppress the proton uptake, or the oxygenation reaction is not successfully frozen in. The experiment was also performed in reducing condition to ensure that all Fe ions are in their 3+ oxidation state. However, the weight changes were still small and increased with T which might be due to change of $p\text{O}_2$ which for given $p\text{H}_2\text{O}$ and $p\text{H}_2$ depends on T . In humid 100% O₂, the weight gain is small (less than 10 µg in T range of 200-400 °C) resulting in a proton concentration less than 0.25 mol%.

4.2.3.3 BCFZr [68], BSCF

BCFZr- The result of thermogravimetry in dry condition is shown in Figure 4-14. The inflection point in the oxygen non-stoichiometry profile corresponds to the point where the average oxidation state of Fe and Co is 3+ ($\delta = 0.4$). At lower $p\text{O}_2$ and higher T , δ increases above 0.4 due to reduction of cobalt to Co^{2+} which is in analogy with similar findings for $\text{Ba}_{1-x}\text{Sr}_x\text{Co}_{0.8}\text{Fe}_{0.2}\text{O}_{3-\delta}$ [69]. The van 't Hoff plot can be calculated in two ways. First, it can be assumed that (apart from 100 ppm O₂ and $T > 600$ °C) cobalt is always 3+ and only iron changes its oxidation state between 3+ ($\text{Fe}_{\text{Fe}}^{\times}$) and 4+ ($\text{Fe}_{\text{Fe}}^{\bullet}$ = trapped holes). This results in Figure 4-14 (b) which indicates deviation from ideally dilute behavior. The alternative approach of considering Fe and Co equally participating in the redox reaction (Tr stands for the transition metal, Fe or Co in this case) is



with mass action constant of

$$K_{\text{ox}} = \frac{(3-\delta)(0.8-2\delta)^2}{\sqrt{p\text{O}_2}\delta(2\delta)^2} \quad (4.13)$$

which gives slightly different results, but also indicates non-ideality (Figure 4-14 (c)).

Figure 4-15 shows the TG results in humid 100 ppm O₂ where the sample is expected to be in the hydration regime. The resulting values of K_{hydrat} are shown in Figure 4-15 (a). They

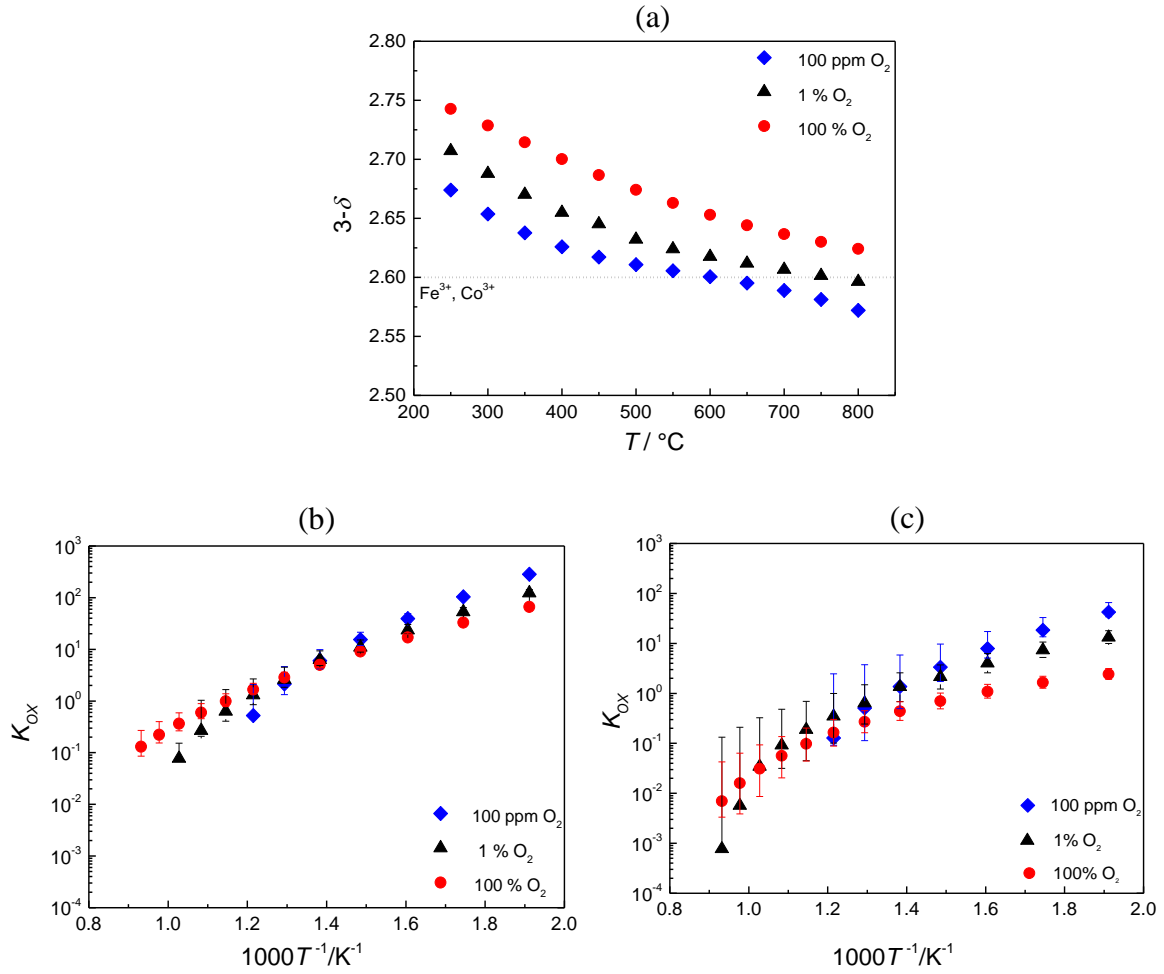


Figure 4-14: TG results in dry oxidizing atmosphere for BCFZr particles: (a) absolute oxygen non-stoichiometry. (b) Oxygenation van't Hoff plot according to the reaction (4.9) and (c) oxygenation van't Hoff plot according to eq. (4.13).

yield a straight van't Hoff plot with $\Delta H_{\text{hydrat}}^{\circ} = -33 \pm 5 \text{ kJmol}^{-1}$ and $\Delta S_{\text{hydrat}}^{\circ} = -103 \pm 5 \text{ Jmol}^{-1}\text{K}^{-1}$ for the O-equilibrated sample and $\Delta H_{\text{hydrat}}^{\circ} = -56 \pm 7 \text{ kJmol}^{-1}$ and $\Delta S_{\text{hydrat}}^{\circ} = -137 \pm 12 \text{ Jmol}^{-1}\text{K}^{-1}$ for the quenched one.

The situation is rather complex in 100% O_2 for the equilibrated sample (Figure 4-16). At 250 °C, $[\text{V}_{\text{O}}^{\bullet\bullet}] = 0.27$ and $[\text{Fe}_{\text{Fe}}^{\bullet}] = 0.26$ and the sample should theoretically still take up protons by hydration ($2[\text{V}_{\text{O}}^{\bullet\bullet}] > [\text{Fe}_{\text{Fe}}^{\bullet}]$). The weight gain should therefore be only moderately less than in 100 ppm O_2 , but the decrease is much more drastic (~ 5 times). This can be explained by strong interaction of protons and holes at higher $p\text{O}_2$. The maximum possible K_{hydrat} (open red circles in top part of Figure 4-16) is calculated from the hydrogenation reaction and the solid red circles correspond to the lower limit of proton concentration calculated from the hydration reaction.

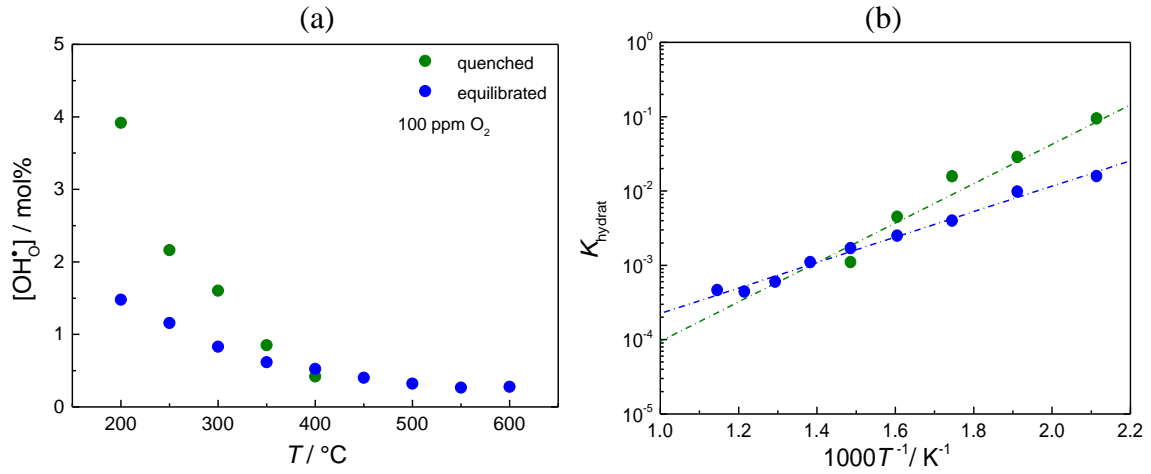


Figure 4-15: (a) Proton concentration for the equilibrated BCFZr particles and the particles quenched from 600 °C in 100 ppm O_2 (6.6-10.6-15.6 mbar H_2O) (b) and the respective hydration van 't Hoff plot.

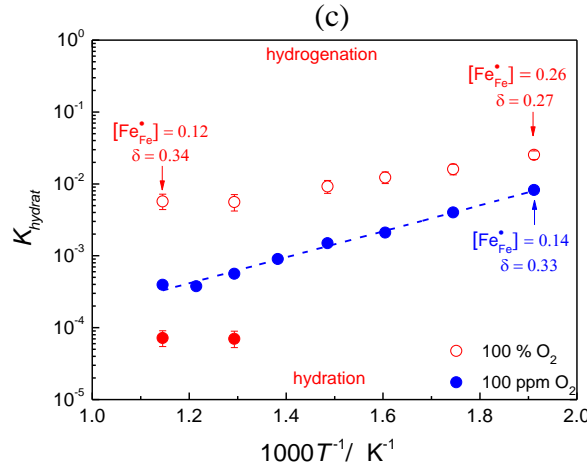


Figure 4-16: BCFZr hydration van 't Hoff plot in 100 ppm and 100% O_2 for oxygen equilibrated BCFZr particles.

BSCF- Oxygen non-stoichiometry in BSCF and the corresponding oxygenation van 't Hoff plot are shown in Figure 4-17. In 100 ppm O_2 , δ is smaller than 0.5 (Fe^{3+} , Co^{3+}) and the oxygenation can be formulated by reaction of Co to Co^{2+} according to



In 100% O_2 , reaction (4.9) at lower T and reaction (4.14) at higher T hold. Non-ideal oxygenation is observed similar to other cathode materials.

The humid TG measurements for BSCF show that it takes up fewer protons compared to BSF, which appears related to presence of Co which increases the covalency of Co–O bonds and decreases the oxide ion basicity. The standard hydration enthalpy and entropy for the equilibrated and quenched samples are $\Delta H_{\text{hydrat}}^{\circ} = -22 \pm 1 \text{ kJmol}^{-1}$, $\Delta S_{\text{hydrat}}^{\circ} = -116 \pm 2 \text{ Jmol}^{-1}\text{K}^{-1}$ and $\Delta H_{\text{hydrat}}^{\circ} = -50 \pm 4 \text{ kJmol}^{-1}$, $\Delta S_{\text{hydrat}}^{\circ} = -151 \pm 6 \text{ Jmol}^{-1}\text{K}^{-1}$, respectively.

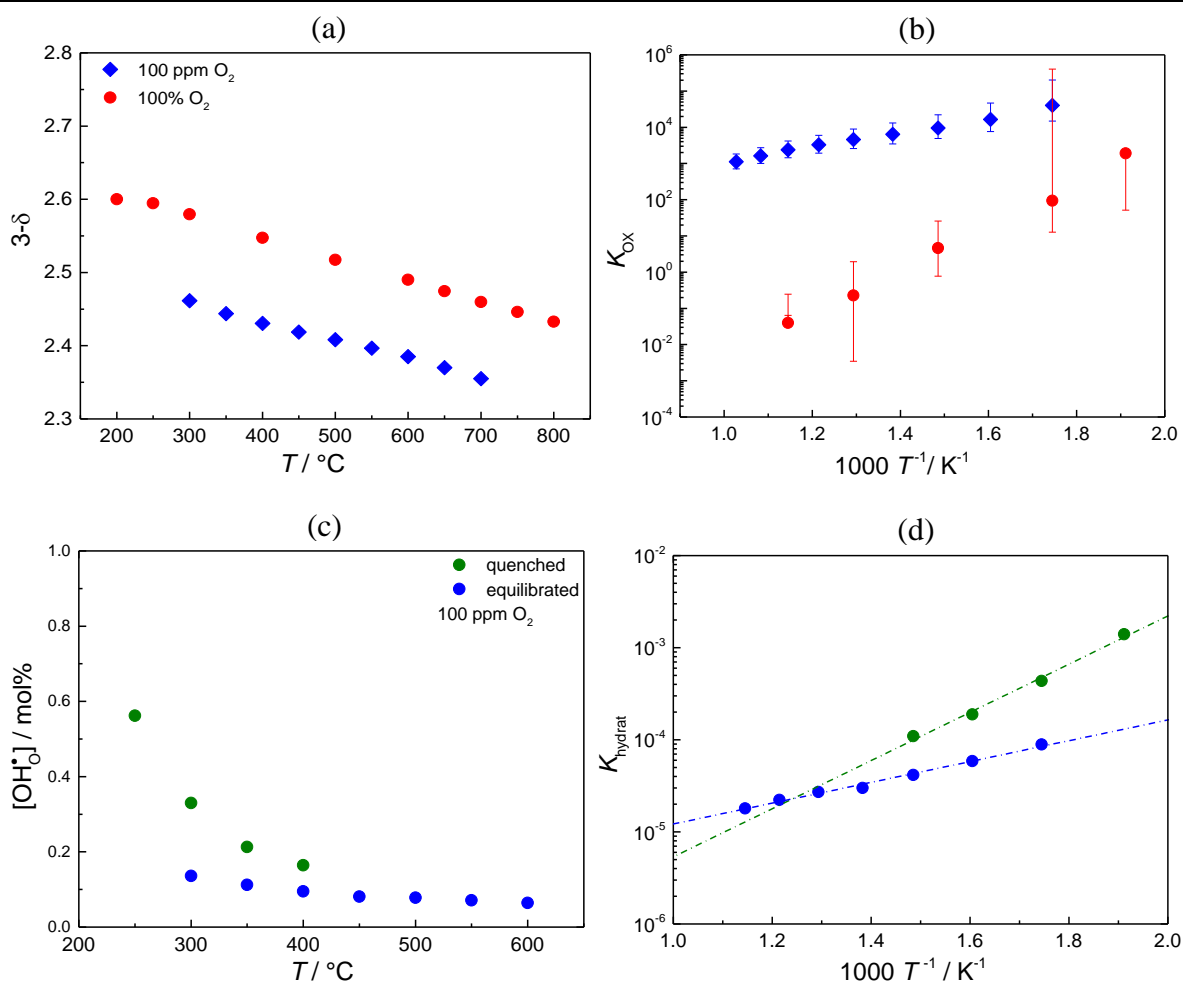


Figure 4-17: TG measurements on BSCF particle (a) oxygen non-stoichiometry in 100 ppm and 100% O_2 (b) and the corresponding nonlinear van 't Hoff plot. (c) Proton concentration for the equilibrated sample and the sample quenched from 800 °C and (d) the corresponding linear van 't Hoff plot.

In humid 100% O_2 , BSCF particles gain 25-160 μg weight in T range of 200-600 °C when p_{H_2O} changes from 6.6 to 15.7 mbar. Considering hydration, this would result in proton concentrations as high as 0.6 mol% at 200 °C which is slightly higher than equilibrated in 100 ppm O_2 .

4.2.3.4 SFZn, BL5FZn20, BSFZn

SFZn- Substitution of 20% of Zn on the B-site of SF prevents formation of oxygen vacancy superstructures and enhances the proton incorporation. This is shown in Figure 4-18. SFZn has high $[V_O^{\bullet\bullet}]$ which approaches 0.6 at high T and low p_{O_2} where all Fe ions are reduced to Fe^{3+} . The oxygenation van 't Hoff plot is also bent. The proton concentration for the equilibrated sample shows similar behavior observed for BSF and the proton concentration decreases at lower T due to proton-hole interaction. The sample was then quenched from 800 °C ($\delta = 0.6$, $[h^{\bullet}] = 0$) in 100 ppm O_2 and the water uptake was measured. The non-stoichiometry was then changed by adding some oxygen until $\Delta\delta = 0.05$ and 0.1 was reached. This shows how proton incorporation is suppressed by increase of hole concentration

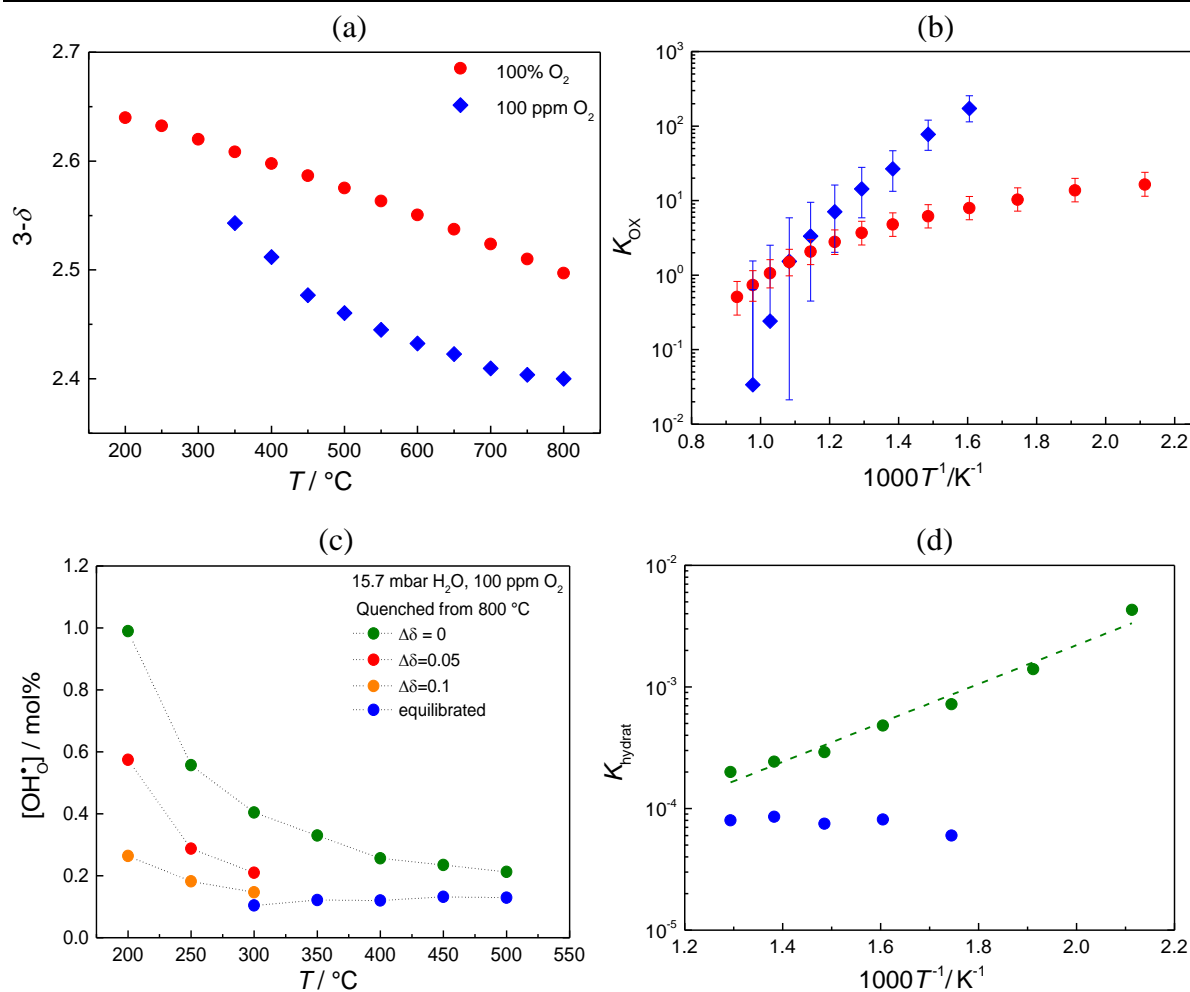


Figure 4-18: TG measurements on SFZn particles. (a) oxygen non-stoichiometry. (b) The non-linear van 't Hoff plot. (c) Proton concentration for the equilibrated sample and the quenched one with $\Delta\delta = 0, 0.05, 0.1$. (d) hydration van 't Hoff plot for the equilibrated and quenched particles.

within the predominant hydration regime. The hydration van 't Hoff plot for the quenched sample is linear resulting in $\Delta H_{\text{hydrat}}^{\circ} = -30 \pm 3 \text{ kJmol}^{-1}$ and $\Delta S_{\text{hydrat}}^{\circ} = -112 \pm 4 \text{ Jmol}^{-1}\text{K}^{-1}$.

BL5FZn20- Partial substitution of Ba on the A-site and Zn on the B-site enhances the proton incorporation in cathode perovskites. BL5FZn20 has a quite high oxygen vacancy concentration which approaches 0.6 at high T and low $p\text{O}_2$. The proton concentration for the particles quenched from 700 °C can approach 10 mol% at 250 °C which is the highest value reported so far for such hole, proton and oxygen vacancy mixed-conducting perovskite. For the quenched sample, $\Delta H_{\text{hydrat}}^{\circ} = -86 \pm 5 \text{ kJmol}^{-1}$ and $\Delta S_{\text{hydrat}}^{\circ} = -143 \pm 6 \text{ Jmol}^{-1}\text{K}^{-1}$ are obtained. The fact that two slopes in hydration van 't Hoff plot is seen in this case suggests that the proton-proton interaction might suppress the proton incorporation in materials with higher proton uptake such as BL5FZn20.

In practice, a PCFC operates under cathodic polarization while it is exposed to relatively high $p\text{O}_2$ ($\sim 20\%$); however in the TG measurements performed in this work, no voltage is applied to the sample which means the oxygen activity in the material is higher than for a PCFC in similar $p\text{O}_2$. To establish an equivalent condition for the investigated samples in TG

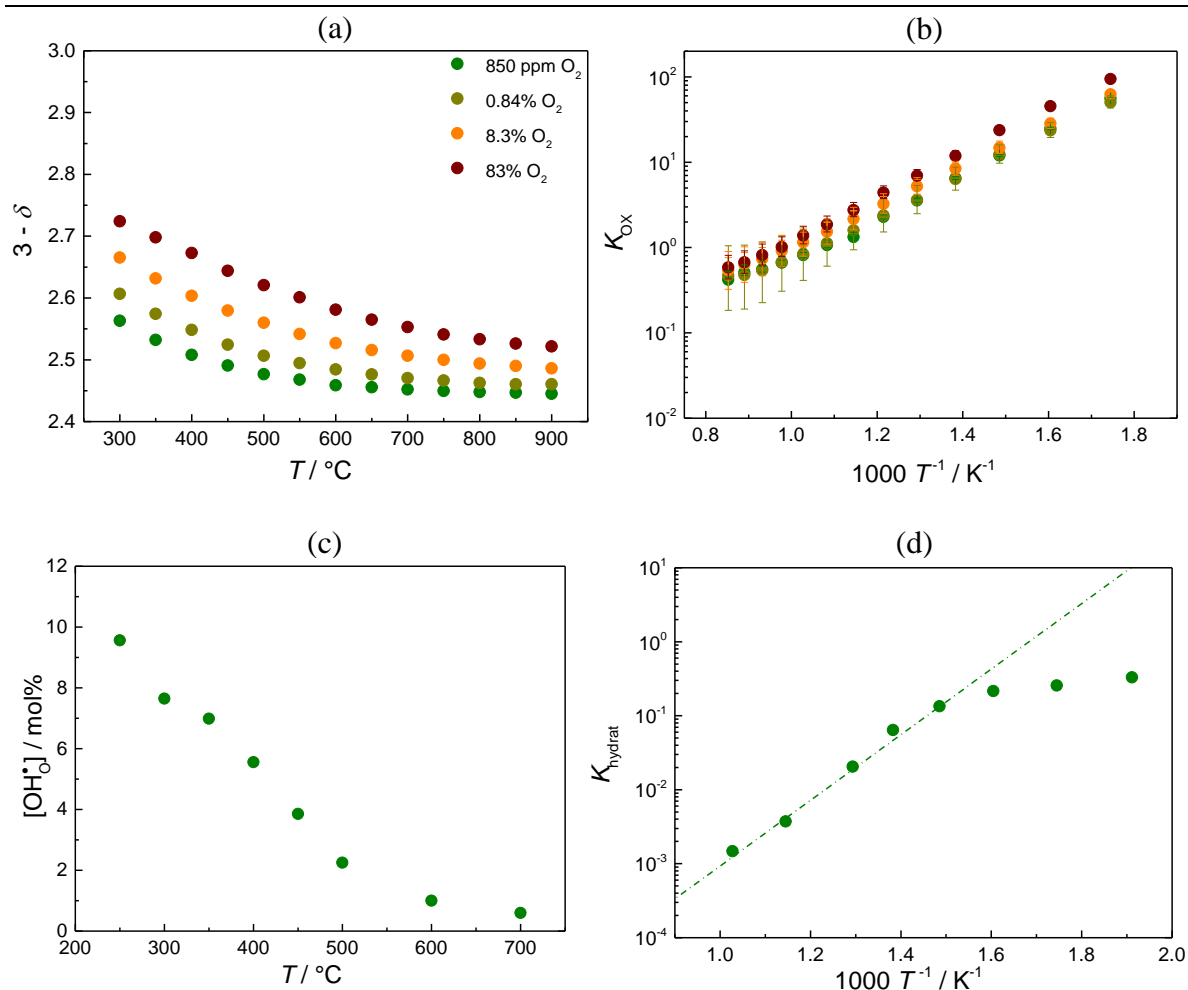


Figure 4-19: (a) Oxygen non-stoichiometry and (b) non-linear oxygenation van 't Hoff plot of BL5FZn20 fine powder. (c) proton uptake for the particles quenched from 700 °C and (d) the corresponding hydration van 't Hoff plot.

as they are exposed to in a practical fuel cell, all measurements are performed in low $p\text{O}_2$ (typically 100 ppm O_2 or N_2) in which oxygen activity decreases substantially. For comparison, the measurements at higher $p\text{O}_2$ are also discussed below for BL5FZn20.

Proton concentration and van 't Hoff plot for the BL5FZn20 sample equilibrated in 0.84% and 8.3% O_2 (close to operational condition of a fuel cell) are shown together with the quenched sample in 100 ppm O_2 in Figure 4-20. The proton concentration decreases from 10% for the quenched sample at 250 °C (green circles) to 5.5%, 2.5%, and 1.2% for the equilibrated sample in 0.84% O_2 , 8.3%, and 83% O_2 , respectively which is still quite high for such oxidizing conditions. The thermodynamic parameters for the equilibrated samples are $\Delta H_{\text{hydrat}}^\circ = -48 \pm 6 \text{ kJmol}^{-1}$, $\Delta S_{\text{hydrat}}^\circ = -107 \pm 11 \text{ Jmol}^{-1}\text{K}^{-1}$ in 0.84% O_2 and $\Delta H_{\text{hydrat}}^\circ = -41 \pm 7 \text{ kJmol}^{-1}$, $\Delta S_{\text{hydrat}}^\circ = -104 \pm 13 \text{ Jmol}^{-1}\text{K}^{-1}$ in 8.3% O_2 . The van 't Hoff curves converge at high T where hole concentration is small and the material is closer to an ideally dilute situation. At lower T , however, the sample behaves non-ideally due to increased concentration of holes which results in smaller hydration enthalpy for the equilibrated sample, hence less proton incorporation.

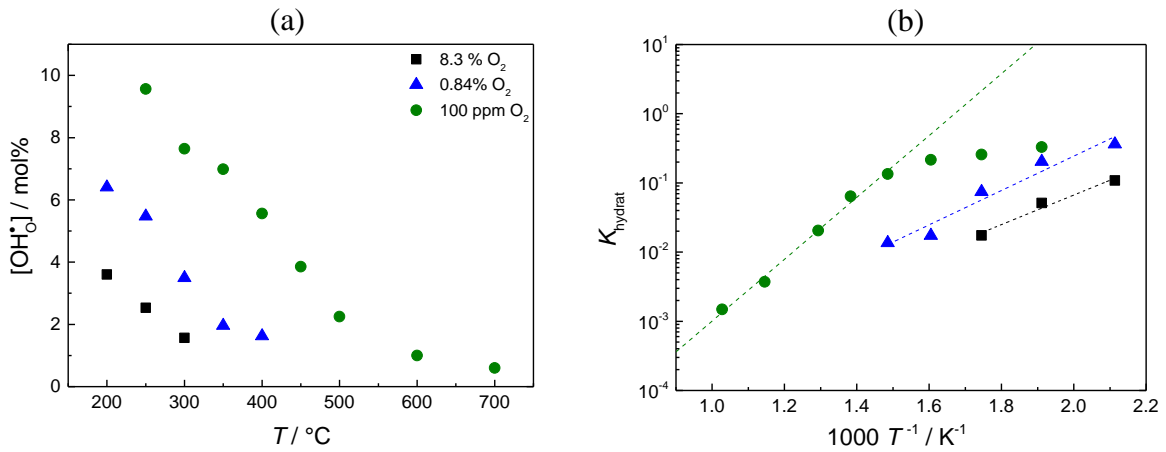


Figure 4-20: (a) Proton concentration for the quenched BL5FZn20 sample in 100 ppm O_2 (green circles), equilibrated sample in 0.84% (blue triangles) and 8.3% O_2 (black squares). (b) The respective hydration van't Hoff plot.

For this material with high proton uptake, the weight changes after a $p\text{H}_2\text{O}$ step show an interesting two-fold behavior. However, owing to the smaller particle size, here the sample is in a surface-reaction controlled regime in contrast to the simulations of section 4.1. This is shown for BL5FZn20 in 8.3% O_2 at 300, 325, and 350 $^\circ\text{C}$ in Figure 4-21 where $p\text{H}_2\text{O}$ is

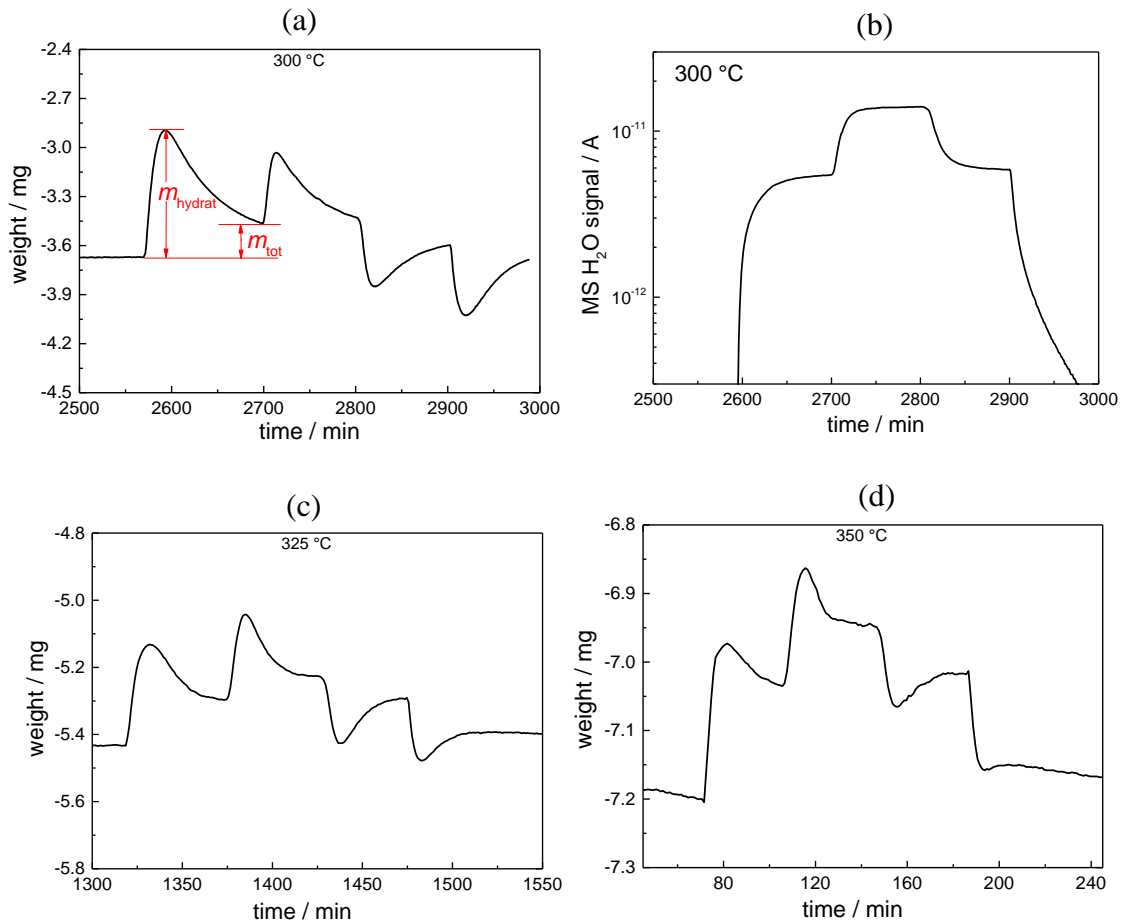


Figure 4-21: TG as a function of time for equilibrated BL5FZn20 sample in 8.3% O_2 at a) 300 $^\circ\text{C}$, in minute 2560 and 2700, $p\text{H}_2\text{O}$ is increased to 7.3 mbar and 16.7 mbar and in minute 2800 and 2920, $p\text{H}_2\text{O}$ decreases back to 7.3 mbar and dry condition. b) Corresponding water signal shown by the mass spectrometer at 300 $^\circ\text{C}$. c) TG at 325 $^\circ\text{C}$ and d) TG at 350 $^\circ\text{C}$.

changed from nominally dry atmosphere to 7.3 and 16.7 mbar H_2O . An example of the corresponding water signal in the mass spectrometer for the measurement at 300 °C is shown in Figure 4-21 (b), evidencing that there is no overshooting in the water supply.

The material is overall in the mixed hydration-hydrogenation reaction regime under this condition. The weight increases upon $p\text{H}_2\text{O}$ change to its maximum value (m_{hydrat}) due to the relatively fast hydration reaction. Then, the weight slowly decreases due to slow oxygen loss. This can be explained by the fact that the large and fast water incorporation decreases $[\text{V}_\text{O}^{\bullet\bullet}]$ below the equilibrium value for the given $p\text{H}_2\text{O}$ and $p\text{O}_2$. Consequently, some oxygen must be removed, and since the oxygen exchange redox reaction is typically slower than the pure acid-base water incorporation reaction, this happens on a slower time scale. A similar two-fold relaxation is seen for decreasing $p\text{H}_2\text{O}$. As T increases, the two fold relaxation becomes less pronounced (m_{tot} increases relative to m_{hydrat}) since the hole concentration decreases; however, the faster kinetics at high T makes it more visible there.

BSFZn- The results of humid TG measurements for particles of BSFZn quenched from 700 °C are shown in Figure 4-22. Partial substitution of Sr on the A-site decreased the proton concentration compared to BL5FZn20. Once more, the flattening of the van 't Hoff plot can be observed at low T corresponding to possible interaction between protons. In this case, $\Delta H_{\text{hydrat}}^\circ = -76 \pm 4 \text{ kJmol}^{-1}$ and $\Delta S_{\text{hydrat}}^\circ = -137 \pm 5 \text{ Jmol}^{-1}\text{K}^{-1}$.

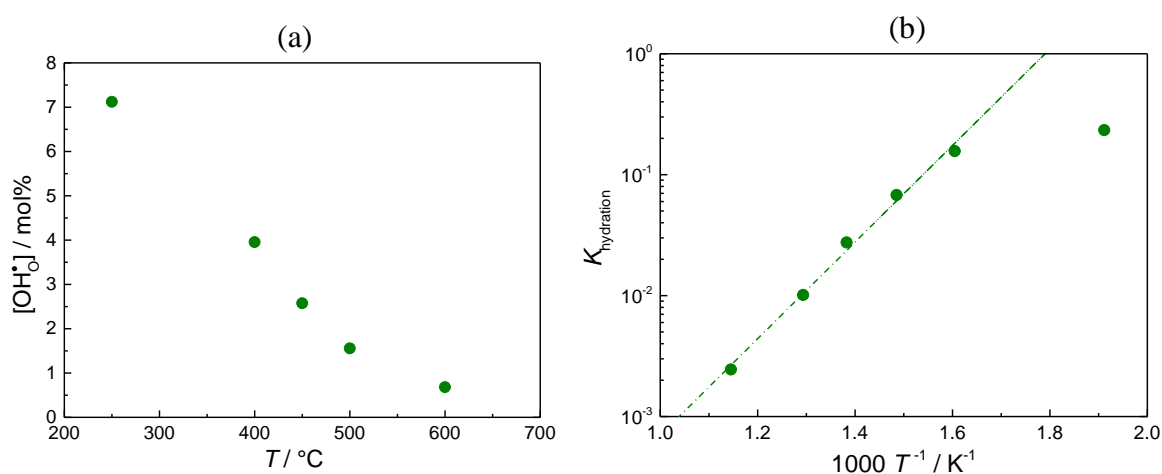


Figure 4-22: (a) BSFZn proton uptake for the particles quenched from 700 °C and (b) the corresponding hydration van 't Hoff plot.

4.2.4 Trends of proton uptake with cation composition

The proton concentration at 250 °C, 100 ppm O₂ and ~ 16 mbar H₂O for particles of various cathode perovskites quenched from high T (where the hole concentration is small) is shown in Figure 4-23. The materials are assumed to be in the predominant hydration regime. Additional compositions including Ba_{0.95}La_{0.05}Fe_{0.95}Zn_{0.05}O_{3- δ} (BL5FZn5), Ba_{0.95}La_{0.05}Fe_{0.9}Zn_{0.1}O_{3- δ} (BL5FZn10), Ba_{0.75}La_{0.25}Fe_{0.8}Zn_{0.2}O_{3- δ} (BL25FZn20), Sr_{0.85}La_{0.15}FeO_{3- δ} (SL15F), Sr_{0.75}La_{0.25}FeO_{3- δ} (SL25F), BaFe_{0.8}Y_{0.2}O_{3- δ} (BFY20), BaCo_{0.8}Y_{0.2}O_{3- δ} (BCY20), and BaCo_{0.4}Fe_{0.4}Zr_{0.1}Y_{0.1}O_{3- δ} (BCFZrY) are also considered in this section [70], [71].

In general, only a few percent of oxygen vacancies are hydrated in the cathode perovskites in contrast to typical electrolyte materials like BZY10 which are fully hydrated below 300 °C [2]. The maximum proton concentration was found for BL5FZn20 with [OH_o[•]] = 10 mol% for the sample quenched to 250 °C, which has an oxygen vacancy concentration of 0.58 per BL5FZn20 formula unit (58%).

In the BLF solid solutions, the proton concentration increases upon higher Ba substitution on the A-site. This is to some degree due to the increase of oxygen vacancy concentration (acceptor dopant increase). However, substitution by more Ba on the A-site increases the oxide ion basicity for two reasons: Firstly, Ba²⁺ is less electronegative compared to La³⁺ and secondly, the proton-hole interaction is weaker due to local lattice distortions related to presence of oxygen vacancies and size mismatch of A and B cations. These two reasons are expected to change the thermodynamics, resulting in a larger mass action constant (more negative standard Gibbs free energy) compared to LaFeO₃. The results suggest that an increase of Ba substitution on the A-site enhances the proton uptake, but a few percent of La is needed to stabilize the cubic perovskite phase.

As mentioned before, the proton concentration in SF is small due to formation of an oxygen vacancy ordered super-structure. Partial substitution of La (SL15F and SL25F) can suppress the formation of vacancy-ordered structures. Relative to SF, the proton concentration increases, but on an absolute scale it remains low. The proton uptake in LSF is even less favorable since the acceptor concentration is small. Furthermore, the system is in hydrogenation regime (high hole concentration even after quenching from 700 °C). The higher electronegativity of La³⁺ compared to Sr²⁺ makes the oxide ion less basic and disfavors the proton uptake. Comparison of SF, BSF, and BL5F emphasizes that a higher Ba to Sr ratio on the A-site enhances the proton uptake due to increased material basicity (Ba²⁺ is less electronegative compared to Sr²⁺).

The beneficial effect of Zn on the B-site can be seen by doping SF, BSF, and BL5F with Zn. Zn acts as acceptor on the B-site and increases the oxygen vacancy concentration. However, the increase of proton uptake is stronger than expected (see Figure 4-20), and this

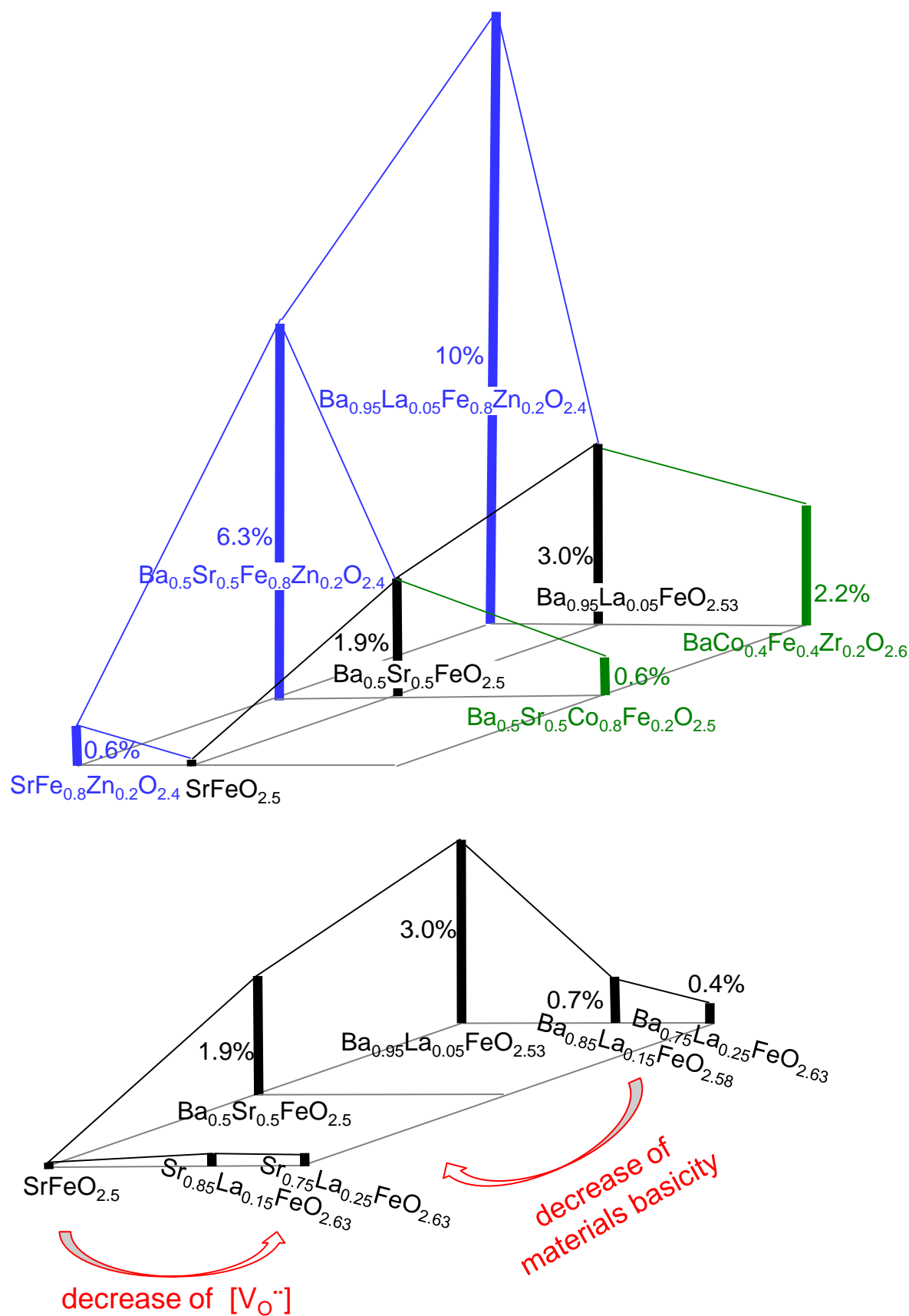


Figure 4-23: Proton concentration of various cathode perovskites at 250 °C, quenched from high T in 100 ppm O_2 (or N_2) and ~16 mbar H_2O . All materials are in the hydration regime.

reveals that the presence of a redox-inactive element with probably local distortions (Zn^{2+} , 0.74 Å, is larger than Fe^{3+} , 0.645 Å) also affects the proton incorporation.

For Co containing cathode perovskites, the proton concentration becomes smaller (compare BSCF with BSF, BCFZr with BL5F) due to stronger Co–O covalency compared to Fe–O covalency and the respectively less basic oxide ions.

The thermodynamic parameters for hydration of the studied cathode materials together with BZY10 and BCY10 as typical electrolyte materials are summarized in Table 4-1. The

Table 4-1: Summary of proton concentration and hydration thermodynamic parameters for different cathode materials determined from the respective van 't Hoff plots, and of BZY10 and BCY10 as typical electrolyte materials (data from ref. [2]). The last column gives the degree of hydration, $[\text{V}_\text{O}^{\bullet\bullet}]_\text{max}$ refers to the maximum possible vacancy concentration in dry conditions. The error bars for $\Delta G_\text{hydrat}^\circ$ are calculated considering the standard deviation of the van 't Hoff plot from the linear regression line.

Material	$\Delta H_\text{hydrat}^\circ /$ kJ mol ⁻¹	$\Delta S_\text{hydrat}^\circ /$ J mol ⁻¹ K ⁻¹	$\Delta G_\text{hydrat}^\circ(700 \text{ K}) /$ kJ mol ⁻¹	$[\text{OH}_\text{O}^\bullet] /$ mol% (250 °C, 16 mbar H ₂ O)	$[\text{OH}_\text{O}^\bullet] / 2[\text{V}_\text{O}^{\bullet\bullet}]_\text{max}$ (250 °C, 16 mbar H ₂ O)
BZY10	-80	-89	-18	10	1
BCY10	-163	-168	-45	10	1
BL5FZn20	-86 ± 5	-143 ± 6	14 ± 2	10	0.088
BL5FZn10**	-53 ± 6	-109 ± 10	23 ± 3	7.9	0.072
BSFZn20	-76 ± 4	-137 ± 5	20 ± 2	6.3	0.053
BFY20**	-71 ± 2	-142 ± 3	29 ± 1	5.3	0.053
BL5FZn5**	-47 ± 5	-106 ± 8	27 ± 1	5.1	0.051
BL5F	-62 ± 3	-144 ± 5	39 ± 3	3.0	0.034
BCFZr	-56 ± 7	-137 ± 12	40 ± 4	2.2	0.028
BCFZrY**	-62 ± 2	-149 ± 2	42 ± 1	2.2	0.024
BSF	-61 ± 3	-150 ± 5	44 ± 2	1.9	0.019
BL25FZn20**	-61 ± 4	-150 ± 6	44 ± 1	1.7	0.018
BCY20**	-50 ± 3	-133 ± 4	43 ± 1	1.5	0.015
BL15F	-60 ± 2	-160 ± 2	52 ± 1	0.7	0.008
BSCF	-50 ± 4	-151 ± 6	56 ± 1	0.6	0.006
SFZn20	-30 ± 3	-112 ± 4	48 ± 2	0.6	0.005
BL25F	-44 ± 4	-143 ± 7	56 ± 2	0.4	0.005
SL15F**	-39 ± 3	-151 ± 5	67 ± 2	0.15	0.003*
SL25F**	-37 ± 2	-143 ± 4	63 ± 1	0.26	0.004
SF	-	-	-	≤0.02	-

* After TG measurements, XRD for SL15F contained reflections of an orthorhombic phase.

** Data are measured by Giulia Raimondi [71].

results indicate that the cathode materials have typically less negative $\Delta H_{\text{hydrat}}^{\circ}$ and more negative $\Delta S_{\text{hydrat}}^{\circ}$ compared to the electrolytes resulting in typically more positive $\Delta G_{\text{hydrat}}^{\circ}$, hence, a lower degree of hydration. Comparing BL5FZn20 ($[V_{\text{O}}^{\bullet\bullet}] = 0.58$ for the quenched sample) with BZY10 ($[V_{\text{O}}^{\bullet\bullet}] = 0.05$) both with 10% of proton concentration emphasizes that the degree of hydration for the cathode materials (less than 10% of oxygen vacancies are hydrated) is much smaller than for electrolytes which are fully hydrated in humid condition. This means that for cathode perovskites other quantities than $[V_{\text{O}}^{\bullet\bullet}]$ are decisive, in particular the oxide ion intrinsic basicity is the main limiting factor for proton incorporation. The values found for $\Delta S_{\text{hydrat}}^{\circ}$ is reasonable; its expected upper bound is the entropy of the gas phase water molecule ($190 \text{ Jmol}^{-1}\text{K}^{-1}$) which loses the translational and rotational degrees of freedom upon incorporation. The comparison of BZY and BCY shows that $\Delta S_{\text{hydrat}}^{\circ}$ also has a contribution from the entropy of the hydrated lattice, which makes $\Delta S_{\text{hydrat}}^{\circ}$ less negative for BZY with an almost undistorted cubic lattice in contrast to BCY with strongly orthorhombically distorted structure. While for BCY the very negative $\Delta S_{\text{hydrat}}^{\circ}$ is compensated by also strongly negative $\Delta H_{\text{hydrat}}^{\circ}$ leading to an overall negative $\Delta G_{\text{hydrat}}^{\circ}$, this is not the case for the cathode materials. Further studies, e.g., phonon calculations, are required to shed more light into this entropy contribution for the cathode perovskites.

Figure 4-24 shows how $\Delta G_{\text{hydrat}}^{\circ}$ at 700 K changes as a function of La and Zn content for some of the studied cathode materials. The beneficial effect of Zn can be clearly observed (solid red lines). Also, partial substitution of Ba^{2+} with La^{3+} on the A-site strongly decreases the proton incorporation beyond the slight decrease of oxygen vacancy concentration (dashed red lines). One can also notice that a complete absence of Ba^{2+} on the A-site in the $(\text{Sr},\text{La})(\text{Fe},\text{Zn})\text{O}_{3-\delta}$ perovskites strongly disfavors the proton uptake, even when an oxygen vacancy ordered super-structure is not formed.

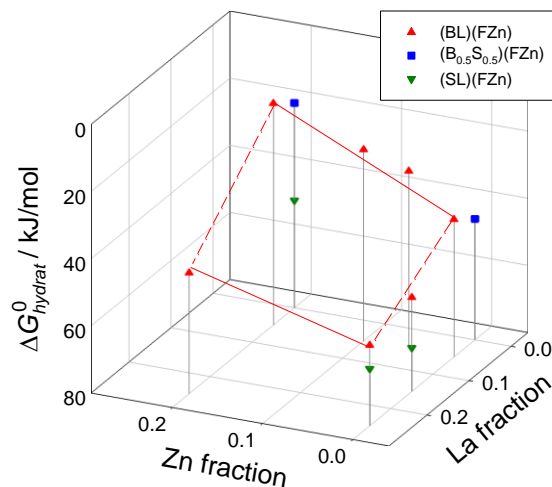


Figure 4-24: Standard Gibbs free energy of hydration at 700 K as a function of Zn and La substitution on the A- and B-site.

In order to place the proton concentrations obtained in this work into larger context, Figure 4-25 shows a collection of data ranging from typical electrolyte materials such as acceptor doped BaZrO₃ and BaCeO₃ to cathode perovskites with predominantly redox active transition metals Fe and Co on the B-site. As a measure of proton uptake, $\Delta G_{\text{hydrat}}^{\circ}$ at typical temperature of 700 K is chosen. For proton conducting electrolytes, a higher basicity of the oxide ions was found to lead to a more negative $\Delta G_{\text{hydrat}}^{\circ}$ which describes the trends of decreasing proton uptake from BaCeO₃ via BaZrO₃ to SrZrO₃ and SrTiO₃ [72]. The basicity of the oxide ions is expected to depend on the electronegativity of the cations on the A- and B-site of the perovskite.

In the first attempt, the change of $\Delta G_{\text{hydrat}}^{\circ}$ with Pauling electronegativity averaged over the elements on the A- and B-site of the perovskite is considered (Figure 4-25 (a)). This shows a separation (see dashed line) of the data into electrolyte materials (red circles) with typically negative $\Delta G_{\text{hydrat}}^{\circ}$, high proton concentration and low average electronegativity; and cathode perovskites with positive $\Delta G_{\text{hydrat}}^{\circ}$, low proton concentration and larger electronegativity. Another interesting feature is that perovskites with 4+ B cations such as BaZrO_{3- δ} follow a correlation line which is different from perovskites with (mainly) 3+ B cations ((A²⁺, A'³⁺)B³⁺O_{3- δ} such as La_{0.9}Sr_{0.1}ScO_{3- δ} and BSF). This suggests that the Pauling electronegativity is not the only determining parameter for proton uptake.

Although the plot of $\Delta G_{\text{hydrat}}^{\circ}$ versus Pauling electronegativity leads to some interesting conclusions, one should keep in mind that the Pauling values refer to the electronegativity of neutral atoms. However, this work mainly deals with largely ionic solids and therefore the effect of polarizing nature of the cations on the basicity of the oxide ion is of more relevance. Therefore, the ‘‘ion electronegativity’’ $\lambda_{\text{ion}} = z_{\text{ion}} / r_{\text{ion}}^2$ is defined inspired by the Allred and Rochow definition of atom electronegativity [73] (which is a measure of the electrostatic force of nucleus on the outer electrons and suggests that $\lambda_{\text{AllRoch}} \propto z_{\text{eff}} / r_{\text{atom}}^2$) to describe the polarizing force of a cation on the neighboring oxide ions. The average of λ_{ion} for A and B cations is calculated from Shannon ionic radii [74] for the respective oxidation state and coordination number. In Figure 4-25 (b), λ_{ion} is chosen as abscissa, and the trend of more favorable proton uptake with lower electronegativity can clearly be observed. Interestingly, the electrolyte-type perovskites without redox inactive B cations (both 2+/4+ and 3+/3+ perovskites) all locate along one correlation line while the cathode perovskites with Fe and Co on the B-site are in another zone with less negative $\Delta G_{\text{hydrat}}^{\circ}$ for the same λ_{ion} . This suggests once more that parameters in addition to λ_{ion} contribute to proton uptake of these perovskites through influencing the oxide ion basicity. One could be the increased covalency of B–O bonds (stronger overlap of transition metal and O orbitals) for later transition metals. This

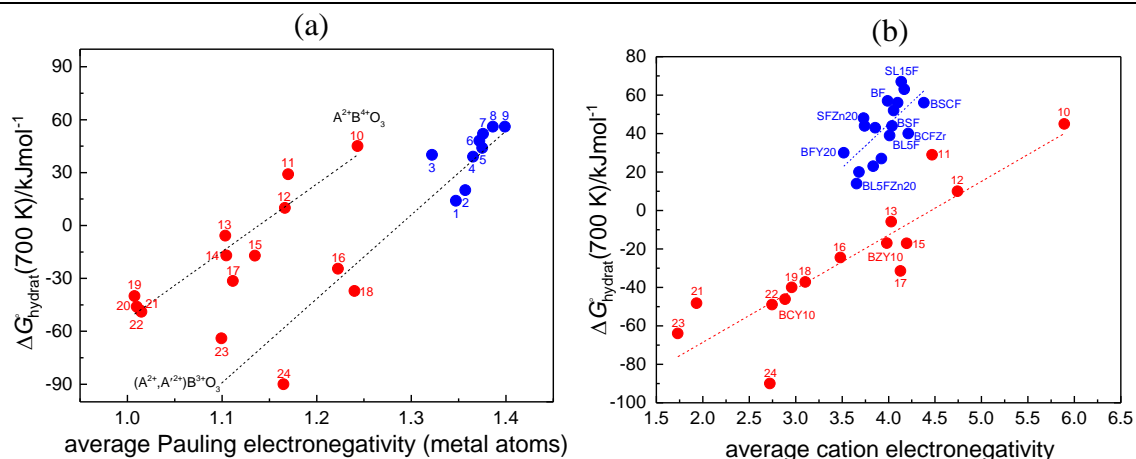


Figure 4-25: Standard Gibbs energy of the hydration reaction ($\Delta G_{\text{hydrat}}^{\circ}$) at 700 K plotted versus (a) average Pauling electronegativity of A- and B-site elements, (b) average “ion electronegativity” (assuming predominant Fe^{3+} and Co^{3+} for the electrode type perovskites) of A- and B-site elements. Blue: cathode perovskites, red: electrolyte-type perovskites. 1 = BL5FZn20 , 2 = BSFZn , 3 = BCFZr , 4 = BL5F , 5 = BSF , 6 = SFZn , 7 = BL15F , 8 = BL25F , 9 = BSCF , 10 = $\text{SrTi}_{0.98}\text{Sc}_{0.02}\text{O}_{3-\delta}$ [75], 11 = $\text{BaTi}_{0.5}\text{Sc}_{0.5}\text{O}_{3-\delta}$ [76], 12 = $\text{CaZr}_{0.9}\text{Sc}_{0.1}\text{O}_{3-\delta}$ [77], 13 = $\text{BaZr}_{0.9}\text{Gd}_{0.1}\text{O}_{3-\delta}$ [75], 14 = $\text{BaZr}_{0.9}\text{Y}_{0.1}\text{O}_{3-\delta}$ [72], 15 = $\text{SrZr}_{0.95}\text{Yb}_{0.05}\text{O}_{3-\delta}$ [78], 16 = $\text{La}_{0.9}\text{Sr}_{0.1}\text{ScO}_{3-\delta}$ [79], 17 = $\text{BaZr}_{0.9}\text{Sc}_{0.1}\text{O}_{3-\delta}$ [72], 18 = $\text{Ba}_2\text{SnY}_2\text{O}_{5.5-\delta}$ [72], 19 = $\text{BaCe}_{0.95}\text{Y}_{0.05}\text{O}_{3-\delta}$, 20 = $\text{BaCe}_{0.9}\text{Y}_{0.1}\text{O}_{3-\delta}$ [72], 21 = $\text{BaPr}_{0.9}\text{Gd}_{0.1}\text{O}_{3-\delta}$ [80], 22 = $\text{BaCe}_{0.8}\text{Y}_{0.2}\text{O}_{3-\delta}$ [72], 23 = $\text{La}_{0.9}\text{Ba}_{0.1}\text{YbO}_{3-\delta}$ [81], 24 = $\text{La}_{0.9}\text{Ca}_{0.1}\text{ErO}_{3-\delta}$ [82].

also contributes to the deviations from the ideally dilute defect model as will be discussed later.

The basicity of the oxide ions is also closely related to the ionicity of the metal-oxygen bonds in the oxide, see e.g. [83]. However, its calculation according to Pauling [84] from element electronegativities occasionally creates nonintuitive results [83]. Furthermore -as already mentioned- element electronegativities are not really appropriate for the largely ionic perovskites (and cannot cover the changes in materials properties caused by variation of the transition metal oxidation state). Therefore, basicity is the preferred quantity for analyzing the trends of proton uptake in the present thesis.

Two more plots of proton uptake versus other properties are shown in Figure 4-26. The first is the proton concentration of cathode perovskites with frozen-in oxygen exchange as a function of maximum oxygen vacancy concentration. The dashed line shows the maximum possible proton concentration when all oxygen vacancies are hydrated ($[\text{OH}_\text{o}^{\bullet}] = 2[\text{V}_\text{o}^{\bullet\bullet}]$). The typical electrolyte materials such as BZY10 and BCY10 are located on this line since at low temperatures they are fully hydrated. Although $[\text{OH}_\text{o}^{\bullet}]$ of the quenched cathode perovskites is far below the maximum proton concentration, there still seems to be a positive correlation as a higher $[\text{V}_\text{o}^{\bullet\bullet}]$ corresponds to a lower average cation charge and thus a tendency of higher oxide ion basicity. Comparing the materials with the same $[\text{V}_\text{o}^{\bullet\bullet}]$ (50% for BF, BSCF, BCY20, BL5FZn5, BFY20, 60% for SFZn20, BSFZn and BL5FZn20) indicates that the proton incorporation in cathode perovskites depends on many other factors such as oxide ion basicity, B–O covalency and crystal structure (local lattice distortions) which as a result might

affect the proton-hole interaction. Also, not all oxygen vacancies are necessarily equivalent when several cations are present on the B-site, in particular when there is large charge and size mismatch.

Figure 4-26 (b) shows the standard Gibbs free energy of hydration at 700 K as a function of Goldschmidt factor, t . Also here no simple overall correlation is apparent. Sr-rich perovskites form a sub-group at lower t because of the smaller radius of Sr compared to Ba. Within this group, a larger t value caused by smaller B-site cations (Fe^{3+} (0.645 Å) and Co^{3+} (0.61 Å)) is related to a less negative $\Delta G_{\text{hydrat}}^{\circ}$ (i.e., less favorable hydration). It is important to note that a number of materials have t values which are significantly higher than 1 and are thus close to the stability limit of the cubic perovskite phase (i.e. might slowly transform into hexagonal perovskites upon extended annealing, cf. [85]). Adding some Zn, Zr, and Y (0.74, 0.72 and 0.9 Å) on the B-site brings t closer to 1 (perfect cubic perovskite) but nevertheless $\Delta G_{\text{hydrat}}^{\circ}$ remains much less negative than for Y-doped BaZrO_3 .

The water uptake from the gas phase can be hypothetically written as (i) $\text{H}_{\text{gas}}^{+} + \text{O}_{\text{O}}^{\times} \rightleftharpoons \text{OH}_{\text{O}}^{\cdot}$ for which oxide ion basicity is beneficial, and (ii) $\text{OH}_{\text{gas}}^{-} + \text{V}_{\text{O}}^{\bullet\bullet} \rightleftharpoons \text{OH}_{\text{O}}^{\cdot}$. A high charge of B cations is expected to be beneficial in the latter reaction corresponding to a larger Madelung potential at the O site and less favorable oxygen vacancy formation. DFT calculations performed by T. S. Bjorheim (university of Oslo) show that the proton affinity ($\text{H}_{\text{gas}}^{+} + \text{O}_{\text{O}}^{\times} \rightleftharpoons \text{OH}_{\text{O}}^{\cdot}$) makes the larger contribution to the total hydration enthalpy than the hydroxide affinity ($\text{OH}_{\text{gas}}^{-} + \text{V}_{\text{O}}^{\bullet\bullet} \rightleftharpoons \text{OH}_{\text{O}}^{\cdot}$). This observation helps to explain why the oxide ion basicity has such an important effect on the hydration thermodynamics. If the hydroxide affinity was the dominant contribution, other parameters such as the Madelung potential might be more important.

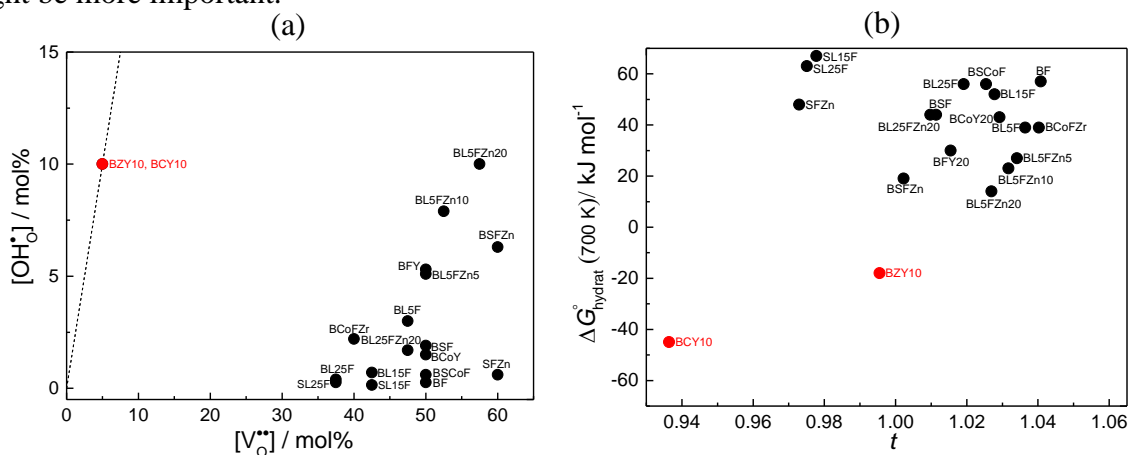


Figure 4-26: Proton concentrations of the quenched sample at 250 °C and 16 mbar H_2O in N_2 plotted versus maximum $[\text{V}_{\text{O}}^{\bullet\bullet}]$ in dry state. The dashed line indicates the maximum possible proton incorporation in case all $\text{V}_{\text{O}}^{\bullet\bullet}$ are hydrated. (b) $\Delta G_{\text{hydrat}}^{\circ}$ at 700 K plotted versus Goldschmidt tolerance factor (t), assuming all iron to be Fe^{3+} .

Figure 4-27 (a) shows the DFT proton affinity versus the average ion electronegativity (Data from T. S. Bjorheim, University of Oslo). A larger average ion electronegativity which leads to decreased oxide ion basicity leads to less negative proton affinity. Figure 4-27 (b) shows how proton affinity (as a measure of oxide ion basicity) changes with ionization potential (work function) of the material. The linear relationship with slope = 1 suggests that ionization potential can also be a measure for evaluation of the oxide ion basicity, and emphasizes the influence of the electronic structure that also shows up in the hole-proton interaction.

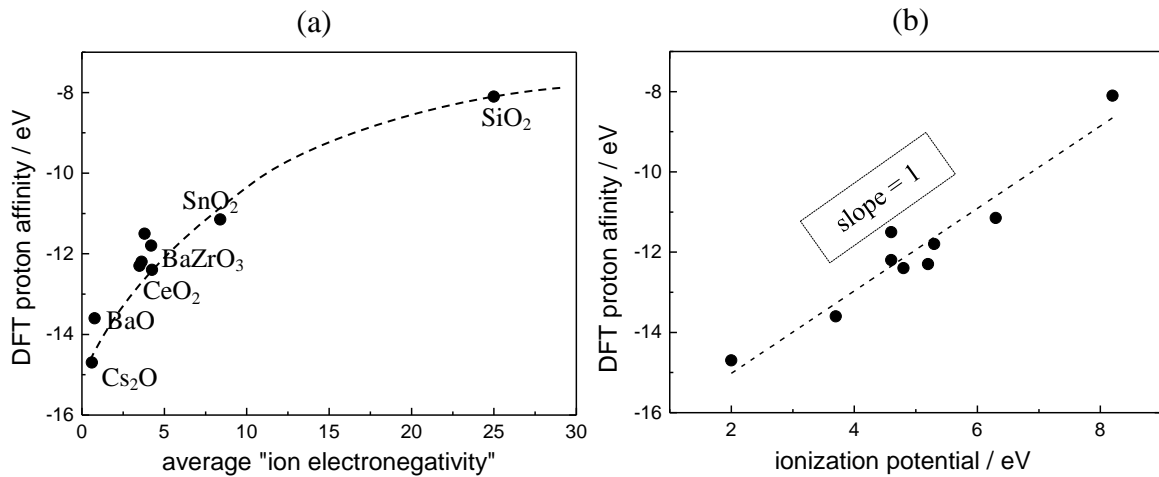


Figure 4-27: DFT proton affinity versus (a) average "ion electronegativity" (b) ionization potential (work function). Data from T. S. Bjorheim, University of Oslo.

4.2.5 Defect interactions and non-ideal behavior

In an ideal solid solution, one expects the thermodynamic parameters (ΔH° and ΔS°) to be independent of T , pO_2 , pH_2O and doping, hence, defect concentrations, and to depend solely on the nature of the material. However, a T dependence of the reaction enthalpy ΔH_R° due to a non-zero reaction heat capacity ($\Delta C_{p,R}$) is possible also in an ideal system. Ab initio calculations for the T -dependence of the oxygen vacancy formation enthalpy in LSF including phonons indicate that the T -dependence of ΔH_{ox}° caused by heat capacity changes amounts to less than 10 kJmol^{-1} between $250 \text{ }^\circ\text{C}$ and $800 \text{ }^\circ\text{C}$ which is negligible [86]. Any deviation from ideal behavior suggests that the distribution of defects is not random and defect interactions exist. In the present thesis, those defect interactions are discussed which are indicated by obvious non-idealities in the measurements: hole-hole, hole-proton and proton-proton interactions.

4.2.5.1 Defect interactions: Qualitative approach

Hole-hole interaction- Considering the oxygenation van 't Hoff plot of cathode materials shown in 4.2.3, it can be seen that the slope (which is related to the reaction enthalpy) becomes less steep at lower T where hole concentration is larger, corresponding to less favorable oxygenation due to hole-hole interaction. This can be equivalently explained by (i) partial delocalization of holes to the oxide ions adjacent to Fe_{Fe}^\bullet (in ferrates) and (ii) change of the Fermi level position by modified charge carrier concentration [87] within a "rigid band model". In the first explanation, owing to partially covalent Fe–O bonds that withdraw electron density from the oxide ion, the six oxide ions in the first coordinate sphere of Fe_{Fe}^\bullet are affected which strongly increases the volume influenced by a single hole, i.e., the holes start to perceive each other already at comparably low concentration. Therefore, further oxygen incorporation becomes less favorable with increasing number of holes. Equivalently, by increase of hole concentration, the Fermi level would move downwards and ΔE_f would lead to a change in ΔH_{ox}° . This change of the Fermi level reflects the fact that - in contrast to dilute semiconductors - the considered mixed conducting perovskites exhibit changes of d-electron concentrations of the transition metal (up to one electron per Fe or Co depending on pO_2 , T change) which are significant relative to the density of states, and thus change the position of the highest occupied state. This point will further be quantified in the next section.

$V_O^{\bullet\bullet}$ - $V_O^{\bullet\bullet}$ interaction is expected to appear at high T or low pO_2 where $[V_O^{\bullet\bullet}]$ is high; however, the slope of the van 't Hoff plot decreases at low T corresponding to low $[V_O^{\bullet\bullet}]$ means that repulsive $V_O^{\bullet\bullet}$ - $V_O^{\bullet\bullet}$ interactions are of minor importance. The interaction between oxygen vacancies and holes is also not relevant as any increase in the concentration of one defect results in a decrease in the other one according to the electroneutrality.

Proton-hole interaction- Since oxide ion basicity is decreased due to partial delocalization of holes, the proton concentration is also suppressed. The holes interact with other defects (protons and holes) by influencing the oxide ions. The proton-hole interaction shows up in the comparison of quenched and oxygen-equilibrated samples. Ideally $[\text{OH}_0^\bullet] \propto \sqrt{[\text{V}_0^{\bullet\bullet}]}$ holds at a certain T and $p\text{O}_2$ in the regime of predominant hydration reaction as long as the degree of hydration is low, i.e., $[\text{V}_0^{\bullet\bullet}]$ is constant. Considering the proton concentration of BCFZr at 250 °C and 100 ppm O_2 for the quenched (from 600 °C, $\delta = 0.4$, $[\text{OH}_0^\bullet] = 2.16$ mol%) and O-equilibrated sample ($\delta = 0.33$, $[\text{OH}_0^\bullet] = 1.16$ mol%) as in Figure 4-15, one expects $[\text{OH}_0^\bullet]$ for the quenched sample to be $\sqrt{0.4/0.33} = 1.1$ times larger than for the equilibrated sample. However, the ratio is larger (a factor of $2.16/1.16 = 1.9$). This indicates that the increased number of holes for the O-equilibrated sample has suppressed the proton incorporation due to decreased oxide ion basicity. This can also explain the small proton concentration in the regime of predominant hydrogenation reaction for samples such as LSF and BL50F which have a perceptible hole concentration even when quenched from 700 °C. This proton-hole interaction is remarkable since holes do not appear in the purely acid-base reaction of water incorporation (of eq. (2.2)). Nevertheless, by modifying the basicity of oxide ions, the holes (electronic structure) affect the protons (ionic defects).

Figure 4-28 shows how $[\text{OH}_0^\bullet]$ for SFZn20 changes with $\sqrt{[\text{V}_0^{\bullet\bullet}]}$ when the oxygen stoichiometry is equilibrated with $p\text{O}_2$ (note that $[\text{O}_0^\times] = (3-\delta)$ in the denominator of mass action constant eq. 4.11 is to good approximation constant). The proton concentration does not scale linearly with the square root of oxygen vacancy concentration and does not pass through the origin as is expected from the hydration reaction (i.e., high $[\text{V}_0^{\bullet\bullet}]$ is required to see proton uptake at all). This confirms that the hydration is not ideal.

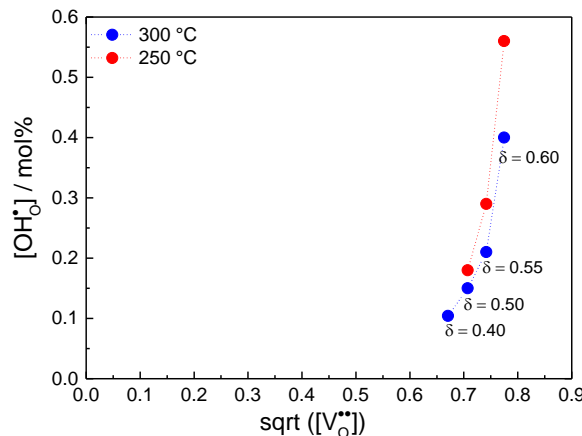


Figure 4-28: Proton concentration in SFZn20 (mol%) for the O-equilibrated sample ($\delta = 0.4$) and the sample quenched from 800 °C ($\delta = 0.6$ and two intermediate O-stoichiometries) versus $\sqrt{[\text{V}_0^{\bullet\bullet}]}$ in 100 ppm O_2 and 250, 300 °C and 15.7 mbar H_2O ; the two latter data points were achieved by inserting O_2 to the quenched sample such that $\Delta\delta = 0.05$ and $\Delta\delta = 0.1$. The proton uptake was measured starting from 6.6 mbar H_2O .

Proton-proton interaction- The linearity of the hydration van 't Hoff plot and the fact that proton concentration scales with square root of water partial pressure (Figure 3-7 (b)) confirms that proton-proton interaction is negligible in cathodes with moderate proton concentration. The exceptions are BL5FZn20 and BSFZn20 with higher proton concentration compared to other cathode materials. As Figure 4-19 shows, the van 't Hoff plot bends at lower T corresponding to higher proton concentration and probably proton-proton interaction.

4.2.5.2 Quantitative Approach: First order correction

Non-ideal behavior has been reported for several of mixed conducting perovskites including $\text{SrCo}_y\text{Fe}_{1-y}\text{O}_{3-\delta}$ [88], $\text{La}_x\text{Sr}_{1-x}\text{Co}_y\text{Fe}_{1-y}\text{O}_{3-\delta}$ [89], $\text{Ba}_x\text{Sr}_{1-x}\text{Co}_y\text{Fe}_{1-y}\text{O}_{3-\delta}$ [61], and $\text{LaSr}_y\text{Co}_{1-y}\text{O}_{3-\delta}$ [90]. In the latter reference, a quantitative method is proposed to describe the non-idealities in LSC. Partial molar enthalpy $\Delta h_{\text{O}} = h_{\text{O}} - h_{\text{O}}^{\circ}$ and partial molar entropy $\Delta s_{\text{O}} = s_{\text{O}} - s_{\text{O}}^{\circ}$ were defined, and it was shown that Δh_{O} in dry $p\text{O}_2$ depends linearly on the oxygen vacancy and equivalently hole concentration while Δs_{O} is almost constant in LSC. A similar approach is taken here to see whether such a “first order correction” (FOC) is applicable for the materials studied. BL15F is chosen for a detailed example of a typical cathode perovskite.

The oxygen chemical potential μ_{O} for a perovskite in dry $p\text{O}_2$ is related to Δh_{O} , Δs_{O} by

$$\mu_{\text{O}} - \mu_{\text{O}}^{\circ} = \frac{RT}{2} \ln(p\text{O}_2 / \text{bar}) = \Delta h_{\text{O}} - T\Delta s_{\text{O}} \quad (4.15)$$

where μ_{O}° is μ_{O} in 1 bar O_2 . $p\text{O}_2$ is the equilibrium partial pressure of the perovskite with oxygen nonstoichiometry δ at temperature T . This can be rearranged to

$$\ln(p\text{O}_2 / \text{bar}) = \frac{2}{R} \left(\frac{\Delta h_{\text{O}}}{T} - \Delta s_{\text{O}} \right) \quad (4.16)$$

Taking the derivative of the equilibrium partial pressure $\ln(p\text{O}_2 / \text{bar})$ for a given δ with respect to $1/T$ yields Δh_{O} :

$$\Delta h_{\text{O}} = \frac{R}{2} \left. \frac{\partial \ln(p\text{O}_2 / \text{bar})}{\partial (1/T)} \right|_{\delta} \quad (4.17)$$

Analogously, Δs_{O} is obtained as

$$\Delta s_{\text{O}} = -\frac{R}{2} \left. \frac{\partial (T \ln(p\text{O}_2 / \text{bar}))}{\partial T} \right|_{\delta} \quad (4.18)$$

Figure 4-29 (a) and (c) shows a plot of $p\text{O}_2$ versus $1000T^{-1}$ and $RT \ln(p\text{O}_2)$ versus T at constant δ values for BL15F in dry $p\text{O}_2$. Both plots yield straight lines which means Δh_{O} and Δs_{O} are independent of T . The variation of Δh_{O} versus hole concentration is shown in Figure 4-29 (b)

and (d). Δh_o changes linearly with $[\text{Fe}_{\text{Fe}}^\bullet]$ and therefore, the first order correction is applicable for BL15F. Since Δh_o describes the enthalpy change of the perovskite upon inserting oxygen into the material it corresponds to the enthalpy of oxidation ΔH_{OX} , and one can write

$$\Delta H_{\text{OX}} = H_{\text{OX}} - H_{\text{OX}}^\circ = \Delta H_{\text{OX}}^\circ + a[\text{Fe}_{\text{Fe}}^\bullet] \quad (4.19)$$

where a is the oxygenation interaction parameter. The linear dependence of ΔH_{OX} on hole concentration is related to the change of Fermi level with electron concentration [87] as described in the previous section.

The change in oxide ion concentration in the oxygenation reaction is equivalent to the change of oxygen vacancy concentration and proportional to the change of hole concentration (or average valence state of Fe). Therefore, the configurational entropy of the change in oxygen vacancy concentration and change of electronic state of Fe will also contribute to the oxygenation partial molar entropy. The former can be simplified and rewritten as

$$s_o(\text{conf}) = R \ln\left(\frac{\delta}{3-\delta}\right) \quad (4.20)$$

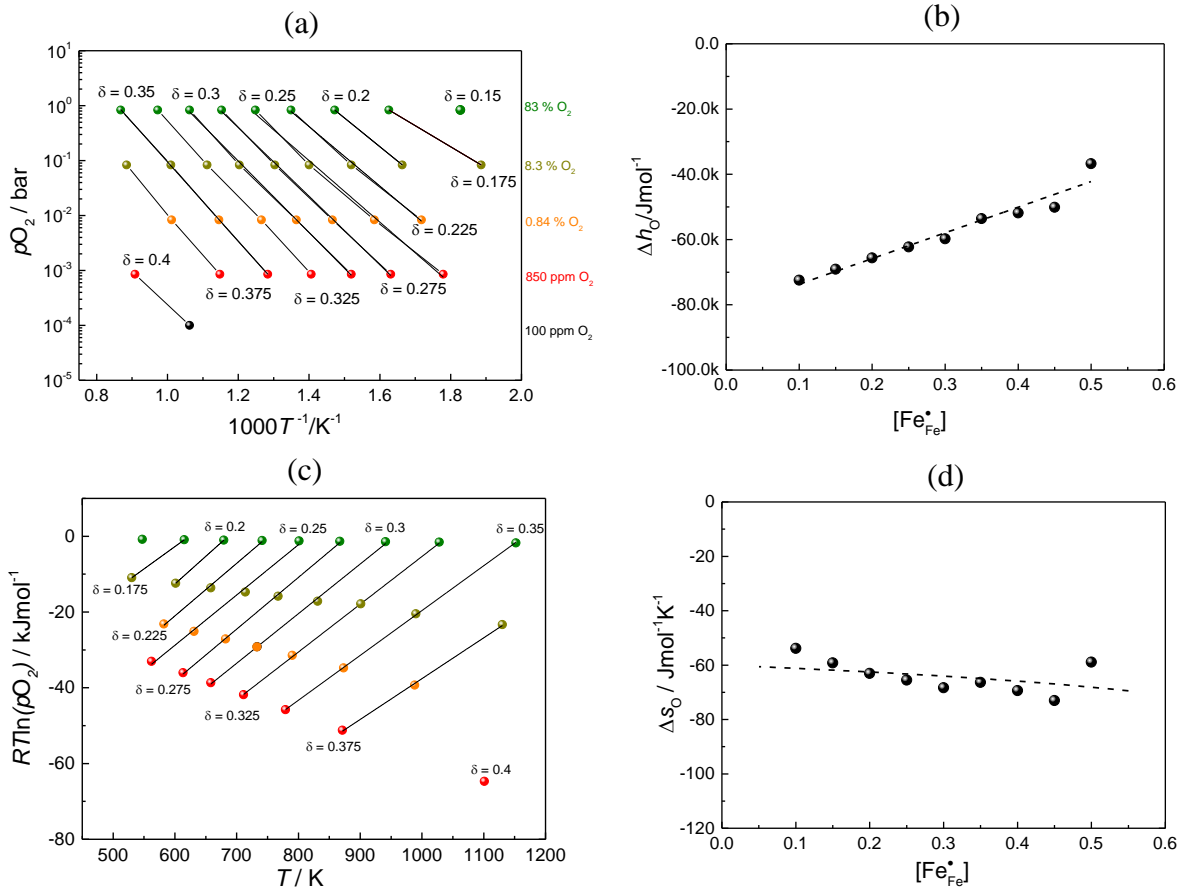


Figure 4-29: BL15F in dry 100 ppm, 850 ppm, 0.84%, 8.3% and 83% $p\text{O}_2$. (a) $p\text{O}_2$ versus $1000T^{-1}/\text{K}^{-1}$ at constant δ . (b) partial molar enthalpy versus hole concentration. (c) $R T \ln(p\text{O}_2)$ versus T at constant δ . (d) partial molar entropy versus hole concentration (fitting when $s_o(\text{elec}) \approx 0$).

The electronic contribution to $s_o(\text{conf})$ has been found to be negligible for LSC due to its metallic or semi-metallic characteristic. However, it might be non-negligible for BL15F since it has a lower hole conductivity. Δs_o can therefore be written as

$$s_o - s_o^\circ = \Delta s_o^\circ + s_o(\text{conf}) + s_o(\text{elec}) \approx \Delta s_o^\circ + R \ln\left(\frac{\delta}{3-\delta}\right) \quad (4.21)$$

Figure 4-29 (d) shows the variation of Δs_o with $[\text{Fe}_{\text{Fe}}^\bullet]$ and the corresponding fitting with eq. (4.21). Since the slope from $R \ln(\delta/(3-\delta))$ largely describes the data, $s_o(\text{elec})$ and an excess entropy contribution from defect interactions can be neglected in first approximation. This, one can regard all non-idealities as a result of change in enthalpy, and FOC can be applied for oxygenation and hydration reaction as follows.

Oxygenation – The ideal mass action for the oxygenation reaction can be written as

$$K_{\text{OX}}^{\text{ideal}} = e^{-\frac{\Delta H_{\text{OX}}^\circ - T\Delta S_{\text{OX}}^\circ}{RT}} \quad (4.22)$$

Considering the first order correction, the apparent concentration action constant (K_{OX}) is

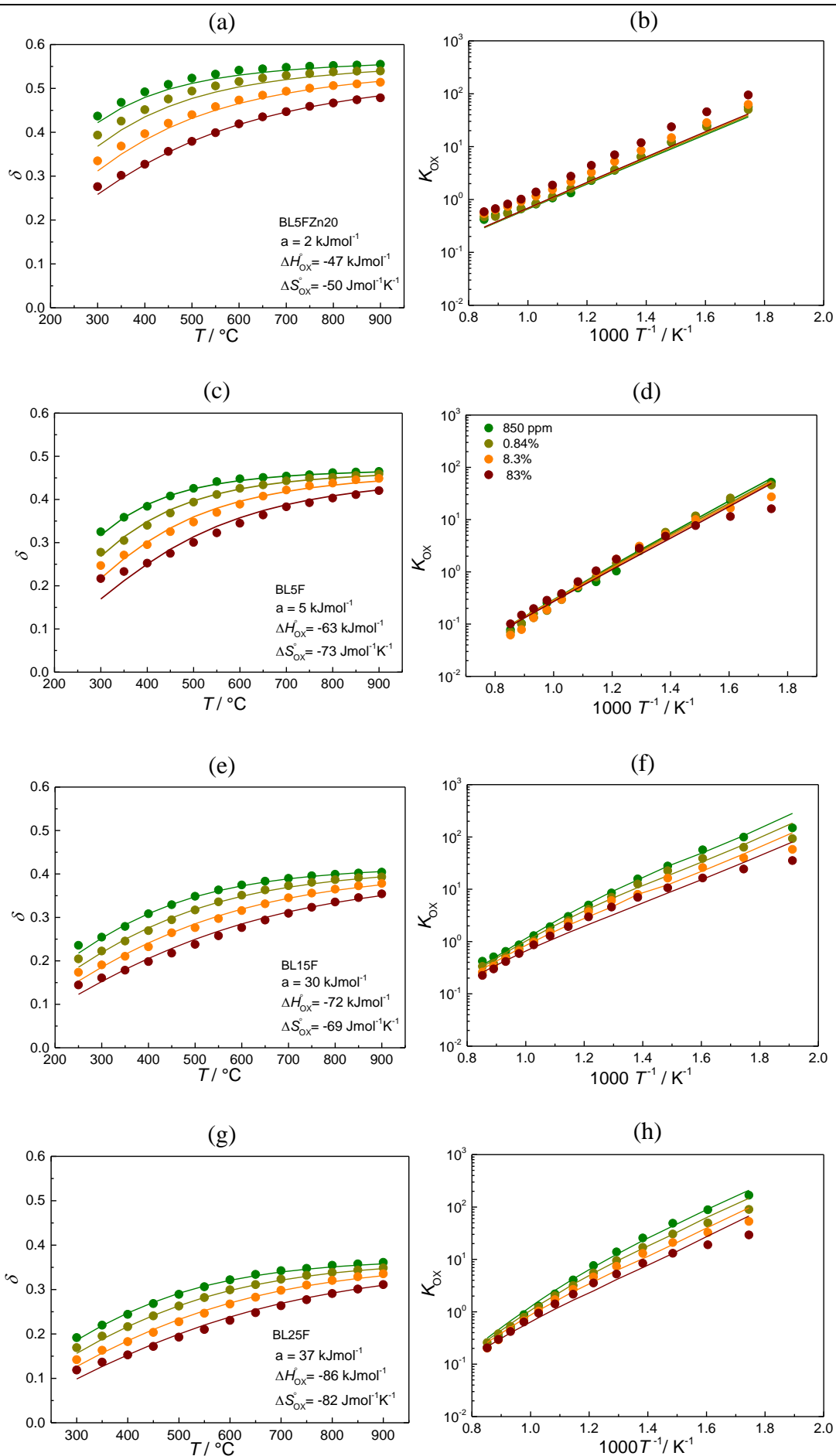
$$K_{\text{OX}} = \frac{[\text{O}_\text{O}^\times][\text{Fe}_{\text{Fe}}^\bullet]^2}{\sqrt{p\text{O}_2}[\text{V}_\text{O}^{\bullet\bullet}][\text{Fe}_{\text{Fe}}^\times]^2} = K_{\text{OX}}^{\text{ideal}} e^{-\frac{a[\text{Fe}_{\text{Fe}}^\bullet]}{RT}} \quad (4.23)$$

Since $\delta-T$ and oxygenation van 't Hoff plot are known from dry TG measurements for several materials, it is possible to apply the FOC and determine a , $\Delta H_{\text{O}}^\circ$, and $\Delta S_{\text{O}}^\circ$ as fitting parameters. This has been done for BL5FZn20, BL5F, BL15F, BL25F, BL50F, and BSF. The results are summarized in Table 4-2 and shown in Figure 4-30. The fitting parameters are found minimizing the standard deviation from the regression line in $\delta-T$ and van 't Hoff plot at the same time. This results in error bars of less than 5 units for the fitting parameters.

Comparing the results for BL5F and BL5FZn20, the interaction parameter has decreased from 5 to 2 kJmol^{-1} . Apparently, Zn (as a cation with completely filled d-orbitals) suppresses the electronic delocalization in the material, and the increased oxygen vacancy concentration may further enhance that effect. The results for BLF series suggest that a depends on La

Table 4-2: Fitting parameters a (oxygenation interaction parameter), $\Delta H_{\text{ox}}^\circ$ and $\Delta S_{\text{ox}}^\circ$ for different materials. The error bars are less than 5 units for each of fitting parameters.

Material	a / kJmol^{-1}	$\Delta H_{\text{OX}}^\circ / \text{kJmol}^{-1}$	$\Delta S_{\text{OX}}^\circ / \text{Jmol}^{-1}\text{K}^{-1}$
BL5FZn20	2	-47	-50
BL5F	5	-63	-73
BL15F	30	-72	-69
BL25F	37	-86	-82
BL50F	34	-88	-55
BSF	23	-84	-78



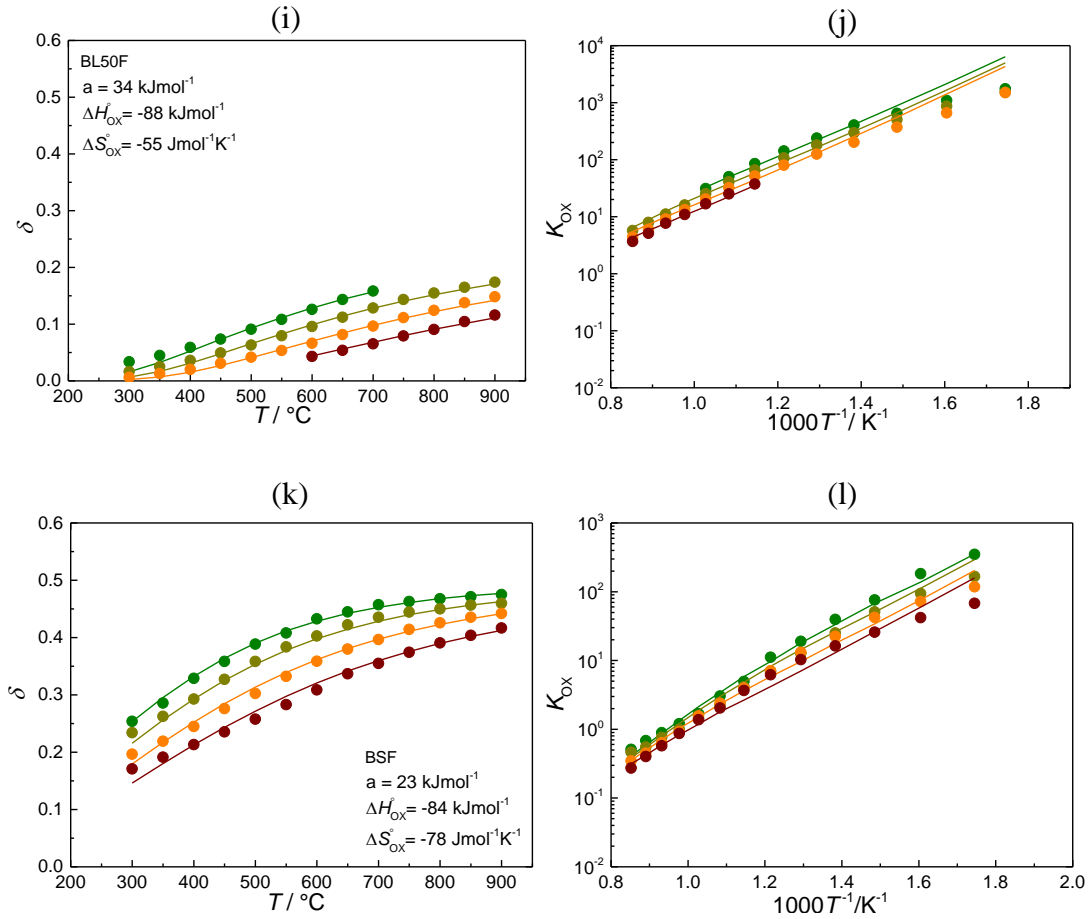


Figure 4-30: Fitting FOC with δ -T (left) and oxygenation van 't Hoff plot (right) for (a), (b) BL5FZn20, (c), (d) BL5F, (e),(f) BL15F, (g),(h) BL25F, (i),(j) BL50F, (k), (l) BSF.

substitution on the A-site. A larger La content decreases the $[V_O^{\bullet\bullet}]$ and thereby local lattice distortions that tend to weaken the electronic delocalization.

Hydration- It is also possible to apply a first order correction to quantify the proton-hole interaction in the hydration reaction. One can assume that the hydration enthalpy changes linearly with hole concentration when proton concentration is relatively low (no proton-proton interaction),

$$\Delta H_{\text{hydrat}} = \Delta H_{\text{hydrat}}^{\circ} + b[\text{Fe}_{\text{Fe}}^{\bullet}] \quad (4.24)$$

where b is the hydration interaction parameter. The corresponding hydration mass action law is then,

$$K_{\text{hydrat}} = \frac{[\text{OH}_O^{\bullet}]^2}{p\text{H}_2\text{O}[\text{V}_O^{\bullet\bullet}][\text{O}_O^{\times}]} = K_{\text{hydrat}}^{\text{ideal}} e^{\frac{-b[\text{Fe}_{\text{Fe}}^{\bullet}]}{RT}} \quad (4.25)$$

Fitting the proton concentration profile and the van 't Hoff plot with the help of these equations, b , $\Delta H_{\text{hydrat}}^{\circ}$, and $\Delta S_{\text{hydrat}}^{\circ}$ can be obtained as fitting parameters. Since measuring oxygen non-stoichiometry at low T (200, 250 °C) and $p\text{O}_2$ (100 ppm O_2) is challenging, the data are estimated by extrapolation of measured data at higher $p\text{O}_2$ ($\delta \propto p\text{O}_2^{-n}$). The results are shown for BL15F and BL5F in Figure 4-31. The uncertainty in δ , also in the measurement of

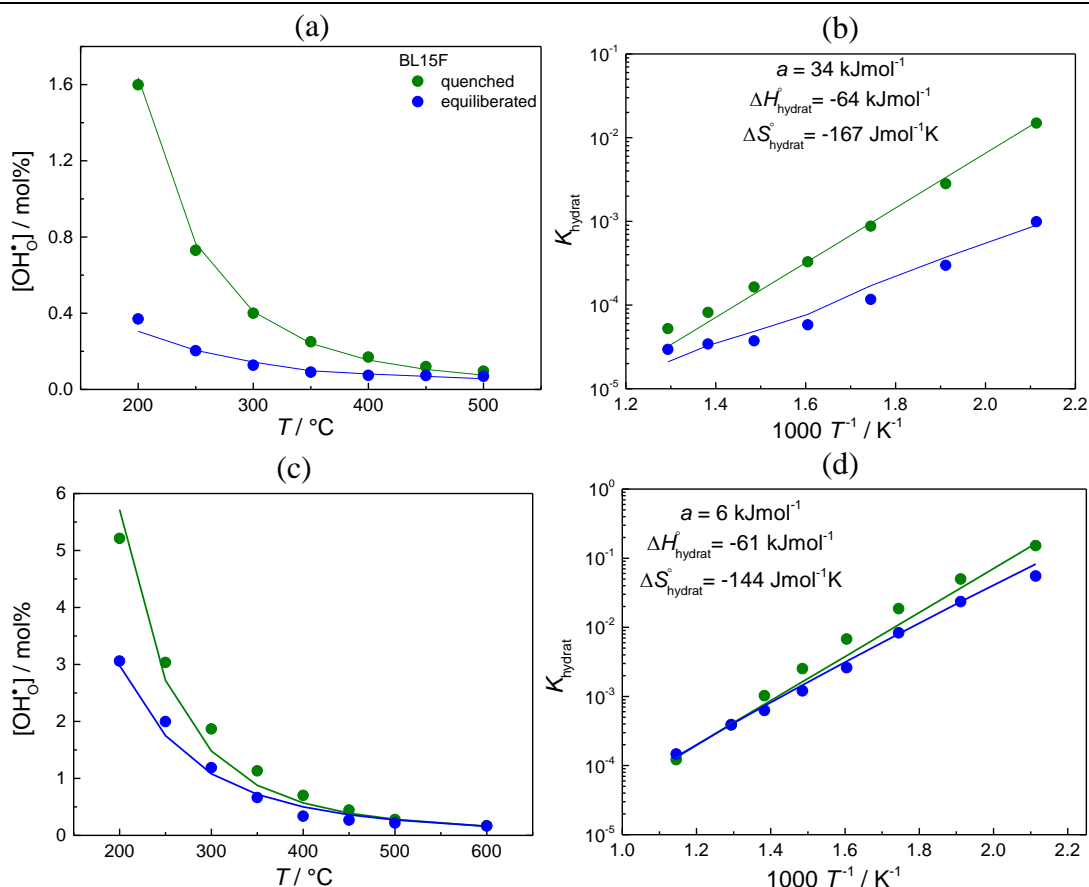


Figure 4-31: Fitting FOC with $[\text{OH}_\text{O}^\bullet]$ proton- T (left) and hydration van 't Hoff plot (right) for (a), (b) BL15F, (c), (d) BL5F.

proton uptake result in error bar of less than 5 units for the fitting parameters. The hydration interaction parameter, b for BL5F and BL15F is 34 and 6 kJmol^{-1} , respectively.

An interesting observation is that the oxygenation and hydration interaction parameters show the same trend with increasing La content, and even the absolute values are quite similar (within the error bars). This is qualitatively understandable as the non-ideality in both cases originates from the oxide ion being affected by holes, which would further influence oxygenation and hydration reaction, hence proton and hole concentration. Furthermore, rough calculations show that this approach is capable of describing the decrease of proton concentration at low T in equilibrium for samples such as BSF (of Figure 4-11 (d)).

4.2.6 Electronic conductivity measurements

For a number of cathode materials including BL5FZn20, BFY20, and BCY20, electronic conductivity was measured on sintered pellets or rods with sputtered Pt electrodes by impedance spectroscopy using pseudo-four-point contacting (current and voltage line meeting at the Pt foil electrode which is pressed against the sputtered Pt film). Figure 4-32 shows T (20% O_2) and $p\text{O}_2$ dependence (600 $^\circ\text{C}$) of electronic conductivity for BL5FZn20 as an example. At lower T where oxygen vacancies are frozen, the T -dependence curve can be described by Arrhenius plot and gives the activation energy (migration barrier) of 0.25 eV in

20% O₂. The Brouwer diagram gives a slope of 0.25 at 600 °C. The hole conductivity of BL5FZn20 at 600 °C and in 20% O₂ is 1.16 Scm⁻¹ which is comparable with that of BCFZrY, which is a cathode with promising performance [1]. The hole conductivity for BFY20 and BCY20 in similar condition is 0.76 and 1.6 Scm⁻¹, respectively. Considering the Goldschmidt tolerance factor (*t*) for these perovskite (1.016 for BFY20, 1.027 for BL5FZn20 and 1.0292 for BCY20), one recognizes that the closer is *t* to unity characterizing a perfect cubic perovskite, the higher is the electronic conductivity. This can be explained by better overlap of transition metal d-orbital and oxygen p-orbital which facilitates the transport of electronic charge carriers. However, the higher mobility of electron holes in Co-containing materials (more covalency of Co–O compared to Fe–O) would result in a higher electronic conductivity for BCY20 compared to the two other materials.

The variation of standard Gibbs energy of hydration as a function of electronic conductivity is shown in Figure 4-33. A number of electronic conductivity values are taken from literature (if necessary, interpolated between neighboring materials compositions). There

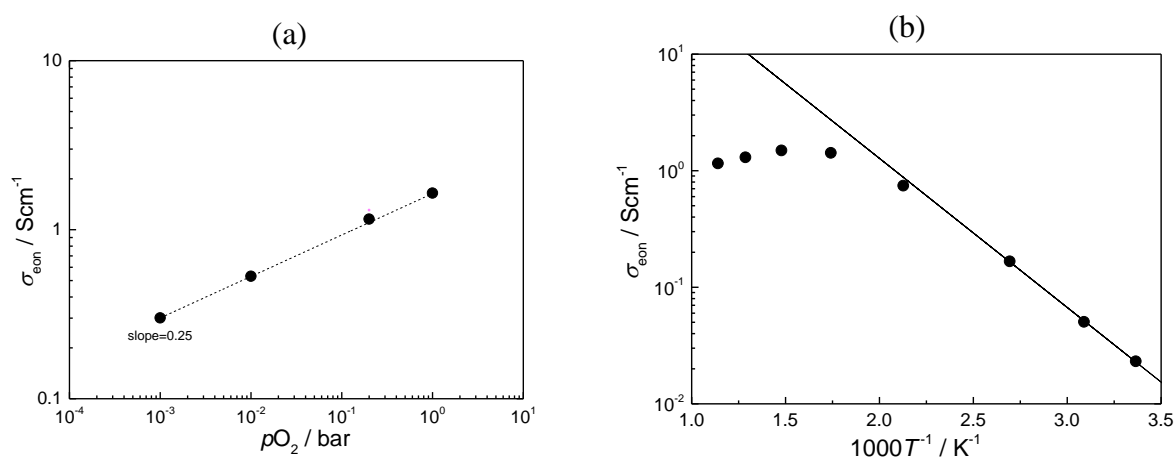


Figure 4-32: (a) Total (= hole) conductivity of BL5FZn20 in 20% O₂. (b) $p\text{O}_2$ dependence measured at 600 °C.

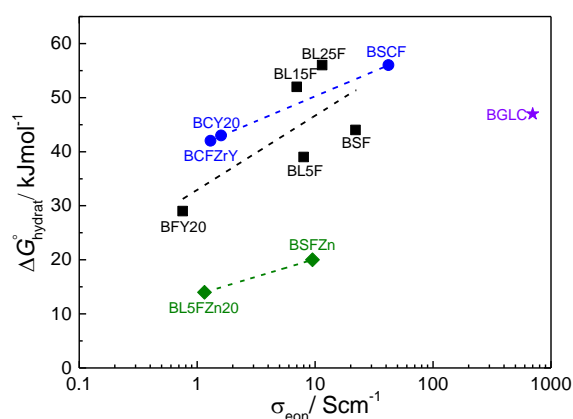


Figure 4-33: Gibbs free energy at 700K as a function of p-type electronic conductivity at 600 °C in air or pure O₂. Data for some of the materials are taken from literature: BSF and BSCF [91], BL5F [92], BSFZn [93], BCFZrY [1], BL15F and BL25F interpolated from Ba_{1-x}La_xFeO_{3- δ} ($x = 10, 20, 30, 40$) [65], BGLC = (Ba,La,Gd)₂Co₂O_{6- δ} [94], [95].

seems to be an overall positive trend within the groups of Zn-containing, Co-containing and the rest of the cathode materials, which means a compromise between electronic conductivity and proton incorporation is required. The reason is that the factors which enhance the p-type carriers mobility decrease the basicity of the oxide ions.

4.2.7 Ionic conductivity measurements

The oxygen vacancy conductivity of BL5FZn20 was measured after quenching the sample from 600 °C in dilute hydrogen at its minimum conductivity (where both n-type and p-type electronic carriers are suppressed) and then measuring the impedance spectra at different temperatures. The results are shown in Figure 4-34 which gives a migration barrier of 0.72 ± 0.1 eV. The oxygen vacancy conductivity is clearly smaller than electronic conductivity and this difference approaches orders of magnitude at lower T . The oxygen vacancy diffusivity at e.g. 250 °C and 400 °C is 7×10^{-10} cm²s⁻¹ and 5×10^{-8} cm²s⁻¹, respectively. Similar values of 2×10^{-9} cm²s⁻¹ (250 °C) and 1.2×10^{-7} cm²s⁻¹ (400 °C) for BSFZn [97] and 3×10^{-7} cm²s⁻¹ (400 °C) for BSCF [98] have been reported in literature.

A direct measurement of proton conductivity is quite complicated as it is difficult to suppress electronic carriers. Using a proton-selective double layer of LWO-BZY15 deposited by PLD on a BL5FZn20 pellet, the electronic carriers are expected to be blocked. However, impedance measurements at 200-350 °C in dry and humid N₂ indicate that the holes were not completely blocked (possibly some pinholes or cracks are present in the LWO-BZY15 layer). The measured capacitance is smaller than the large chemical capacitance expected for such an electronically blocked situation. A systematic reversible conductivity change was observed when switching from dry to humid gas and back, evidencing that protons affect the sample's transport properties and penetrate into the dense ceramic pellet. In the respective temperature range the proton conductivity should exceed the $V_{\text{O}}^{\bullet\bullet}$ conductivity (which has a much higher activation energy). But after an initial small decrease the low-frequency resistance increased when switching to humid gas, which indicates the measured conductivity is still predominantly hole conductivity (the hole concentration decreases in humid conditions

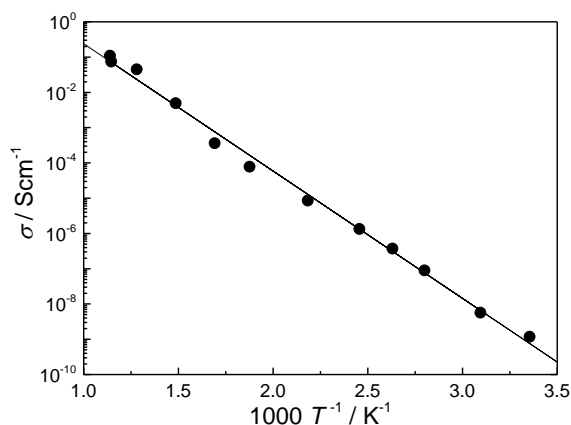


Figure 4-34: Oxygen vacancy conductivity of quenched BL5FZn in dry N₂. $E_a = 0.72 \pm 0.1$ eV.

because of proton uptake by the hydrogenation reaction). The two-fold character of the resistance change is in line with this interpretation.

4.2.8 Design strategies

A promising protonic cathode material finally should not only have a sufficiently high protonic and electronic conductivity, but also high catalytic activity and chemical stability against carbonate and hexagonal phase formation to improve its power efficiency and lifetime. The chemical and mechanical compatibility of the cathode with electrolyte, interconnect and sealing materials is important, too. Fulfilling all these criteria simultaneously is challenging as different element substitutions might have compromising effects.

The compromise between electronic and protonic conductivity has already been mentioned in 4.2.6. The Co-containing perovskites have higher electronic conductivity compared to Fe, Zn, and Y containing ones. One can notice in Figure 4-33 that BCFZrY, which shows promising performance [1], has a relatively low electronic conductivity, but a less positive $\Delta G_{\text{hydrat}}^{\circ}$, hence a greater proton uptake. This suggests that the PCFC cathodes can show good performances even when they have only moderate electronic conductivity.

A high catalytic activity for the oxygen reduction reaction is crucial for a good performance of the cathode material. A high Ba and Co content, also a high oxygen vacancy concentration are desired for the catalytic activity. As Co decreases the proton incorporation, partial substitution of Zn and/or Y can be helpful.

As Figure 4-26 (b) shows, the Goldschmidt factor (as a measure of phase stability) for a number of the studied cathode materials is close to or slightly higher than for BSCF which is known to transform to the hexagonal phase at $T = 700\text{-}900\text{ }^{\circ}\text{C}$ [85], [96]; e.g., in BCFZr, for which the Goldschmidt factor is higher than for BSCF, substitution of a highly charged cation on the B-site (Zr^{4+}), can effectively suppress this phase transformation. Some Y doping on the B-site (ionic radius 0.9 \AA for coordination number of 6) can bring t closer to unity (perfect cubic perovskite).

Chemical stability against carbonate formation at PCFC operation temperature is another necessity for a good cathode. The Ba-containing cathode materials such as BSCF are known to have issues with carbonate formation. However, only minor effects have been claimed for BCFZr when exposed to dilute CO_2 [37].

The compatibility of the electrolyte with the cathode is also of importance. For acceptor-doped $\text{Ba}(\text{Zr,Ce})\text{O}_3$ electrolyte, this is largely satisfied; however, Ba-containing cathode materials react with lanthanum tungstate, as discussed before in 3.1.4.

4.3 Surface oxygen reduction mechanism of the PCFC cathode materials

In this section, the oxygen reduction reaction for BSCF and BCFZrY is studied using LWO (with BZY buffer layer) and BZC10Y1 as alternative electrolytes with small electronic transference number (see 3.3). The dependency of R_s on electrode diameter (d), T , pO_2 and pH_2O is investigated for dense and/or porous microelectrodes. A constant phase element Q is used instead of a capacitor to fit impedance spectra with non-ideal semicircles. The capacitance can then be found knowing R , Q and the depression factor n according to [99]

$$C = (R^{1-n}Q)^{1/n} \quad (4.26)$$

The impedance spectrum contains typically three or four semicircles. The high frequency semicircle indicates the electrolyte ionic resistance and capacitance (in the order of pF). The medium frequency semicircle characterizes the BZY buffer layer or the blocking grain boundaries in BZC10Y1. The LWO electrolyte pellet does not have blocking grain boundaries. A second medium frequency semicircle can often be observed which can be attributed to the interface layer formed between the cathode and the electrolyte. This semicircle shows relatively large activation energy (~ 1.5 eV for porous BCFZrY on LWO-BZY) and is more visible when the sample is exposed to high temperature for extended time. The low frequency semicircle contains information about the surface reaction rate and the chemical capacitance of the whole volume of the microelectrode [100] (in the order of μ F). An example of impedance spectrum is shown in Figure 4-35 for porous BSCF on BZY-LWO at 700 °C. The equivalent circuit consists of three parallel R and Q elements, all in series as electronic leakage is expected to be negligible for samples with LWO electrolyte. This is equivalent to the exact circuit with $R_{LF}C_{LF}$ nested inside the $R_{MF}C_{MF}$ loop [101] as long as the relaxation time of the $R_{LF}C_{LF}$ is much larger than that of $R_{MF}C_{MF}$ (because of the larger chemical capacitance C_{LF}) [102]. The equivalent circuit shown in Figure 3-12 (a) is used for

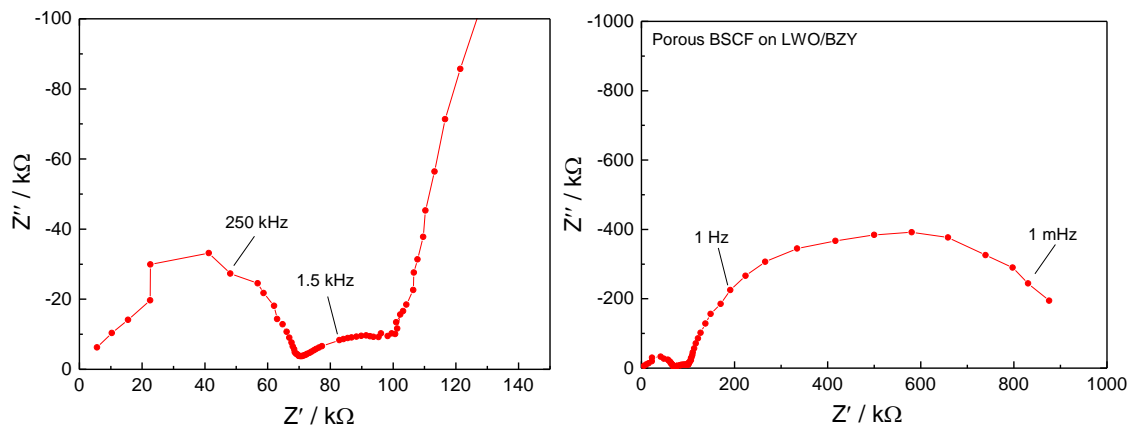


Figure 4-35: Example of impedance spectrum of 100 μ m porous BSCF on LWO (with BZY buffer layer) at 700 °C in 1000 ppm O_2 and 20 mbar H_2O . The three semicircles correspond to LWO (high frequency) and BZY (medium frequency) ionic resistance (left) and the surface oxygen reduction resistance (low frequency, right).

correction of the data measured on BZC10Y1 for electronic leakage.

Temperature dependence- Figure 4-36 (a) shows the Arrhenius plots of R_s for dense BSCF on LWO and BZC10Y1 electrolyte. The ionic resistance of the electrolytes is consistent with the measurements of section 3.3. The higher activation energy of R_i for BZC10Y1 is caused by its blocking grain boundaries. It can be observed that the presence of electronic leakage for BZC10Y1 (although small) decreases R_s for about half an order of magnitude compared to the LWO electrolyte. The activation energy for R_s in both cases is found to be quite close within the error bars (1.4-1.5 eV), also consistent with measurements of Daniel Pötzsch on BZY1 electrolyte (figure 4.39 in [24]). For BCFZrY on LWO, E_a is slightly smaller ($= 1.2 \pm 0.1$ eV for the porous and 1.1 ± 0.1 eV for the dense sample); R_s values for BCFZrY are also quite comparable with BSCF within the error bars.

In general, lower R_s values are expected for porous electrodes compared to dense ones due to their larger exposed surface area. Area specific resistance ASR_s for dense BCFZrY is found to be $\sim 80 \Omega\text{cm}^{-2}$ at 600 °C and 1 bar which is about an order of magnitude larger than the value reported for the porous BCFZrY in air in the literature [1]. The difference in results for the porous and dense BCFZrY and BSCF on BZY-LWO in this work is not much. This might be due to change in (surface) cation composition and thus catalytic activity because of the modified PLD conditions. However, a more detailed study is required.

Microelectrode diameter dependence- The variation of R_s with microelectrode diameter d indicates to what degree the bulk path is active for a certain cathode material. Ideally, R_s is expected to scale with d with a slope of -2 in a double logarithmic plot if the contribution from the bulk path dominates the overall current. When the slope is -1, the oxygen reduction reaction is limited to the triple phase boundary (or R_{con} dominates the electrode response). One should also consider that due to local cooling of the microelectrodes through the Pt/Ir tip, the slope is expected to be slightly overestimated (smaller microelectrodes bear more local

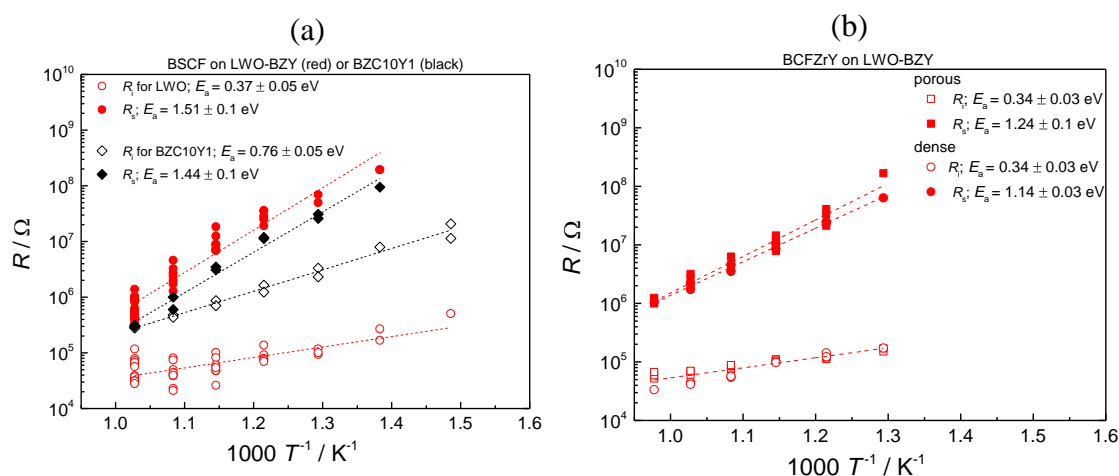


Figure 4-36: Surface reduction reaction resistance (R_s) and electrolyte ionic resistance (R_i) for (a) dense 100 μm BSCF on LWO-BZY and BZC10Y1 electrolyte and for (b) dense and porous 100 μm BCFZrY on LWO-BZY. All measurements are done in 1000 ppm O_2 and 20 mbar H_2O .

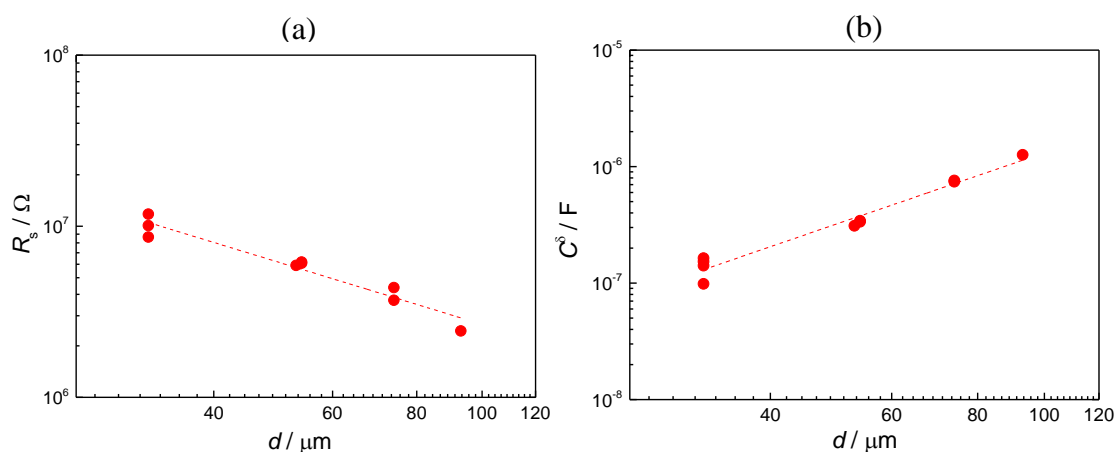


Figure 4-37: diameter dependence of (a) oxygen surface reduction reaction R_s and the (b) chemical capacitance at 650 °C, 1000 ppm O_2 and 20 mbar H_2O for dense BSCF microelectrodes on LWO/BZY.

cooling resulting in increasing of R_s) [24]. The chemical capacitance should also scale with the area at constant microelectrode thickness as it is related to the volume of the cathode. Figure 4-37 shows the diameter dependence of R_s and C^δ for dense BSCF on LWO at 650 °C with a slope of -1.2 ± 0.15 and -2.0 ± 0.15 , respectively. The real diameter of the microelectrodes is always few micrometers smaller than the nominal diameter according to SEM pictures. Interestingly, a similar result for porous BSCF on LWO-BZY (PLD at room T to form amorphous layer of the cathode followed by annealing at 850 °C / 2 h to form a porous crystalline cathode, see 3.1.4) for which the bulk path is highly expected to be active was found (-1.3 ± 0.1 and -1.8 ± 0.2). For the dense sample, the slope of R_s decreases to -1.5 ± 0.2 at 600 °C where the proton concentration slightly increases and the bulk path current is expected to contribute more to the total current. For dense BCFZrY on LWO, the slopes are -1.2 ± 0.1 and -2.6 ± 0.1 , less negative than expected for BCFZrY with a higher proton concentration compared to BSCF. However, there seemed to be adhesion problems between the cathode and electrolyte in this case (high surface roughness of the substrate) which made the measurements problematic.

Partial pressure dependence- The oxygen and water partial pressure dependence of R_s can give some information about the rate-determining step of the oxygen surface reduction reaction. In general, R_s is proportional to pO_2^m and pH_2O^n . One should note that since the (surface) defect concentrations, $[V_O^{\bullet\bullet}]$, $[OH_O^{\bullet}]$, and $[h^{\bullet}]$ are oxygen and water partial pressure dependent (see Figure 2-1 for the case of (bulk) defects), they also contribute to the exponents m and n [46].

The pO_2 dependence of R_s is shown in Figure 4-38 (a) for BSCF on BZY-LWO. m increases upon decreasing of T (compare m at 600 °C and 650 °C on LWO electrolyte). In [24], m was reported to be $-0.56(1)$ at 550 °C for the same material (80 μm , on BZY1 electrolyte). In this work, m was found to be less negative than -0.5 . However, for realistic mechanisms the pO_2 dependence of individual defects such as electrons, holes, and oxygen

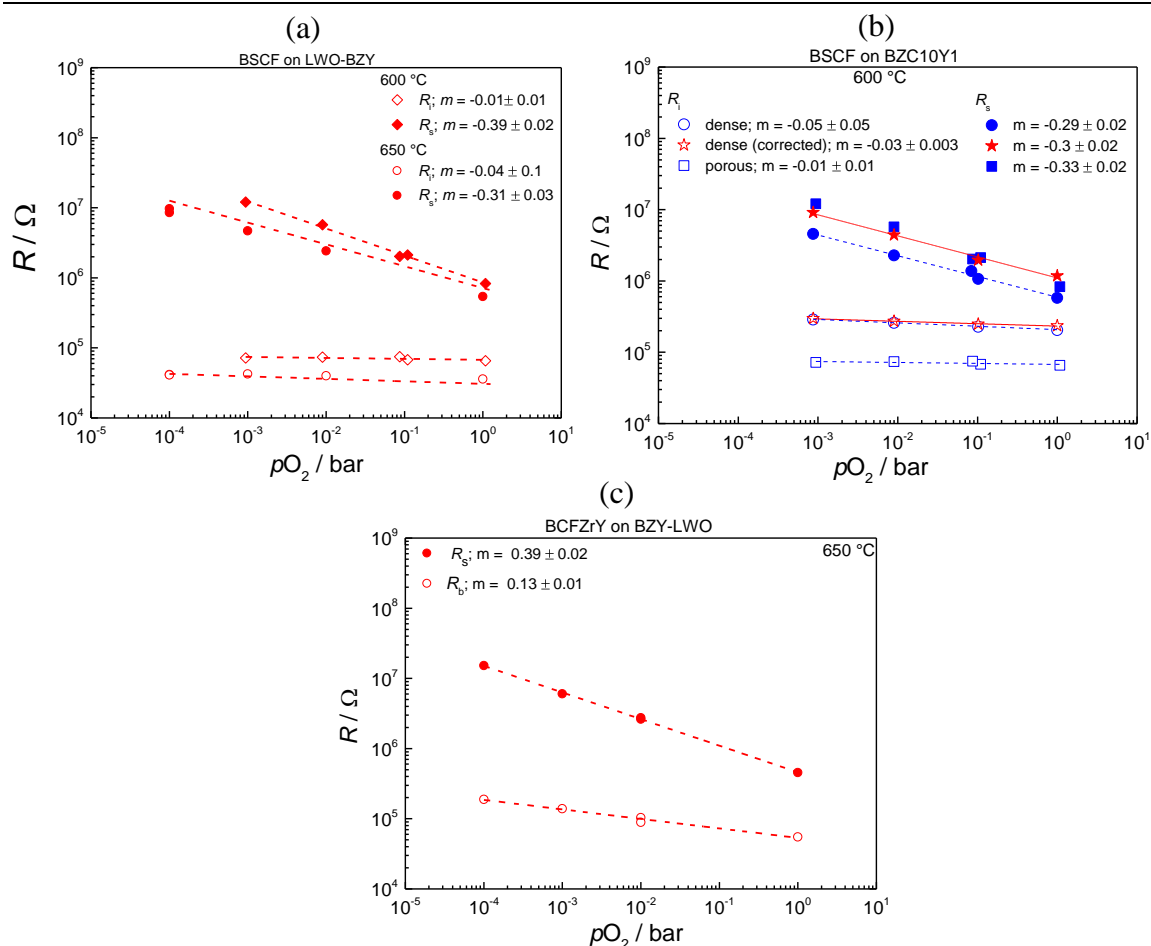


Figure 4-38: pO_2 dependence in 20 mbar H_2O (a) for dense 100 μm BSCF microelectrode on LWO-BZY (600 and 650 °C), (b) for dense and porous 100 μm BSCF microelectrode on BZC10Y1; the results for dense microelectrodes are also corrected for the electronic leakage (red stars) using the equivalent circuit shown in Figure 3-12 (a). (c) pO_2 dependence for porous 100 μm BCFZrY on LWO-BZY at 650 °C.

vacancies leads to overall pO_2 dependences of ≤ 0.25 if only atomic oxygen species are involved in the rate determining step [46]. Therefore molecular oxygen species most probably contribute to the rate determining step. The ionic resistance of the electrolyte gives $m < -0.04 \pm 0.01$ for LWO. This proves once more that the electronic leakage for LWO is negligible.

The results for dense (blue circles) and porous (blue squares) BSCF microelectrodes on BZC10Y1 at 600 °C are shown in Figure 4-38 (b). It is noticeable that the R_s values for the porous samples are larger than for the dense one since the electronic resistance affects the dense sample more. Correction of the results for the dense sample using the equivalent circuit of Figure 3-12 (a) and the R_{con} values from table 3-4 gives R_s values quite close to the ones found for the porous sample, also the measurements done on BZY-LWO at 600 °C (Figure 4-38 (a)) indicating that for these measurements the electronic leakage can be largely corrected.

For porous BCFZrY on LWO, $m = -0.4 \pm 0.02$ at 650 °C, however for unknown reason a slight pO_2 dependence of R_i is in this case is observed. The results are shown in Figure 4-38 (c).

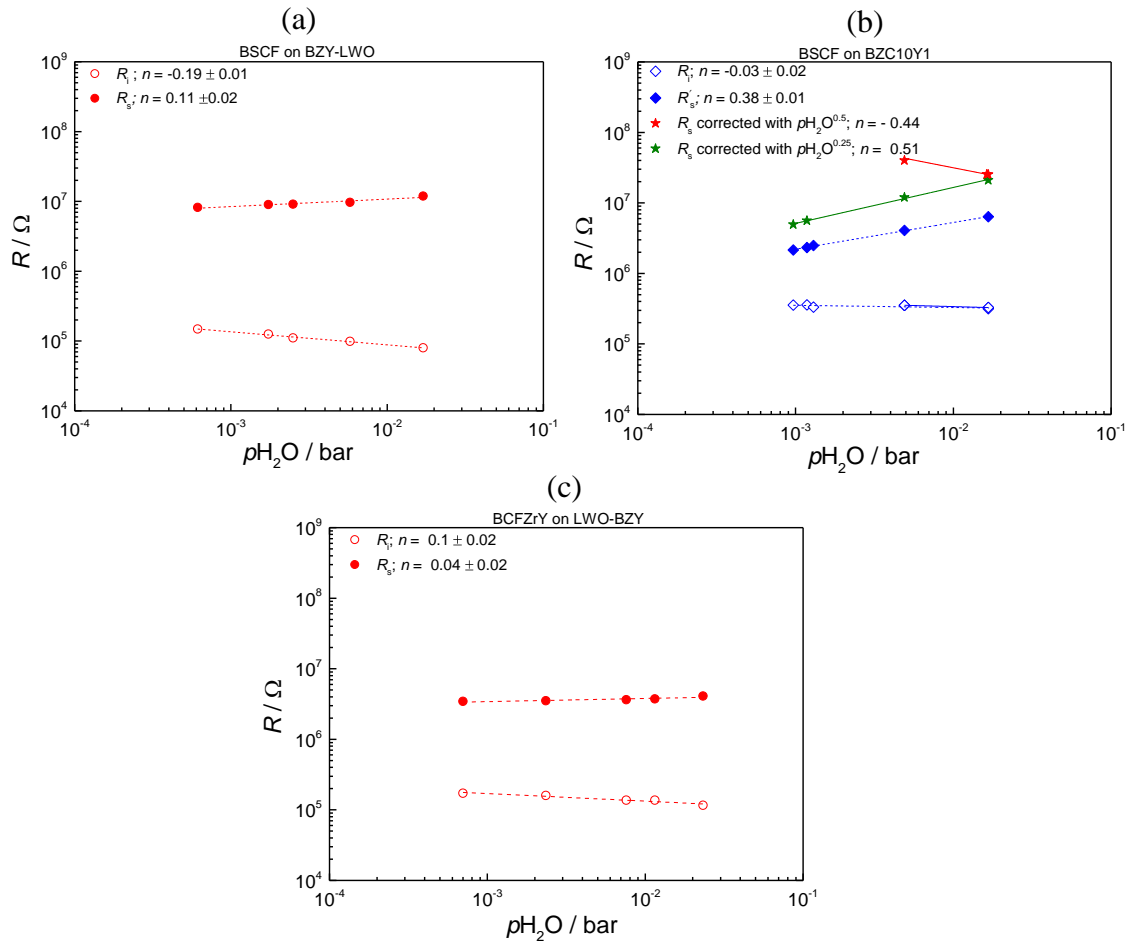


Figure 4-39: $p\text{H}_2\text{O}$ dependence in 1000 ppm O_2 for 100 μm (a) BSCF on BZY-LWO (650 $^\circ\text{C}$) and (b) BSCF on BZC10Y1 (600 $^\circ\text{C}$, with and without correction for the electronic leakage) (b) and for porous BCFZrY on BZY-LWO (650 $^\circ\text{C}$).

The value for the water partial pressure exponent n is found to be quite sensitive to the choice of the electrolyte. In 1 bar O_2 , 550 $^\circ\text{C}$ and 80 μm , n was found to be 0.5 (1) for BSCF on BZY6 [24] which is strongly positive. However, since the water partial pressure dependence of electronic resistance is also positive, it could lead to a misinterpretation of the data. In this work, n is found to be 0.11 for BSCF on LWO (650 $^\circ\text{C}$) and 0.38 on BZC10Y1 (600 $^\circ\text{C}$, without correction) which is less positive. Assuming two cases of $R_{\text{con}} \propto p\text{H}_2\text{O}^{0.5}$ and $R_{\text{con}} \propto p\text{H}_2\text{O}^{0.25}$ (see Table 3-5), the results for BSCF on BZC10Y1 are corrected (red and green stars). When R_{con} decreases to the values close to the low frequency semicircle diameter in low $p\text{H}_2\text{O}$, it is not possible to reliably correct the results (although the fitting error bars are typically an order of magnitude smaller than the absolute values). A negative slope of $n = -0.44$ for $R_{\text{con}} \propto p\text{H}_2\text{O}^{0.5}$ and a positive slope of $n = 0.51$ for $R_{\text{con}} \propto p\text{H}_2\text{O}^{0.25}$ are found indicating that the correction is very sensitive to the choice of R_{con} and correspondingly the n values are not very reliable for this case.

In general, the small values found for n on BZY-LWO suggest that protons do not contribute to the rate determining step. The slight positive value reflects the $p\text{H}_2\text{O}$ dependence of some surface the defect concentrations involved (e.g. the surface $\text{V}_\text{O}^{\bullet\bullet}$ concentration is

expected to decrease with increasing $p_{\text{H}_2\text{O}}$). The $p_{\text{H}_2\text{O}}$ dependence of porous BCFZrY on BZY-LWO in the similar condition resulted in $n = 0.05 \pm 0.02$ (almost no water partial pressure dependence).

In conclusion, investigation of the surface oxygen exchange kinetics of BSCF and BCFZrY shows that the surface reduction reaction is not limited to the triple phase boundary as a slope of more negative than -1 is observed in the diameter dependence measurements. Furthermore, the molecular oxygen species are and the protons are not involved in the rate determining step according to the partial pressure dependence measurements. LWO can be used as an electrolyte for study of surface reduction reaction in gas symmetric cells in oxidizing conditions, as electronic leakage can be mainly suppressed. The study on porous microelectrodes still needs more consideration.

5 Conclusion and Summary

This work focuses on studying the thermodynamics and kinetics of mixed-conducting perovskite materials as electrodes for intermediate temperature protonic ceramic fuel cells. Oxygen vacancies, protons, and holes are the relevant defects in these materials.

In the first part, the two-fold stoichiometry relaxation upon $p\text{H}_2\text{O}$ change was studied for the perovskites with only redox-inactive elements on the B-site such as $\text{BaZrO}_{3-\delta}$. Finite-difference simulations were performed to calculate the change of defect concentration and conductivity relaxation as a function of time after a $p\text{H}_2\text{O}$ change. From this, four phenomenological diffusion coefficients could be calculated: D^{fast} and D^{slow} which are related to hole concentration changes and determine the conductivity relaxation curve; and $D_{\text{H}}^{\text{eff}}$ and $D_{\text{O}}^{\text{eff}}$ which are related to $\text{V}_{\text{O}}^{\bullet\bullet}$ and $\text{OH}_{\text{O}}^{\bullet}$ concentration and determine the weight relaxation. It could be shown that considering trapping of the holes in the model, a good agreement of the temperature dependence of D^{fast} with measured activation energies from the literature could be achieved.

The main part of this work deals with the hydration thermodynamics of cathode perovskites with different compositions. Since the proton incorporation can occur through hydration or hydrogenation reactions, the proton uptake measurements were mainly performed for the case of frozen oxygen exchange surface reaction. The samples were equilibrated at typically 600-700 °C and quenched to the desired temperature; then, the weight gain upon $p\text{H}_2\text{O}$ changes was measured. This has been performed mainly for $(\text{Ba,Sr,La})(\text{Fe,Co,Zn,Zr,Y})\text{O}_{3-\delta}$ compounds. The following results have been found:

- The proton concentration in $\text{SrFeO}_{3-\delta}$ is small due to formation of superstructures of vacant oxygen sites which disfavors hydration. Partial Ba substitution on the A-site suppresses this ordering; it also enhances the proton incorporation compared to Sr and La as it is less electronegative. However, some Sr or La is needed to maintain the cubic perovskite structure ($\text{BaFeO}_{3-\delta}$ is hexagonal).
- The partial substitution of Sr or Ba with La on the A-site decreases the oxygen vacancy and increase the hole concentration. Both decrease the proton incorporation.
- Co on the B-site decreases the proton incorporation. This can be attributed to the stronger Co–O covalency compared to Fe–O, which decreases the oxide ion basicity and increases the hole-proton defect interaction.
- Zn is beneficial for proton uptake. It does not act as an acceptor, but it additionally decreases the defect interactions by interrupting the hole delocalization. This suggests that the presence of redox-inactive element on the B-site is helpful.

For samples such as $(\text{La}_{0.5}\text{Sr}_{0.5})\text{FeO}_{3-\delta}$ and $(\text{Ba}_{0.5}\text{La}_{0.5})\text{FeO}_{3-\delta}$, the hole concentration was so high that it was difficult to suppress the holes by quenching measurements. For these samples, the hydrogenation reaction was predominant.

In general, the degree of hydration is smaller for cathode materials compared to the $\text{Ba}(\text{Zr,Cr,Y})\text{O}_{3-\delta}$ electrolytes which are fully hydrated at low temperatures.

The cathode materials have a more positive $\Delta G_{\text{hydrat}}^{\circ}$, a less negative standard enthalpy and a more negative standard entropy compared to the electrolytes. Among different correlation plots, the most interesting one is the variation of $\Delta G_{\text{hydrat}}^{\circ}$ (as a measure of the propensity for proton uptake) as a function of cation electronegativity (which will affect the oxide ion basicity). While all cathode materials follow one correlation line, the electrolyte materials lie on a different line. This indicates that additional parameters such as the B–O convalency are required to explain the proton incorporation of the cathodes. Since the increasing B–O covalency and corresponding hole delocalization decrease the oxide ion basicity, the hole conductivity shows the opposite trend with $\Delta G_{\text{hydrat}}^{\circ}$. Among the measured perovskites, $(\text{Ba}_{0.95}\text{La}_{0.05})(\text{Fe}_{0.8}\text{Zn}_{0.2})\text{O}_{3-\delta}$ has the highest proton concentration of 10 mol% at 250 °C (measured with quenched oxygen stoichiometry), and remains comparably high also when equilibrated with higher $p\text{O}_2$ s. While its hole conductivity is not very high (1.2 Scm^{-1}) such values have been proven to suffice for PCFC cathode operation on the example of $\text{Ba}(\text{Co}_{0.4}\text{Fe}_{0.4}\text{Zr}_{0.1}\text{Y}_{0.1})\text{O}_{3-\delta}$ in the literature.

The quantitative analysis of oxygen stoichiometry in dry conditions and the variation of proton content with hole concentration proved that hole-hole and hole-proton defect interactions cannot be neglected. The hole-hole interactions show up in a flattening of the oxygenation van 't Hoff plot at lower temperatures, i.e. the presence of holes disfavors further oxygen uptake. The presence of holes has also a detrimental effect on proton uptake. This can be recognized when comparing the proton concentration for oxygen equilibrated and quenched samples. Although the $V_{\text{O}}^{\bullet\bullet}$ concentration in the equilibrated sample is still high, already the presence of a small hole concentration drastically decreases the proton incorporation. The hole-hole as well as hole-proton interaction can be attributed to the partial delocalization of holes from the transition metal (typically Fe for which the holes are present as small polaron) to the adjacent oxide ions. This decreases the basicity of the oxide ions which disfavors proton uptake, and leads to an enhanced mutual perception of the holes decreasing the tendency for additional oxygen incorporation.

The hole-hole and hole-proton interaction was quantified using a first order correction, which assumes that the oxygenation and hydration enthalpy change linearly as a function of hole concentration. The values of the interaction parameter were found to be rather similar for oxygenation and hydration. They change systematically in the $(\text{Ba,L a})\text{FeO}_{3-\delta}$ family for which a higher La content increases the interaction parameter. Furthermore, the interaction

parameter is quite small for $(\text{Ba}_{0.95}\text{La}_{0.05})(\text{Fe}_{0.8}\text{Zn}_{0.2})\text{O}_{3-\delta}$ indicating that Zn suppresses the interactions.

The hydration van 't Hoff plot of the materials with relatively high proton incorporation such as $(\text{Ba}_{0.95}\text{La}_{0.05})(\text{Fe}_{0.8}\text{Zn}_{0.2})\text{O}_{3-\delta}$ and $(\text{Ba}_{0.5}\text{Sr}_{0.5})(\text{Fe}_{0.8}\text{Zn}_{0.2})\text{O}_{3-\delta}$ bends at lower temperature where proton concentration is high indicating that for such materials also proton-proton interactions might become relevant.

A direct measurement of proton conductivity in cathode materials is challenging as it is difficult to sufficiently suppress the electronic carriers. However, applying a proton selective layer of $\text{La}_{27}\text{W}_5\text{O}_{54+\delta}$ (together with a $\text{Ba}(\text{Zr},\text{Y})\text{O}_{3-\delta}$ buffer layer) the holes can be largely blocked. In this case, a reversible behavior of the conductivity upon switching from dry to humid condition and back again is observed.

The surface kinetics study of the cathode materials $(\text{Ba}_{0.5}\text{Sr}_{0.5})(\text{Co}_{0.8}\text{Fe}_{0.2})\text{O}_{3-\delta}$ and $\text{Ba}(\text{Co}_{0.4}\text{Fe}_{0.4}\text{Zr}_{0.1}\text{Y}_{0.1})\text{O}_{3-\delta}$ on electrolyte materials $\text{La}_{27}\text{W}_5\text{O}_{54+\delta}$ (with $\text{Ba}(\text{Zr}_{0.85}\text{Y}_{0.15})\text{O}_{3-\delta}$ buffer layer) and $\text{Ba}(\text{Zr}_{0.89}\text{Ce}_{0.1}\text{Y}_{0.01})\text{O}_{3-\delta}$ reveals once more that the electronic leakage of the electrolyte in the gas symmetric cells at oxidizing condition might make the kinetics study of the cathode materials sophisticated. For $(\text{Ba}_{0.5}\text{Sr}_{0.5})(\text{Co}_{0.8}\text{Fe}_{0.2})\text{O}_{3-\delta}$, the activation energy was found to be close to previous studies on $\text{Ba}(\text{Zr}_{0.99}\text{Y}_{0.01})\text{O}_{3-\delta}$. The diameter dependence of the surface oxygen reduction reaction for both cathodes is larger than 1, showing that the bulk path is expected to be partially active. The $p\text{O}_2$ and $p\text{H}_2\text{O}$ dependence study reveals that molecular oxygen is expected to be involved in the rate determining step. The $p\text{H}_2\text{O}$ dependence studies are quite sensitive to the electrolyte's electronic transference number since the electronic resistance itself increases with $p\text{H}_2\text{O}$. The exponent was found to be quite small for cathode materials when studied on LWO which means that the water species are not involved in the rate determining step.

Overall it can be concluded that within the present thesis a far-reaching understanding of the defect chemistry of mixed conducting perovskites with $\text{V}_\text{O}^{\bullet\bullet}$, $\text{OH}_\text{O}^\bullet$, and h^\bullet has been achieved, including the importance of defect interactions and the fundamentally different behavior of electrolyte and cathode materials. The basicity of the oxide ions - which itself is influenced by cation composition, cation oxidation state, local lattice distortions, *etc.* has been shown to be a key parameter for proton uptake. This knowledge may now serve as the basis for further PCFC cathode development, in particular since a number of desired properties (proton uptake, catalytic activity, electronic conductivity, *etc.*) have conflicting tendencies and an insightful optimization strategy is required.

References

- [1] C. Duan, J. Tong, M. Shang, S. Nikodemski, M. Sanders, S. Ricote, A. Almansoori, and R. O'Hayre, "Readily processed protonic ceramic fuel cells with high performance at low temperatures," *Science.*, vol. 349, no. 6254, pp. 1321-1326, Sep. 2015.
- [2] K. D. Kreuer, "Proton-conducting oxides," *Annu. Rev. Mater. Res.*, vol. 33, no. 1, pp. 333-359, Aug. 2003.
- [3] Y. Matsuzaki, Y. Tachikawa, T. Somekawa, T. Hatae, H. Matsumoto, S. Taniguchi, and K. Sasaki, "Effect of proton-conduction in electrolyte on electric efficiency of multi-stage solid oxide fuel cells," *Sci. Rep.*, vol. 5, no. 1, p. 12640, Oct. 2015.
- [4] N. T. Q. Nguyen and H. H. Yoon, "Preparation and evaluation of $\text{BaZr}_{0.1}\text{Ce}_{0.7}\text{Y}_{0.1}\text{Yb}_{0.1}\text{O}_{3-\delta}$ (BZCYYb) electrolyte and BZCYYb-based solid oxide fuel cells," *J. Power Sources*, vol. 231, pp. 213-218, Jun. 2013.
- [5] M. Shang, J. Tong, and R. O'Hayre, "A promising cathode for intermediate temperature protonic ceramic fuel cells: $\text{BaCo}_{0.4}\text{Fe}_{0.4}\text{Zr}_{0.2}\text{O}_{3-\delta}$," *RSC Adv.*, vol. 3, no. 36, p. 15769, 2013.
- [6] K. Bae, H. S. Noh, D. Y. Jang, J. Hong, H. Kim, K. J. Yoon, J. H. Lee, B. K. Kim, J. H. Shim, and J. W. Son, "High-performance thin-film protonic ceramic fuel cells fabricated on anode supports with a non-proton-conducting ceramic matrix," *J. Mater. Chem. A*, vol. 4, no. 17, pp. 6395-6403, 2016.
- [7] K. Bae, D. Y. Jang, H. J. Choi, D. Kim, J. Hong, B. K. Kim, J. H. Lee, J. W. Son, and J. H. Shim, "Demonstrating the potential of yttrium-doped barium zirconate electrolyte for high-performance fuel cells," *Nat. Commun.*, vol. 8, p. 14553, Feb. 2017.
- [8] S. Choi, C. J. Kucharczyk, Y. Liang, X. Zhang, I. Takeuchi, H. I. Ji, and S. M. Haile, "Exceptional power density and stability at intermediate temperatures in protonic ceramic fuel cells," *Nat. Energy*, vol. 3, no. 3, pp. 202-210, Mar. 2018.
- [9] A. Dubois, S. Ricote, and R. J. Braun, "Benchmarking the expected stack manufacturing cost of next generation, intermediate-temperature protonic ceramic fuel cells with solid oxide fuel cell technology," *J. Power Sources*, vol. 369, pp. 65-77, Nov. 2017.
- [10] F. Iguchi, T. Yamada, N. Sata, T. Tsurui, and H. Yugami, "The influence of grain structures on the electrical conductivity of a $\text{BaZr}_{0.95}\text{Y}_{0.05}\text{O}_3$ proton conductor," *Solid State Ionics*, vol. 177, no. 26-32, pp. 2381-2384, Oct. 2006.
- [11] A. K. Azad and J. T. S. Irvine, "Synthesis, chemical stability and proton conductivity of the perovskites $\text{Ba}(\text{Ce,Zr})_{1-x}\text{Sc}_x\text{O}_{3-\delta}$," *Solid State Ionics*, vol. 178, no. 7-10, pp. 635-640, 2007.
- [12] F. Iguchi, N. Sata, T. Tsurui, and H. Yugami, "Microstructures and grain boundary conductivity of $\text{BaZr}_{1-x}\text{Y}_x\text{O}_{3-\delta}$ ($x = 0.05, 0.10, 0.15$) ceramics," *Solid State Ionics*, vol. 178, no. 7-10, pp. 691-695, Apr. 2007.

- [13] P. Babilo, T. Uda, and S. M. Haile, "Processing of yttrium-doped barium zirconate for high proton conductivity," *J. Mater. Res.*, vol. 22, no. 05, pp. 1322-1330, May 2007.
- [14] Y. Yamazaki, R. Hernandez-Sanchez, and S. M. Haile, "Cation non-stoichiometry in yttrium-doped barium zirconate: phase behavior, microstructure, and proton conductivity," *J. Mater. Chem.*, vol. 20, no. 37, p. 8158, 2010.
- [15] S. Imashuku, T. Uda, and Y. Awakura, "Sintering properties of trivalent cation-doped Barium Zirconate at 1600°C," *Electrochem. Solid-State Lett.*, vol. 10, no. 10, p. B175, 2007.
- [16] P. Babilo and S. M. Haile, "Enhanced sintering of yttrium-doped barium zirconate by addition of ZnO," *J. Am. Ceram. Soc.*, vol. 88, no. 9, pp. 2362-2368, Sep. 2005.
- [17] S. Tao and J. T. S. Irvine, "Conductivity studies of dense yttrium-doped BaZrO₃ sintered at 1325°C," *J. Solid State Chem.*, vol. 180, no. 12, pp. 3493-3503, Dec. 2007.
- [18] S. Ricote, N. Bonanos, A. Manerbino, and W. G. Coors, "Conductivity study of dense BaCe_xZr_(0.9-x)Y_{0.1}O_{3-δ} prepared by solid state reactive sintering at 1500 °C," *Int. J. Hydrogen Energy*, vol. 37, no. 9, pp. 7954-7961, May 2012.
- [19] J. Tong, D. Clark, M. Hoban, and R. O'Hayre, "Cost-effective solid-state reactive sintering method for high conductivity proton conducting yttrium-doped barium zirconium ceramics," *Solid State Ionics*, vol. 181, no. 11-12, pp. 496-503, Apr. 2010.
- [20] R. Merkle, D. Poetzsch, and J. Maier, "Oxygen reduction reaction at cathodes on proton conducting oxide electrolytes: contribution from three phase boundary compared to bulk path," *ECS Trans.*, vol. 66, no. 2, pp. 95-102, May 2015.
- [21] V. Brichzin, "The geometry dependence of the polarization resistance of Sr-doped LaMnO₃ microelectrodes on yttria-stabilized zirconia," *Solid State Ionics*, vol. 152-153, pp. 499-507, Dec. 2002.
- [22] D. Poetzsch, R. Merkle, and J. Maier, "Proton uptake in the H⁺-SOFC cathode material Ba_{0.5}Sr_{0.5}Fe_{0.8}Zn_{0.2}O_{3-δ}: transition from hydration to hydrogenation with increasing oxygen partial pressure," *Faraday Discuss.*, vol. 182, pp. 129-143, 2015.
- [23] D. Poetzsch, R. Merkle, and J. Maier, "Proton conductivity in mixed-conducting BSFZ perovskite from thermogravimetric relaxation," *Phys. Chem. Chem. Phys.*, vol. 16, no. 31, p. 16446, Jul. 2014.
- [24] D. Poetzsch, "Mixed-conducting (Ba,Sr)(Co,Fe,Zn)O_{3-δ} as cathode material for proton-conducting ceramic fuel cells: Defect chemistry and oxygen reduction mechanism," PhD thesis, University of Stuttgart, 2014.
- [25] D. Poetzsch, R. Merkle, and J. Maier, "Stoichiometry variation in materials with three mobile carriers - Thermodynamics and transport kinetics exemplified for protons, oxygen vacancies, and holes," *Adv. Funct. Mater.*, vol. 25, no. 10, pp. 1542-1557, Mar. 2015.
- [26] J. H. Yu, J. S. Lee, and J. Maier, "Peculiar nonmonotonic water incorporation in oxides detected by local in-situ optical absorption spectroscopy," *Angew. Chemie Int. Ed.*, vol.

- 46, no. 47, pp. 8992-8994, Dec. 2007.
- [27] J. H. Yu, J. S. Lee, and J. Maier, "Water incorporation in oxides: A moving boundary problem," *Solid State Ionics*, vol. 181, no. 3-4, pp. 154-162, Feb. 2010.
- [28] P. Kofstadt, *Non-stoichiometry, diffusion and electrical conductivity in binary metal oxides.*, Wiley-Interscience, 1972.
- [29] J. E. ten Elshof, "Oxygen exchange and diffusion coefficients of strontium-doped lanthanum ferrites by electrical conductivity relaxation," *J. Electrochem. Soc.*, vol. 144, no. 3, p. 1060, 1997.
- [30] J. Maier, "Mass transport in the presence of internal defect reactions- concept of conservative ensembles: I, chemical diffusion in pure compounds," *J. Am. Ceram. Soc.*, vol. 76, no. 5, pp. 1223-1227, May 1993.
- [31] J. Maier, "Mass transport in the presence of internal defect reactions- concept of conservative ensembles: II, evaluation of electrochemical transport measurements," *J. Am. Ceram. Soc.*, vol. 76, no. 5, pp. 1223-1227, May 1993.
- [32] J. Maier, "Mass transport in the presence of internal defect reactions- concept of conservative ensembles: III, trapping effect of dopants on chemical diffusion," *J. Am. Ceram. Soc.*, vol. 76, no. 5, pp. 1223-1227, May 1993.
- [33] G. R. Kim, H. H. Seo, J. M. Jo, E. C. Shin, J. H. Yu, and J. S. Lee, "Moving boundary diffusion problem for hydration kinetics evidenced in non-monotonic conductivity relaxations of proton conducting perovskites," *Solid State Ionics*, vol. 272, pp. 60-73, Apr. 2015.
- [34] H. I. Yoo, J. Y. Yoon, J. S. Ha, and C. E. Lee, "Hydration and oxidation kinetics of a proton conductor oxide, $\text{SrCe}_{0.95}\text{Yb}_{0.05}\text{O}_{2.975}$," *Phys. Chem. Chem. Phys.*, vol. 10, no. 7, pp. 974-982, 2008.
- [35] H. I. Yoo, J. I. Yeon, and J. K. Kim, "Mass relaxation vs. electrical conductivity relaxation of a proton conducting oxide upon hydration and dehydration," *Solid State Ionics*, vol. 180, no. 28-31, pp. 1443-1447, Nov. 2009.
- [36] D. K. Lim, M. B. Choi, K. T. Lee, H. S. Yoon, E. D. Wachsman, and S. J. Song, "Conductivity relaxation of proton-conducting $\text{BaCe}_{0.85}\text{Y}_{0.15}\text{O}_{3-\delta}$ upon oxidation and reduction," *J. Electrochem. Soc.*, vol. 158, no. 8, p. B852, 2011.
- [37] J. Tong, W. S. Yang, B. Zhu, and R. Cai, "Investigation of ideal zirconium-doped perovskite-type ceramic membrane materials for oxygen separation," *J. Memb. Sci.*, vol. 203, no. 1-2, pp. 175-189, Jun. 2002.
- [38] N. Hayashi, T. Yamamoto, A. Kitada, A. Matsuo, K. Kindo, J. Hester, H. Kageyama, and M. Takano, "Field-induced ferromagnetism of Fe^{4+} -perovskite system, $\text{Sr}_{1-x}\text{Ba}_x\text{FeO}_3$ ($0 \leq x \leq 1$)," *J. Phys. Soc. Japan*, vol. 82, no. 11, p. 113702, Nov. 2013.
- [39] H. Wang, C. Tablet, W. Yang, and J. Caro, "In situ high temperature X-ray diffraction studies of mixed ionic and electronic conducting perovskite-type membranes," *Mater. Lett.*, vol. 59, no. 28, pp. 3750-3755, Dec. 2005.

- [40] Z. A. Munir, U. Anselmi-Tamburini, and M. Ohyanagi, "The effect of electric field and pressure on the synthesis and consolidation of materials: A review of the spark plasma sintering method," *J. Mater. Sci.*, vol. 41, no. 3, pp. 763-777, Feb. 2006.
- [41] F. S. Baumann, "Oxygen reduction kinetics on mixed conducting SOFC model cathodes," PhD thesis, University of Stuttgart, 2006.
- [42] P. Plonczak, A. Bieberle-Hütter, M. Sjøgaard, T. Ryll, J. Martynczuk, P. V. Hendriksen, and L. J. Gauckler, "Tailoring of $\text{La}_x\text{Sr}_{1-x}\text{Co}_y\text{Fe}_{1-y}\text{O}_{3-\delta}$ nanostructure by pulsed laser deposition," *Adv. Funct. Mater.*, vol. 21, no. 14, pp. 2764-2775, Jul. 2011.
- [43] G. Gregori, M. Shirpour, and J. Maier, "Proton conduction in dense and porous nanocrystalline ceria thin films," *Adv. Funct. Mater.*, vol. 23, no. 47, pp. 5861-5867, Dec. 2013.
- [44] D. Han, Y. Okumura, Y. Nose, and T. Uda, "Synthesis of $\text{La}_{1-x}\text{Sr}_x\text{Sc}_{1-y}\text{Fe}_y\text{O}_{3-\delta}$ (LSSF) and measurement of water content in LSSF, LSCF and LSC hydrated in wet artificial air at 300°C," *Solid State Ionics*, vol. 181, no. 35-36, pp. 1601-1606, Nov. 2010.
- [45] D. Poetzsch, R. Merkle, and J. Maier, "Investigation of oxygen exchange kinetics in proton-conducting ceramic fuel cells: Effect of electronic leakage current using symmetric cells," *J. Power Sources*, vol. 242, pp. 784-789, Nov. 2013.
- [46] D. Poetzsch, R. Merkle, and J. Maier, "Oxygen reduction at dense thin-film microelectrodes on a proton-conducting electrolyte: I. Considerations on reaction mechanism and electronic leakage effects," *J. Electrochem. Soc.*, vol. 162, no. 9, pp. F939-F950, Jun. 2015.
- [47] K. Nomura and H. Kageyama, "Transport properties of $\text{Ba}(\text{Zr}_{0.8}\text{Y}_{0.2})\text{O}_{3-\delta}$ perovskite," *Solid State Ionics*, vol. 178, no. 7-10, pp. 661-665, Apr. 2007.
- [48] M. Oishi, S. Akoshima, K. Yashiro, K. Sato, J. Mizusaki, and T. Kawada, "Defect structure analysis of B-site doped perovskite-type proton conducting oxide BaCeO_3 , Part 2: The electrical conductivity and diffusion coefficient of $\text{BaCe}_{0.9}\text{Y}_{0.1}\text{O}_{3-\delta}$," *Solid State Ionics*, vol. 179, no. 39, pp. 2240-2247, Dec. 2008.
- [49] A. Magrasó, C. Frontera, D. Marrero-López, and P. Núñez, "New crystal structure and characterization of lanthanum tungstate ' $\text{La}_6\text{WO}_{12}$ ' prepared by freeze-drying synthesis," *Dalt. Trans.*, no. 46, p. 10273, 2009.
- [50] A. Magrasó, "Transport number measurements and fuel cell testing of undoped and Mo-substituted lanthanum tungstate," *J. Power Sources*, vol. 240, pp. 583-588, Oct. 2013.
- [51] R. Merkle, R. Zohourian, and J. Maier, "Two-fold stoichiometry relaxation- Simulated relaxation kinetics of ionic and electronic defect concentrations," *Solid State Ionics*, vol. 288, pp. 291-297, May 2016.
- [52] H. G. Bohn and T. Schober, "Electrical conductivity of the high-temperature proton conductor $\text{BaZr}_{0.9}\text{Y}_{0.1}\text{O}_{2.9}$," *J. Am. Ceram. Soc.*, vol. 83, no. 4, pp. 768-772, 2000.
- [53] E. Kim and H. I. Yoo, "Two-fold -to-single-fold transition of the conductivity

- relaxation patterns of proton-conducting oxides upon hydration/dehydration,” *Solid State Ionics*, vol. 252, pp. 132-139, Dec. 2013.
- [54] N. H. Chan, R. K. Sharma, and D. M. Smyth, “Nonstoichiometry in undoped BaTiO₃,” *J. Am. Ceram. Soc.*, vol. 64, no. 9, pp. 556-562, Sep. 1981.
- [55] M. Fleischer, H. Meixner, and C. Tragut, “Hole mobility in acceptor-doped, monocrystalline SrTiO₃,” *J. Am. Ceram. Soc.*, vol. 75, no. 6, pp. 1666-1668, Jun. 1992.
- [56] H. I. Yoo and K. D. Becker, “Effect of hole-trapping on mass/charge transport properties in acceptor-doped BaTiO₃,” *Phys. Chem. Chem. Phys.*, vol. 7, no. 9, p. 2068, 2005.
- [57] A. Lindman, P. Erhart, and G. Wahnström, “Implications of the band gap problem on oxidation and hydration in acceptor-doped barium zirconate,” *Phys. Rev. B*, vol. 91, no. 24, p. 245114, Jun. 2015.
- [58] H. I. Ji, B. K. Kim, J. H. Yu, S. M. Choi, H. R. Kim, J. W. Son, H. W. Lee, and J. H. Lee, “Three dimensional representations of partial ionic and electronic conductivity based on defect structure analysis of BaZr_{0.85}Y_{0.15}O_{3-δ},” *Solid State Ionics*, vol. 203, no. 1, pp. 9-17, Nov. 2011.
- [59] H. Zhu, S. Ricote, W. G. Coors, and R. J. Kee, “Interpreting equilibrium-conductivity and conductivity-relaxation measurements to establish thermodynamic and transport properties for multiple charged defect conducting ceramics,” *Faraday Discuss.*, vol. 182, pp. 49-74, 2015.
- [60] J. Maier, “Mass transport in the presence of internal defect reactions- Concept of Conservative Ensembles: IV, tracer diffusion and intercorrelation with chemical diffusion and ion conductivity,” *J. Am. Ceram. Soc.*, vol. 76, no. 5, pp. 1228-1232, May 1993.
- [61] L. Wang, “BSCF SOFC cathode materials: Bulk properties , kinetics and mechanism of oxygen reduction,” PhD thesis, University of Stuttgart, 2009.
- [62] C. S. Knee, A. Magrasó, T. Norby, and R. I. Smith, “Structural transitions and conductivity of BaPrO₃ and BaPr_{0.9}Y_{0.1}O_{3-δ},” *J. Mater. Chem.*, vol. 19, no. 20, p. 3238, 2009.
- [63] S. Escolástico, M. Ivanova, C. Solís, S. Roitsch, W. a. Meulenberg, and J. M. Serra, “Improvement of transport properties and hydrogen permeation of chemically-stable proton-conducting oxides based on the system BaZr_{1-x-y}Y_xM_yO_{3-δ},” *RSC Adv.*, vol. 2, no. 11, p. 4932, 2012.
- [64] D. Y. Kim, S. Miyoshi, T. Tsuchiya, and S. Yamaguchi, “Defect chemistry and electrochemical properties of BaZrO₃ heavily doped with Fe,” *ECS Trans.*, vol. 45, no. 1, pp. 161-170, Apr. 2012.
- [65] X. Ding, X. Gao, W. Zhu, J. Wang, and J. Jiang, “Electrode redox properties of Ba_{1-x}La_xFeO_{3-δ} as cobalt free cathode materials for intermediate-temperature SOFCs,” *Int. J. Hydrogen Energy*, vol. 39, no. 23, pp. 12092-12100, Aug. 2014.

- [66] J. Mizusaki, M. Okayasu, S. Yamauchi, and K. Fueki, "Nonstoichiometry and phase relationship of the SrFeO_{2.5}-SrFeO₃ system at high temperature," *J. Solid State Chem.*, vol. 99, no. 1, pp. 166-172, Jul. 1992.
- [67] J. Mizusaki, M. Yoshihiro, S. Yamauchi, and K. Fueki, "Nonstoichiometry and defect structure of the perovskite-type oxides La_{1-x}Sr_xFeO_{3-δ}," *J. Solid State Chem.*, vol. 58, no. 2, pp. 257-266, Jul. 1985.
- [68] R. Zohourian, R. Merkle, and J. Maier, "Proton uptake into the protonic cathode material BaCo_{0.4}Fe_{0.4}Zr_{0.2}O_{3-δ} and comparison to protonic electrolyte materials," *Solid State Ionics*, vol. 299, pp. 64-69, Jan. 2017.
- [69] D. N. Mueller, R. A. De Souza, J. Brendt, D. Samuelis, and M. Martin, "Oxidation states of the transition metal cations in the highly nonstoichiometric perovskite-type oxide Ba_{0.1}Sr_{0.9}Co_{0.8}Fe_{0.2}O_{3-δ}," *J. Mater. Chem.*, vol. 19, no. 14, p. 1960, 2009.
- [70] R. Zohourian, R. Merkle, G. Raimondi, and J. Maier, "Mixed-conducting perovskites as cathode materials for protonic ceramic fuel cells: understanding the trends in proton uptake," *Adv. Funct. Mater.*, vol. 28, 2018.
- [71] G. Raimondi, R. Merkle, and J. Maier, *unpublished*.
- [72] K. D. Kreuer, "Aspects of the formation and mobility of protonic charge carriers and the stability of perovskite-type oxides," vol. 125, pp. 285-302, 1999.
- [73] A. L. Allred and E. G. Rochow, "A scale of electronegativity based on electrostatic force," *J. Inorg. Nucl. Chem.*, vol. 5, no. 4, pp. 264-268, Jan. 1958.
- [74] R. D. Shannon, "Revised effective ionic radii and systematic studies of interatomic distances in halides and chalcogenides," *Acta Crystallogr. Sect. A*, vol. 32, no. 5, pp. 751-767, 1976.
- [75] K. D. Kreuer, S. Adams, W. Münch, A. Fuchs, U. Klock, and J. Maier, "Proton conducting alkaline earth zirconates and titanates for high drain electrochemical applications," *Solid State Ionics*, vol. 145, no. 1-4, pp. 295-306, Dec. 2001.
- [76] A. Løken, C. Kjølseth, and R. Haugrud, "Electrical conductivity and TG-DSC study of hydration of Sc-doped CaSnO₃ and CaZrO₃," *Solid State Ionics*, vol. 267, pp. 61-67, Dec. 2014.
- [77] T. S. Bjørheim, S. M. H. Rahman, S. G. Eriksson, C. S. Knee, and R. Haugrud, "Hydration thermodynamics of the proton conducting oxygen-deficient perovskite series BaTi_{1-x}M_xO_{3-x/2} with M = In or Sc," *Inorg. Chem.*, vol. 54, no. 6, pp. 2858-2865, Mar. 2015.
- [78] F. Krug, "The high-temperature proton conductor Ba₃(Ca_{1.18}Nb_{1.82})O_{9-δ}: Thermogravimetry of the water uptake," *Solid State Ionics*, vol. 92, no. 3-4, pp. 297-302, Nov. 1996.
- [79] Y. Okuyama, T. Kozai, S. Ikeda, M. Matsuka, T. Sakai, and H. Matsumoto, "Incorporation and conduction of proton in Sr-doped LaMO₃ (M=Al, Sc, In, Yb, Y)," *Electrochim. Acta*, vol. 125, pp. 443-449, Apr. 2014.

- [80] A. Magrasó, R. Haugrud, M. Segarra, and T. Norby, “Defects and transport in Gd-doped BaPrO₃,” *J. Electroceramics*, vol. 23, no. 1, pp. 80-88, Aug. 2009.
- [81] Y. Okuyama, T. Kozai, T. Sakai, M. Matsuka, and H. Matsumoto, “Proton transport properties of La_{0.9}M_{0.1}YbO_{3-δ} (M=Ba, Sr, Ca, Mg),” *Electrochim. Acta*, vol. 95, pp. 54-59, Apr. 2013.
- [82] Y. Larring and T. Norby, “Protons in LaErO₃,” *Solid State Ionics*, vol. 70-71, pp. 305-310, May 1994.
- [83] J. A. Duffy, “Ionic-covalent character of metal and nonmetal oxides,” *J. Phys. Chem. A*, vol. 110, no. 49, pp. 13245-13248, Dec. 2006.
- [84] L. Pauling, *The Nature of the Chemical Bond and the Structure of Molecules and Crystals: An Introduction to Modern Structural Chemistry*, Cornell University Press, 1960.
- [85] S. Svarcova, “Structural instability of cubic perovskite Ba_xSr_{1-x}Co_{1-y}Fe_yO_{3-δ},” *Solid State Ionics*, vol. 178, no. 35-36, pp. 1787-1791, Feb. 2008.
- [86] D. Gryaznov, R. Merkle, E. A. Kotomin, and J. Maier, “*Ab initio* modelling of oxygen vacancies and protonic defects in La_{1-x}Sr_xFeO_{3-δ} perovskite solid solutions,” *J. Mater. Chem. A*, vol. 4, no. 34, pp. 13093-13104, 2016.
- [87] M. H. R. Lankhorst, H. J. M. Bouwmeester, and H. Verweij, “High-temperature coulometric titration of La_{1-x}Sr_xCoO_{3-δ}: Evidence for the effect of electronic band structure on nonstoichiometry behavior,” *J. Solid State Chem.*, vol. 133, no. 2, pp. 555-567, 1997.
- [88] N. Grunbaum, L. Mogni, F. Prado, and A. Caneiro, “Phase equilibrium and electrical conductivity of SrCo_{0.8}Fe_{0.2}O_{3-δ},” *J. Solid State Chem.*, vol. 177, no. 7, pp. 2350-2357, Jul. 2004.
- [89] E. Bucher, W. Sitte, G. Caraman, V. Cherepanov, T. Aksenova, and M. Ananyev, “Defect equilibria and partial molar properties of (La,Sr)(Co,Fe)O_{3-δ},” *Solid State Ionics*, vol. 177, no. 35-36, pp. 3109-3115, Nov. 2006.
- [90] J. Mizusaki, Y. Mima, S. Yamauchi, K. Fueki, and H. Tagawa, “Nonstoichiometry of the perovskite-type oxides La_{1-x}Sr_xCoO_{3-δ},” *J. Solid State Chem.*, vol. 80, no. 1, pp. 102-111, May 1989.
- [91] J. I. Jung, S. T. Misture, and D. D. Edwards, “The electronic conductivity of Ba_{0.5}Sr_{0.5}Co_xFe_{1-x}O_{3-δ} (BSCF: $x = 0-1.0$) under different oxygen partial pressures,” *J. Electroceramics*, vol. 24, no. 4, pp. 261-269, Jun. 2010.
- [92] J. Wang, M. Saccoccio, D. Chen, Y. Gao, C. Chen, and F. Ciucci, “The effect of A-site and B-site substitution on BaFeO_{3-δ}: An investigation as a cathode material for intermediate-temperature solid oxide fuel cells,” *J. Power Sources*, vol. 297, pp. 511-518, Nov. 2015.
- [93] B. Wei, Z. Lü, X. Huang, M. Liu, N. Li, and W. Su, “Synthesis, electrical and electrochemical properties of Ba_{0.5}Sr_{0.5}Zn_{0.2}Fe_{0.8}O_{3-δ} perovskite oxide for IT-SOFC

- cathode,” *J. Power Sources*, vol. 176, no. 1, pp. 1–8, Jan. 2008.
- [94] R. Strandbakke, V. A. Cherepanov, A. Y. Zuev, D. S. Tsvetkov, C. Argirusis, G. Sourkouni, S. Prünke, and T. Norby, “Gd- and Pr-based double perovskite cobaltites as oxygen electrodes for proton ceramic fuel cells and electrolyser cells,” *Solid State Ionics*, vol. 278, pp. 120-132, Oct. 2015.
- [95] E. Vøllestad, M. Schrade, J. Segalini, R. Strandbakke, and T. Norby, “Relating defect chemistry and electronic transport in the double perovskite $\text{Ba}_{1-x}\text{Gd}_{0.8}\text{La}_{0.2+x}\text{Co}_2\text{O}_{6-\delta}$ (BGLC),” *J. Mater. Chem. A*, vol. 5, no. 30, pp. 15743-15751, 2017.
- [96] D. N. Mueller, R. A. De Souza, T. E. Weirich, D. Roehrens, J. Mayer, and M. Martin, “A kinetic study of the decomposition of the cubic perovskite-type oxide $\text{Ba}_x\text{Sr}_{1-x}\text{Co}_{0.8}\text{Fe}_{0.2}\text{O}_{3-\delta}$ (BSCF) ($x = 0.1$ and 0.5),” *Phys. Chem. Chem. Phys.*, vol. 12, no. 35, p. 10320, 2010.
- [97] J. Martynczuk, K. Efimov, L. Robben, and A. Feldhoff, “Performance of zinc-doped perovskite-type membranes at intermediate temperatures for long-term oxygen permeation and under a carbon dioxide atmosphere,” *J. Memb. Sci.*, vol. 344, no. 1-2, pp. 62-70, Nov. 2009.
- [98] L. Wang, R. Merkle, J. Maier, T. Acartürk, and U. Starke, “Oxygen tracer diffusion in dense $\text{Ba}_{0.5}\text{Sr}_{0.5}\text{Co}_{0.8}\text{Fe}_{0.2}\text{O}_{3-\delta}$ films,” *Appl. Phys. Lett.*, vol. 94, no. 7, p. 071908, Feb. 2009.
- [99] J. Fleig, “The grain boundary impedance of random microstructures: numerical simulations and implications for the analysis of experimental data,” *Solid State Ionics*, vol. 150, no. 1-2, pp. 181-193, Sep. 2002.
- [100] F. Baumann, J. Fleig, H. Habermeier, and J. Maier, “Impedance spectroscopic study on well-defined $(\text{La,Sr})(\text{Co,Fe})\text{O}_{3-\delta}$ model electrodes,” *Solid State Ionics*, vol. 177, no. 11-12, pp. 1071-1081, Apr. 2006.
- [101] J. Jamnik and J. Maier, “Generalised equivalent circuits for mass and charge transport: chemical capacitance and its implications,” *Phys. Chem. Chem. Phys.*, vol. 3, no. 9, pp. 1668-1678, 2001.
- [102] R. Merkle, J. Maier, and J. Fleig, “Mechanistic understanding and electrochemical modeling of mixed conducting (SOFC) electrodes,” in *Handbook of fuel cells-fundamentals, technology and applications.*, part 3, vol. 5, 2009.

Acknowledgement

I would like to express my sincere gratitude to all who have directly and indirectly helped me throughout this work.

At first, I deeply thank and am grateful to Prof. Dr. Joachim Maier for the opportunity he gave me to do my Ph.D. on this fascinating project and in an excellent research condition in his department in Max Planck Institute for Solid State Research.

I am grateful to Prof. Dr. Anke Weidenkaff and Prof. Dr. Joris van Slageren for reviewing my PhD thesis and being on my examination committee. Thanks to Prof. Dr. Hagen Klauk, my external advisor, for his helpful suggestions.

In particular, I would like to thank Dr. Rotraut Merkle, my day-to-day supervisor. I am sincerely grateful to her for the precise instructions in the lab, scientific discussions and proof-reading of the thesis and presentations. Her broad scientific knowledge helped the progress of this work a lot.

My special thanks to Sofia Weiglein and Dr. Hans George Libuda, coordinator of IMPRS, for their great administrative support from the very first days.

Dr. Helga Hoier has performed all the X-ray measurements in this project. I would like to sincerely thank her for her efforts. I am also very grateful to Annette Fuchs who has taken SEM images and trained me how to use Karl-Fischer titration. Thanks to all the technicians in the departments in particular Florian Kaiser, Udo Klock, and Armin Sorg who have been always available and helpful in the time of need, also Uwe Traub for helping with computer-related problems, always in the quickest way.

People in the Crystal preparation group, in particular, Barbara Baum, are thanked for assisting with the sample preparation. Thanks to Benjamin Stuhlhofer in the technology group for the preparation of microelectrode samples by PLD and photolithography and Samir Hammoud and Albert Meyer for ICP-OES measurements.

I would also like to thank Dr. Michael Weissmaier and Dr. Giuliano Gregori for training me in detail how to use spark plasma sintering. Thanks to the internship students Nico Röttcher, Julian Türck, and Julia Hübner for the preparation of some of the samples.

I enjoyed working in this department within a diverse and friendly environment and would like to thank everybody in particular following PhD and graduated students: Christian Berger, Dr. Chia-chin Chen, Dr. Elisa Gilardi, Maximilian Hödl, Yuanye Huang, Markus Joos, Dr. Pinar Kaya, Dr. Gee Yeong Kim, Dr. Gints Kucinskis, Lim Kyungmi, Simon Lorger, Dr. Jan Melchior, Dr. Ashkan Moradabadi, Andreas Münchinger, Maryam Nojabae, Giulia Raimondi, Torben Saatkamp, Maximilian Schaube, Alessandro Senocrate, and Dr. Sebastian Stämmler.

Lastly, I would like to thank my beloved parents, Ali and Masi, and my close friends for their loving support during this time.

Curriculum Vitae

Personal Information

Name: Reihaneh Zohourian Aboutorabi
Date of birth: 3. April 1990
Place of birth: Mashhad, Iran
E-Mail: r.zohouriann@gmail.com

Academic Education

Nov. 2014- July 2018: **Ph.D.**, Material Science
Max Planck Institute for Solid State Research, Stuttgart

Sept. 2008- Sept. 2014: **M.Sc. and B. Sc.**
Electrical Engineering and Electronics
Ferdowsi University of Mashhad

Sept. 2001- July 2008: **Highschool**, Mathematics and Physics
Farzanegan

Publications

- R. Merkle, R. Zohourian, and J. Maier, "Two-fold stoichiometry relaxation - Simulated relaxation kinetics of ionic and electronic defect concentrations," *Solid State Ionics*, vol. 288, pp. 291-297, May 2016.
- R. Zohourian, R. Merkle, and J. Maier, "Proton uptake into the protonic cathode material $\text{BaCo}_{0.4}\text{Fe}_{0.4}\text{Zr}_{0.2}\text{O}_{3-\delta}$ and comparison to protonic electrolyte materials," *Solid State Ionics*, vol. 299, pp. 64-69, Jan. 2017.
- R. Zohourian, R. Merkle, and J. Maier, "Bulk defect chemistry of PCFC cathode materials: Discussion of defect interactions," *ECS Trans.*, vol. 77, no. 10, pp. 133-138, May 2017.
- R. Zohourian, R. Merkle, G. Raimondi, and J. Maier, "Mixed-conducting perovskites as cathode materials for protonic ceramic fuel cells: Understanding the trends in proton uptake," *Advanced Functional Materials*, vol. 28, July 2018.
- R. Zohourian, R. Merkle, and J. Maier, "Defect interactions in mixed-conducting perovskites as protonic ceramic fuel cells cathode materials," *In preparation*.

Awards

Best poster award: Bunsentagung 2016: Basic mechanisms in energy conversion,
May 2016 Rostock, Germany

Best poster award: Summer school on "Ionic and protonic conducting ceramic
Sept. 2015 membranes for green energy applications", Valencia, Spain.